Effects of spatial heterogeneity on bacterial genetic circuits

Carlos Barajas[1] and Domitilla Del Vecchio[1*]

[1] Department of Mechanical Engineering, Massachusetts Institute of Technology, Cambridge, Massachusetts

[*] Correspondence: ddv@mit.edu

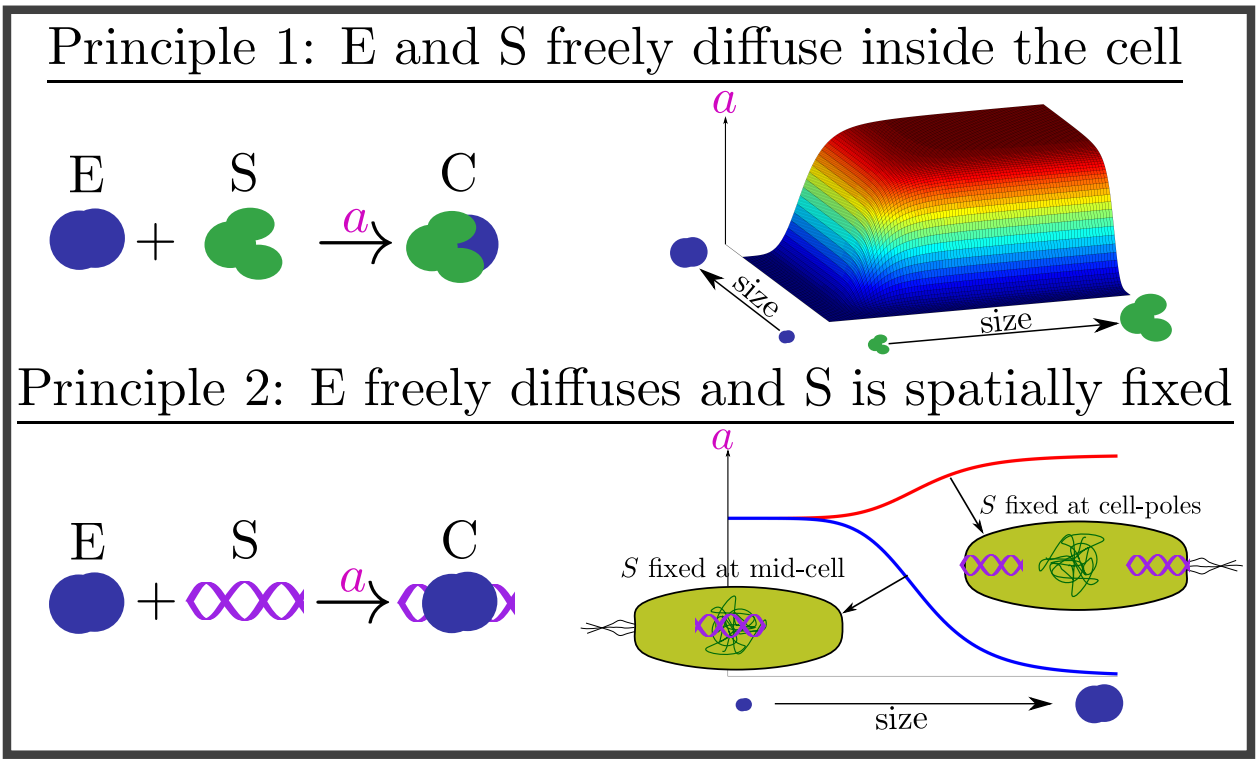

Highlights:

- Intracellular spatial heterogeneity modulates the effective association rate constant of binding reactions through a *binding correction factor* (BCF) that fully captures spatial effects
- The BCF depends on molecules size and location (if fixed) and can be determined experimentally
- Spatial heterogeneity may be detrimental or exploited for genetic circuit design
- Traditional well-mixed models can be appropriate despite spatial heterogeneity

Statement of significance: A general and simple modeling framework to determine how spatial heterogeneity modulates the dynamics of gene networks is currently lacking. To this end, this work provides a simple-to-use ordinary differential equation (ODE) model that can be used to both analyze and design genetic circuits while accounting for spatial intracellular effects. We apply our model to several core biological processes and determine that transcription and its regulation are more effective for genes located at the cell poles than for genes located on the chromosome and this difference increases with regulator size. For translation, we predict the effective binding between ribosomes and mRNA is higher than that predicted by a well-mixed model, and it increases with mRNA size. We provide examples where spatial effects are significant and should be considered but also where a traditional well-mixed model suffices despite severe spatial heterogeneity. Finally, we illustrate how the operation of well-known genetic circuits is impacted by spatial effects.

Abstract

Intracellular spatial heterogeneity is frequently observed in bacteria, where the chromosome occupies part of the cell's volume and a circuit's DNA often localizes within the cell. How this heterogeneity affects core processes and genetic circuits is still poorly understood. In fact, commonly used ordinary differential equation (ODE) models of genetic circuits assume a well-mixed ensemble of molecules and, as such, do not capture spatial aspects. Reaction-diffusion partial differential equation (PDE) models have been only occasionally used since they are difficult to integrate and do not provide mechanistic understanding of the effects of spatial heterogeneity. In this paper, we derive a reduced ODE model that captures spatial effects, yet has the same dimension as commonly used well-mixed models. In particular, the only difference with respect to a well-mixed ODE model is that the association rate constant of binding reactions is multiplied by a coefficient, which we refer to as the binding correction factor (BCF). The BCF depends on the size of interacting molecules and on their location when fixed in space and it is equal to unity in a well-mixed ODE model. The BCF can be used to investigate how spatial heterogeneity affects the behavior of core processes and genetic circuits. Specifically, our reduced model indicates that transcription and its regulation are more effective for genes located at the cell poles than for genes located on the chromosome. The extent of these effects depends on the value of the BCF, which we found to be close to unity. For translation, the value of the BCF is always greater than unity, it increases with mRNA size, and, with biologically relevant parameters, is substantially larger than unity. Our model has broad validity, has the same dimension as a well-mixed model, yet it incorporates spatial heterogeneity. This simple-to-use model can be used to both analyze and design genetic circuits while accounting for spatial intracellular effects.

1 Introduction

Deterministic models of gene circuits typically assume a well-mixed ensemble of species inside the cell [1, 2]. This assumption allows one to describe genetic circuit dynamics through a set of ODEs, for which a number of established analysis tools are available [1]. However, it is well known that spatial heterogeneity is prevalent inside bacterial cells [3, 4, 5, 6, 7, 8]. Depending on the origin of replication, plasmids tend to localize within bacterial cells [9, 10, 11]. Furthermore, chromosome genes (endogenous and synthetically integrated ones [12]) are distributed in the cell according to the chromosome complex spatial structure. In bacterial cells, any molecule freely diffusing through the chromosome (e.g., mRNA, ribosome, and protease) experiences what are known as *excluded volume effects*, which capture the tendency of species to be ejected from the nucleoid due to the space occupied by the dense DNA mesh [13]. These excluded volume effects for ribosomes and RNAP in bacteria have been observed experimentally [14].

Despite the strong evidence in support of spatial heterogeneity within bacterial cells, a convenient modeling framework that captures the spatio-temporal organization of molecules inside the cell is largely lacking. As a consequence, how spatial effects modulate genetic circuit dynamics remains also poorly understood. Partial differential equation (PDE) models have been employed on an *ad hoc* basis to numerically capture intracellular spatial dynamics for specific case studies [15, 16, 17]. Although a general PDE model of a gene regulatory network (GRN) can be constructed, it is difficult to analyze and impractical for design [18]. Recently, the method of matched asymptotic expansions was used to simplify the PDEs to a set of ODEs to analyze ribosome-mRNA interactions [19]. Similarly, [20] used a compartmentalized model to capture spatial heterogeneity in sRNA-mRNA interactions. However, these results have not been generalized, relied on simulation, and specific parameter values.

In this paper, we provide a general framework to model spatial heterogeneity through an ODE that has the same structure and hence dimensionality as a well-mixed ODE model. To this end, we first introduce a PDE model that captures spatial dynamics. Next, we exploit the time scale separation between molecule diffusion and biochemical reactions to derive a reduced order ODE model of the space averaged dynamics. This model accounts for spatial heterogeneity by multiplying the association rate constant of binding reactions by a factor that depends on the size of freely diffusing species and on the location of spatially fixed species. We call this factor the *binding correction factor* (BCF). Thus, this reduced model has the same dimensionality as traditional well-mixed models, yet it captures spatial effects.

We demonstrate the effects of spatial heterogeneity in genetic circuit behavior by modeling and analyzing several core biological processes. We show that the transcription rate of a gene and the affinity at which transcription factors bind to it, is lower (higher) when the gene is located near mid-cell (cell poles) with respect to the well-mixed model. We show that compared to a well-mixed model, translation rate is always higher and increases with mRNA size. Finally, we consider a genetic clock, a circuit that produces sustained

oscillations. We show that for a parameter range where a well-mixed model predicts sustained oscillations, a model that accounts for spatial heterogeneity of DNA may not show oscillations. All of these phenomena can be recapitulated by our reduced ODE model.

Methods

We use mathematical models to investigate the effects of spatial heterogeneity, specifically DNA localization and excluded volume effects, on genetic circuit behavior. The first part of this section introduces the mathematical model used, a set of nonlinear PDEs. Model reduction is performed on the resulting PDEs to obtain the reduced ODE model that we use to predict how molecule size and location affect genetic circuit's behavior.

1.1 Reaction-Diffusion Model

A reaction-diffusion model describes the concentration of a species at a given time and location in the cell. We focus on enzymatic-like reactions since they can be used to capture most core processes in the cell. We specialize the model to the cases where the reacting species both freely diffuse or where one freely diffuses while the other one is fixed. For example, mRNA and ribosomes are both freely diffusing, while for RNA polymerase and DNA, one is freely diffusing and the other one is fixed.

1.1.1 Enzymatic-like reactions that model core biological processes

Let S be a substrate being shared by n enzymes $\mathrm{E_i}$, to form product $\mathrm{P_i}$ where $i = 1, \ldots, n$. The rate at which $\mathrm{E_i}$ and S are produced is given by α_i and α_s, respectively. The decay rates of $\mathrm{E_i}$ and S are given by γ_i and γ_s, respectively. Here, we assume that $\mathrm{E_i}$ and S can be degraded even in complex form, that is, the complex is not protecting them from degradation. Finally, all species are diluted as the cell divides at a rate μ. The biochemical reactions corresponding to this process are given by:

$$\emptyset \xrightarrow{\alpha_\mathrm{i}} \mathrm{E_i} \xrightarrow{\gamma_\mathrm{i}+\mu} \emptyset, \quad \emptyset \xrightarrow{\alpha_\mathrm{s}} \mathrm{S} \xrightarrow{\gamma_\mathrm{s}+\mu} \emptyset, \quad \mathrm{c_i} \xrightarrow{\gamma_\mathrm{i}} \mathrm{S}, \quad \mathrm{c_i} \xrightarrow{\gamma_\mathrm{s}} \mathrm{E_i}, \quad \mathrm{c_i} \xrightarrow{\mu} \emptyset, \quad \mathrm{E_i} + \mathrm{S} \underset{\mathrm{d_i}}{\overset{\mathrm{a_i}}{\rightleftharpoons}} \mathrm{c_i} \xrightarrow{\kappa_\mathrm{i}} \mathrm{P_i} + \mathrm{E_i} + \mathrm{S}, \tag{1}$$

where $\mathrm{c_i}$ is the complex formed when $\mathrm{E_i}$ binds to S, a_i is the association rate constant, d_i is the dissociation rate constant, and κ_i is the catalytic rate constant of product formation. These enzymatic-like reactions capture many core biological processes such as genes transcribed by RNA polymerase, mRNA translated by ribosomes, or proteins degraded by a common protease [1]. Notice that they differ from the classical enzymatic reactions since the substrate is not converted into product [1].

E. coli actively regulates its geometry to achieve a near-perfect cylindrical shape [21]. Thus, we model the cell as a cylinder of length $2L$ and radius R_c. This geometry is shown in Figure 1-A. We assume angular and radial homogeneity ($(R_c/L)^2 \ll 1$) such that the concentration of a species varies only axially (the spatial x direction). Symmetry relative to mid-cell is assumed and hence only half of the cell is considered, that is, $x \in [0, L]$, where $x = 0$ is at mid-cell and $x = L$ is at the cell poles. Furthermore, we assume a constant cross-sectional area along the axial direction.

In [14] it was shown that polysomes were excluded from the dense chromosomal DNA mesh onto the cell poles. These phenomena is generalized for any species that freely diffuses within the DNA mesh and is referred to as "excluded volume effects". Leveraging the diffusion modeling framework from [13], we now specify the model to capture excluded volume effects. Let $v(x) \in (0, 1]$ be the volume fraction (dimensionless) available to a species to diffuse within the chromosome (Figure 1-B). As derived in [13] and discussed in SI Section 2.5, the available volume profile $v(x)$ of a species with a radius of gyration r, takes the form

$$v(x) = e^{-(r/r^*)^2 \hat{\rho}(x)}, \quad (r^*)^2 = \frac{V_p}{2\kappa\pi L_p}, \tag{2}$$

where $\hat{\rho}(x)$ is the normalized local density of chromosome DNA length such that $\frac{2}{L}\int_0^L \hat{\rho}(x)dx = 1$, L_p is the total length of chromosome DNA, V_p the volume where the DNA polymer is confined, such that L_p/V_p is the total DNA length per volume , and κ is an empirically determined correction factor (see [13] and SI Section 2.5). The quantity $(r^*)^2$ is inversely proportional to the total DNA length per volume. The local DNA density $\hat{\rho}(x)$ is assumed to be monotonically decreasing (i.e, the chromosome is more dense near

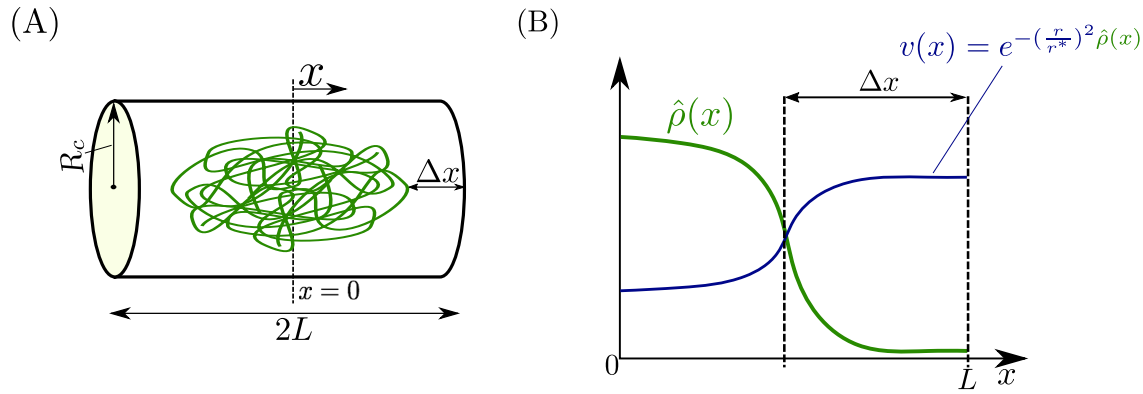

Figure 1: **Intracellular spatial geometry.** (A) We model the cell as a cylinder of radius R_c and length $2L$. The distance between the end of the chromosome and the cell poles is Δx. (B) The spatial profiles for the normalized local density of DNA length $\hat{\rho}(x)$ and the fraction of available volume $v(x)$ of a freely diffusing species with radius of gyration r within the chromosomal mesh. These two quantities are related by $v(x) = e^{-(r/r^*)^2 \hat{\rho}(x)}$, where r^* is a length scale dependent on the averaged chromosome density in the cell given by (2). The chromosome density is assumed to be monotonically decreasing from mid-cell to the cell poles (as in [13]), thus the available volume profile are monotonically increasing.

mid-cell than at the cell poles as shown in Figure 1-B). Therefore by (2), the available volume profile is higher near mid-cell than at the cell poles (i.e., $v(0) < v(L)$) as shown in Figure 1-B and furthermore, the discrepancy between $v(0)$ and $v(L)$ increases with r/r^*. For all simulations in this study, we model the normalized chromosome density as

$$\hat{\rho}(x) = \frac{1}{1 + e^{20(x/L - 1/2)}},$$

as experimentally determined in [13]. We note that the specific expressions of $\hat{\rho}(x)$ and r/r^* do not affect the model reduction result of this paper. The main results in this paper are presented for a constant cell length L and chromosome DNA density $\hat{\rho}(x)$, however in SI Section 2.13 we relax these assumptions and allow these quantities to vary in time as the cell divides.

For any given species with concentration per unit length given by $y(t,x)$, free to diffuse, with available volume $v(x)$, an expression for the flux term, derived in [13] is given by:

$$J(x,y) = D\Bigg(\underbrace{-\frac{\partial y(t,x)}{\partial x} v(x)}_{\text{towards low concentration}} + \underbrace{y(t,x)\frac{\partial v(x)}{\partial x}}_{\text{towards high available volume}} \Bigg) = -v(x)^2 \frac{d}{dx}\left[\frac{y(t,x)}{v(x)}\right], \tag{3}$$

where D is the diffusion coefficient. The flux is driven by two mechanisms: the first is concentration gradient, which pushes molecules from high to low concentrations and the second drives molecules to regions with a higher volume fraction. This second term is referred to as the excluded volume effect [13]. From (3), if $\left|\frac{\partial y(t,x)}{\partial x} v(x)\right| < \left|y(t,x)\frac{\partial v(x)}{\partial x}\right|$ and $\frac{\partial y(t,x)}{\partial x}\frac{\partial v(x)}{\partial x} > 0$, then the net flux is from low to high concentration, which is the case when species are repelled from the chromosome to high concentration areas in the cell poles. As we will show, this mechanism dictates intracellular heterogeneity in the limit of fast diffusion.

For species S, we denote by $S(t,x)$ its concentration per unit length at time t at location x (similarly for $\mathrm{E_i}$ and $\mathrm{c_i}$). Assuming sufficently high molecular counts, the reaction-diffusion dynamics corresponding to (1) describing the rate of change of the species concentrations at position x, are given by [22] :

$$\begin{aligned}
\frac{\partial E_i(t,x)}{\partial t} &= -\frac{d}{dx}\big[J(x,E_i)\big] + \alpha_i(t,x) - a_i E_i(t,x)S(t,x) + (\gamma_s + d_i + \kappa_i)c_i(t,x) - (\gamma_i + \mu)E_i(t,x),\\
\frac{\partial c_i(t,x)}{\partial t} &= -\frac{d}{dx}\big[J(x,c_i)\big] + a_i E_i(t,x)S(t,x) - (\gamma_i + \gamma_s + d_i + \kappa_i + \mu)c_i(t,x),\\
\frac{\partial S(t,x)}{\partial t} &= -\frac{d}{dx}\big[J(x,S)\big] + \alpha_s(t,x) + \sum_{j=1}^{n}\big[-a_j E_j(t,x)S(t,x) + (\gamma_j + d_j + \kappa_j)c_j(t,x)\big] - (\gamma_s + \mu)S(t,x),
\end{aligned} \tag{4}$$

where $J(x,\cdot)$ is the flux per unit area per unit time, within the cell. If the species is freely diffusing $J(x,\cdot)$ is given by (3), otherwise if the species is spatially fixed, then $J(x,\cdot)=0$ for all $x\in[0,L]$. The boundary conditions associated with freely diffusing species of (4) are zero flux at the cell poles and cell center due to the assumed left-right symmetry, which corresponds to:

$$J(0,\cdot)=J(L,\cdot)=0. \tag{5}$$

Notice that none of the parameters in (4) appearing in (1) depend explicitly on time and space except for the production terms $\alpha_i(t,x)$ and $\alpha_s(t,x)$. The explicit time dependence of the production terms allows us to capture how genes can be activated or repressed externally with a time varying signal [23]. The explicit dependence of the production terms on x allows us to capture where the species is produced within the cell (e.g., DNA in the chromosome or DNA in pole localized plasmid genes).

Dimensionless model: Depending on the parameter regimes, the dynamics of (4) can display time scale separation. For example, diffusion occurs in the order of mili-seconds compared to minutes for dilution due to cell-growth and mRNA degradation [2]. Therefore, we are interested in determining the behavior of (4) in the limit of fast diffusion. We thus rewrite (4) in dimensionless form to make time scale separation explicit. We nondimensionalize the system variables using dilution ($1/\mu$) as the characteristic time scale, the length of the cell (L) as the characteristic length, and μ/a_1 as the characteristic concentration per length scale: $t^*=t\mu,\ y^*=y\frac{a_1}{\mu},\ x^*=\frac{x}{L}$, where y denotes concentration per unit length and the superscript "$*$" is used on the dimensionless variable. Concentrations are nondimensionalized through a_1 because this parameter contains a concentration scale, it is fixed in time, and it is assumed to be nonzero. The dimensionless form of (4) is given by

$$\begin{aligned}
\frac{\partial E_i^*(t^*,x^*)}{\partial t^*} &= -\frac{d}{dx^*}\big[J^*(x^*,E_i^*)\big]+\alpha_i^*(t^*,x^*)+\frac{1}{\eta_i}\Big[-E_i^*(t^*,x^*)S^*(t^*,x^*)\frac{a_i^*}{\tilde{d}_i}+c_i^*(t^*,x^*)\Big]\\
&\qquad -(\gamma_i^*+1)(E_i^*(t^*,x^*)+c_i^*(t^*,x^*)),\\
\frac{\partial c_i^*(t^*,x^*)}{\partial t^*} &= -\frac{d}{dx^*}\big[J^*(x^*,c_i^*)\big]+\frac{1}{\eta_i}\Big[E_i^*(t^*,x^*)S^*(t^*,x^*)\frac{a_i^*}{\tilde{d}_i}-c_i^*(t^*,x^*)\Big],\\
\frac{\partial S^*(t^*,x^*)}{\partial t^*} &= -\frac{d}{dx^*}\big[J^*(x^*,S^*)\big]+\alpha_s^*(t^*,x^*)+\sum_{j=1}^{n}\frac{1}{\eta_j}\Big[-E_j^*(t^*,x^*)S^*(t^*,x^*)\frac{a_j^*}{\tilde{d}_j}+c_j^*(t^*,x^*)\Big]\\
&\qquad -(\gamma_s^*+1)(S^*(t^*,x^*)+\sum_{j=1}^{n}c_j^*(t^*,x^*)),
\end{aligned} \tag{6}$$

where $a_i^*=a_i/a_1$, $\gamma_s^*=\gamma_s/\mu$, $\gamma_i^*=\gamma_i/\mu$, $d_i^*=d_i/\mu$, $\kappa_i^*=\kappa_i/\mu$, $\alpha_i^*=\alpha_i a_1/\mu^2$, $\alpha_s^*=\alpha_s a_1/\mu^2$, $\tilde{d}_i=\gamma_i^*+\gamma_s^*+d_i^*+\kappa_i^*+1$, $\eta_i=1/\tilde{d}_i$, and $J^*=Ja_1/(\mu^2L)$. For a freely diffusing species with diffusion coefficient D, the dimensionless parameter that determines the relative speed of diffusion is denoted by $\epsilon=\mu L^2/D$ and fast diffusion corresponds to $\epsilon\ll 1$. Likewise, η_i in (4) determines the relative speed of the binding dynamics, where $\eta_i\ll 1$ implies these reactions are fast. From hereon, unless otherwise specified, we work with variables in their dimensionless form and drop the star superscript for simplifying notation.

Space averaged concentrations: Concentrations per cell are usually the quantities measured experimentally [24] and are the primary quantities of interest. We now derive the space averaged dynamics corresponding to (6), which describe the dynamics of concentrations per half of the cell. We define $\bar{E}_i(t)$, $\bar{S}(t)$, and $\bar{c}_i(t)$ to be the *space averaged enzyme, substrate, and complex concentrations*, respectively, and are given by

$$\bar{E}_i(t)=\int_0^1 E_i(t,x)dx,\quad \bar{c}_i(t)=\int_0^1 c_i(t,x)dx,\quad \bar{S}(t)=\int_0^1 S(t,x)dx,$$

also giving the concentrations per half of the cell. The dynamics governing these space averaged variables are derived by integrating (6) in space and applying the boundary conditions (5) and are given by:

$$\begin{aligned}
\frac{d\bar{E}_i(t)}{dt} &= \bar{\alpha}_i(t)-\frac{1}{\eta_i}\big[\bar{E}_i(t)\bar{S}(t)\frac{a_i\theta_i(t)}{\tilde{d}_i}-\bar{c}_i(t)\big]-(\gamma_i+1)(\bar{E}_i(t)+\bar{c}_i(t)),\\
\frac{d\bar{c}_i(t)}{dt} &= \frac{1}{\eta_i}\big[\bar{E}_i(t)\bar{S}(t)\frac{a_i\theta_i(t)}{\tilde{d}_i}-\bar{c}_i(t)\big],\\
\frac{d\bar{S}(t)}{dt} &= \bar{\alpha}_s(t)-\sum_{j=1}^{n}\frac{1}{\eta_j}\Big[\bar{E}_j(t)\bar{S}(t)\frac{a_j\theta_j(t)}{\tilde{d}_j}-\bar{c}_j(t)\Big]-(\gamma_s+1)(\bar{S}(t)+\sum_{j=1}^{n}\bar{c}_j(t)),
\end{aligned} \tag{7a}$$

where overbars denote spatially averaged variables and

$$\theta_i(t) = \frac{\int_0^1 E_i(t,x)S(t,x)dx}{\left[\int_0^1 E_i(t,x)dx\right]\left[\int_0^1 S(t,x)dx\right]}. \tag{7b}$$

Therefore, to calculate the space averaged concentrations, one could integrate the outputs of the full PDE (6) directly or use (7) along with (7b), as illustrated in Figure 2. Notice that calculating θ_i in (7b) requires solving the full PDE system (6) because of its dependence on the product $E_i(t,x)S(t,x)$. Therefore, in general, there is no obvious benefit in working with (7). In this paper, we provide a method to compute a guaranteed approximation of θ_i without solving the PDEs (6).

Well-mixed model: Next, we define what we have been informally referring to as the "well-mixed" model [25]. A standard well-mixed model is derived starting from (1) assuming mass action kinetics, that molecular counts are sufficiently large, and that the intracellular environment is spatially homogeneous (well-mixed) [1]. We let $\bar{E}_i^{\mathrm{wm}}(t)$, $\bar{S}^{\mathrm{wm}}(t)$ and $\bar{c}_i^{\mathrm{wm}}(t)$, denote the well-mixed concentrations of $\mathrm{E_i}$, S, and $\mathrm{c_i}$, respectively, and their dynamics are given by

$$\begin{aligned}
\frac{d\bar{E}_i^{\mathrm{wm}}(t)}{dt} &= \bar{\alpha}_i(t) - \frac{1}{\eta_i}\left[\bar{E}_i^{\mathrm{wm}}(t)\bar{S}^{\mathrm{wm}}(t)\frac{a_i}{\tilde{d}_i} - \bar{c}_i^{\mathrm{wm}}(t)\right] - (\gamma_i+1)(\bar{E}_i^{\mathrm{wm}}(t) + \bar{c}_i^{\mathrm{wm}}(t)),\\
\frac{d\bar{c}_i^{\mathrm{wm}}(t)}{dt} &= \frac{1}{\eta_i}\left[\bar{E}_i^{\mathrm{wm}}(t)\bar{S}^{\mathrm{wm}}(t)\frac{a_i}{\tilde{d}_i} - \bar{c}_i^{\mathrm{wm}}(t)\right],\\
\frac{d\bar{S}^{\mathrm{wm}}(t)}{dt} &= \bar{\alpha}_s(t) - \sum_{j=1}^{n}\frac{1}{\eta_j}\left[\bar{E}_j^{\mathrm{wm}}(t)\bar{S}^{\mathrm{wm}}(t)\frac{a_j}{\tilde{d}_j} - \bar{c}_j^{\mathrm{wm}}(t)\right] - (\gamma_s+1)(\bar{S}^{\mathrm{wm}}(t) + \sum_{j=1}^{n}\bar{c}_j^{\mathrm{wm}}(t)).
\end{aligned} \tag{8}$$

Comparing (7) and (8), motivates us to define $a_i'(t) = a_i\theta_i(t)$, which can be regarded as the effective association rate constant between $\mathrm{E_i}$ and S in (7). We refer to $\theta_i(t)$ as the *binding correction factor* (BCF). The dynamics of the space averaged concentrations (7) coincide with those of the well-mixed model (8) when $\theta_i(t) = 1$ (thus $a_i'(t) = a_i$) for all time and for all $i = 1,\ldots,n$. From (7b) notice that $E_i(t,x)$ and $S(t,x)$ being spatially constant for all time is not necessary for $\theta_i(t) = 1$ for all time. For example, if $S(t,x)$ is spatially constant while $E_i(t,x)$ has an arbitrary spatial profile (or *vice-versa*), then $\theta_i(t) = 1$. Thus, the space averaged concentrations can coincide with those of a well-mixed model despite severe spatial heterogeneity. In this work, we provide a constant approximation of $\theta_i(t)$ denoted by θ_i^*, which depends on spatial variables such as molecule size and gene location. Under the fast diffusion approximation, we show that θ_i^* is close to $\theta_i(t)$. The space averaged dynamics (7) with $\theta_i(t)$ replaced by θ_i^*, thus provides a reduced ODE model that captures spatial information without having to solve (6). We will compare how solutions to (7) with (7b) calculated from the full PDE (6) or with θ_i^* compare to each other and to the solutions of the well-mixed model (8).

1.1.2 Three diffusion cases to capture core biological processes

To use model (6) to describe key biological processes, we consider three cases. In Case I, $\mathrm{E_i}$ for all $i = 1,\ldots,n$ and S are all freely diffusing within the cell. In Case II, $\mathrm{E_i}$ is spatially fixed for all $i = 1,\ldots,n$ ($J(x,E_i) = 0$ for all $x \in [0,1]$ and for all $i = 1,\ldots,n$) and S is freely diffusing. In Case III, $\mathrm{E_i}$ is freely diffusing for all $i = 1,\ldots,n$ and S is spatially fixed ($J(x,S) = 0$ for all $x \in [0,1]$). Case I may represent mRNA molecules ($\mathrm{E_i}$) competing for ribosomes (S), all freely diffusing in the cell. Case II captures genes ($\mathrm{E_i}$), which are spatially fixed and are transcribed by RNA polymerase (S), which freely diffuses. Case III models transcription factors ($\mathrm{E_i}$), which freely diffuse regulating the same spatially fixed gene (S).

The flux dynamics, the boundary conditions, and a core biological process example for each case are summarized in Table. 1. When a species is spatially fixed, the flux is zero through the whole domain, that is, $J(x,\cdot) = 0$ for all $x \in [0,1]$. The available volume profiles for the enzyme, complex, and substrate are denoted by $v_{E_i}(x)$, $v_{c_i}(x)$, and $v_S(x)$, respectively. The available volume profile for the complex $v_{c_i}(x)$, represents the probability that the complex has enough free volume to hop into the DNA mesh at position x and it equals the product of the probability of the two independent events of the enzyme and the substrate hopping into the DNA mesh [13], thus

$$v_{c_i}(x) = v_{E_i}(x)v_S(x). \tag{9}$$

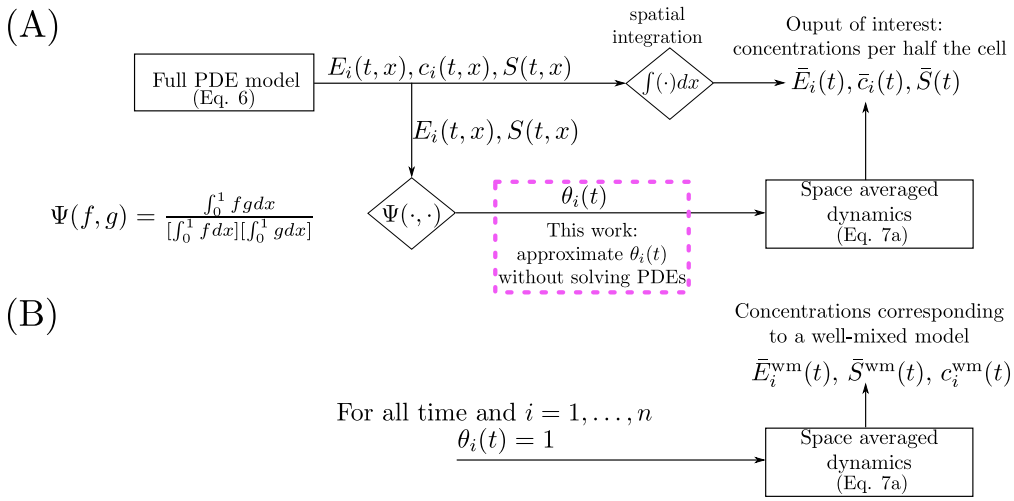

Figure 2: **Methods to calculate space averaged concentrations.** (A) The time and space dependent solutions of the full PDE (6) are integrated spatially to yield concentrations per half of the cell. Alternatively, space averaged concentrations can be calculated using the space average dynamics (7) with the BCF ($\theta_i(t)$ (7b)) as a time varying parameter. (B) The dynamics of the space averaged concentration is given by the well mixed model (8) when $\theta_i(t) = 1$ for all time and for all $i = 1, \ldots, n$.

Furthermore, we define the normalized available volume profiles as

$$\hat{v}_{E_i}(x) = \frac{v_{E_i}(x)}{\int_0^1 v_{E_i}(x)dx}, \quad \hat{v}_{c_i}(x) = \frac{v_{c_i}(x)}{\int_0^1 v_{c_i}(x)dx}, \quad \hat{v}_S(x) = \frac{v_S(x)}{\int_0^1 v_S(x)dx}. \tag{10}$$

	Case I All species diffuse	**Case II** Substrate diffuse and enzymes fixed	**Case III** Enzymes diffuse and substrate fixed
Dimensionless Flux	$J(x,E_i) = -\frac{1}{\epsilon}\chi_{E_i} v_{E_i}^2 \frac{d}{dx}[\frac{E_i}{v_{E_i}}]$ $J(x,S) = -\frac{1}{\epsilon} v_S^2 \frac{d}{dx}[\frac{S}{v_s}]$ $J(x,c_i) = -\frac{1}{\epsilon}\chi_{c_i} v_{c_i}^2 \frac{d}{dx}[\frac{c_i}{v_{c_i}}]$	$J(x,E_i) = 0$ $J(x,S) = -\frac{1}{\epsilon} v_s^2 \frac{d}{dx}[\frac{S}{v_s}]$ $J(x,c_i) = 0$	$J(x,E_i) = -\frac{1}{\epsilon} v_{E_i}^2 \frac{d}{dx}[\frac{E_i}{v_{E_i}}]$ $J(x,S) = 0$ $J(x,c_i) = 0$
Boundary conditions	$J(0,E_i) = J(1,E_i) = 0$ $J(0,c_i) = J(1,c_i) = 0$ $J(0,S) = J(1,S) = 0$	$J(0,S) = J(1,S) = 0$	$J(0,E_i) = J(1,E_i) = 0$
ϵ	$(\mu L^2)/D_s$	$(\mu L^2)/D_s$	$(\mu L^2)/D_{E_1}$
Dimensionless diffusion	$\chi_{E_i} = D_{E_i}/D_s, \chi_{c_i} = D_{c_i}/D_s$	N/A	N/A
Core process	mRNAs binding ribosomes	RNAP binding several genes	Transcription factors binding promoter
Location of fixed species	N/A	x_i^*	x_s^*

Table 1: The flux dynamics and the boundary conditions corresponding to (6) for each case of interest along with a core process example. Here $v_{E,i}(x)$, $v_S(x)$, and $v_{c,i}(x)$, are the available volume profiles of $\mathrm{E_i}$, S, and $\mathrm{c_i}$, respectively. The parameters D_{E_i}, D_{c_i}, and D_s, are the enzyme, complex, and substrate diffusion coefficients, respectively, ϵ is a dimensionless parameter that captures the speed of diffusion (with respect to dilution). A species being spatially fixed translates to the flux being zero throughout the whole spatial domain. In Case II, for $i = 1, \ldots, n$, $x_i^* \in (0,1)$ denotes the location of the fixed species $\mathrm{E_i}$. In Case III, $x_s^* \in (0,1)$ denotes the location of the fixed species S.

1.2 Numerical Method: Finite Difference

In general, a closed form solution to (6) is not available. Therefore, we rely on numerical solutions to directly integrate the PDE. In particular, we utilize a finite difference method that is widely used to simulate PDEs [26]. For a general diffusing species with its concentration given by $y(t,x)$, and available volume profile $v(x)$, we make the following coordinate transformation $u(t,x) := y(t,x)/v(x)$. In this coordinate, the boundary conditions (if applicable) are Neumann [27]: $\frac{\partial u}{\partial x}\big|_{x=0,1} = 0$ and thus are simpler to implement. Furthermore, with this transformation we observe less stiffness in the numerical simulations. We discretized the spatial domain into $N+1$ equidistant points such that $\Delta = 1/N$. Using a second order finite difference method, we approximate the derivatives as:

$$\frac{\partial u}{\partial x}\bigg|_{x=x_i^*} \approx \frac{u(t,x_{i+1}) - u(t,x_{i-1})}{2\Delta} \text{ and } \frac{\partial^2 u}{\partial x^2}\bigg|_{x=x_i^*} \approx \frac{u(t,x_{i+1}) - 2u(t,x_i^*) + u(t,x_{i-1})}{\Delta^2},$$

that appear in the flux terms (in the case where species freely diffuses). The new boundary conditions give rise to the following constraints:

$$\frac{\partial^2 u}{\partial x^2}\bigg|_{x=0} \approx 2\frac{u(t,x_2) - u(t,0)}{\Delta^2} \text{ and } \frac{\partial^2 u}{\partial x^2}\bigg|_{x=1} \approx 2\frac{u(t,x_N) - u(t,1)}{\Delta^2}.$$

This discretization leads to a system of $N+1$ ODEs. The resulting set of ODEs are then simulated with MATLAB, using the numerical ODE solvers ode23s. To calculate the space averaged concentrations, we implement a second oder trapezoidal integration scheme [27] given by:

$$\bar{y}(t) := \int_0^1 y(t,x)dx, \quad \bar{y}(t) \approx \frac{\Delta}{2}\sum_{j=1}^{N}\big[y(t,x_j) + y(t,x_{j+1})\big].$$

The convergence rate of our numerical method is demonstrated in Section 2.10. For all simulations in this paper $N = 200$.

Results

1.3 Time Scale Separation

In this section, we provide a time independent approximation of the BCF (7b) in the limit of fast diffusion, which depends solely on the size of diffusing species, chromosome density profiles, and the spatial localization of non-diffusing species. With this approximation, we can compute space averaged solutions in (7) without solving the PDEs in (6).

1.3.1 Reduced space averaged dynamics when diffusion is fast and fixed species are localized

For Case II and Case III of Table 1, in which one of the reacting species is fixed, we assume that the *fixed species is spatially localized* to a small space, that is, we have the situation depicted in Figure 3 (see SI Section 2.3, Assumption 3 for the mathematical definition). Practically, for Case II, spatial localization at x_i^* requires that the production rate $\alpha_i(t,x)$ of the fixed species is smaller than some small threshold δ when x is outside the interval $[x_i^* - \delta, x_i^* + \delta]$ for all time and that the space averaged production rate is $\bar{\alpha}_i(t)$ independent of δ (similarly for Case III, x_s^*, and $\alpha_s(t,x)$). From a biological perspective, having the space averaged production rate independent of δ is consistent with the fact that the total amount of DNA in the cell is independent of where the DNA is concentrated. Note that δ is a parameter that controls the amount of localization, such that $\delta \ll 1$ implies the production of spatially fixed species being localized to a small region. Let ϵ be as in Table 1 that appears in (6), the following definition will provide the candidate reduced model that approximates (7) well when $\epsilon \ll 1$ and $\delta \ll 1$. Recall that ϵ is a dimensionless parameter that captures the speed of diffusion (with respect to dilution).

Let x_i^* and x_s^* be the location of the fixed species for Case II and Case III, respectively (see Table 1). For

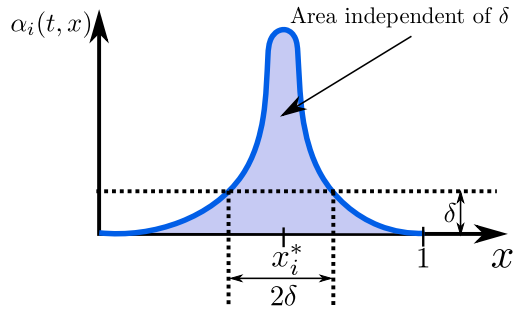

Figure 3: **Graphical representation of localization of fixed species** The production rate $\alpha_i(t,x)$ is assumed to be localized at x_i^* if $\alpha_i(t,x) \leq \delta, \forall x \notin [x_i^* - \delta, x_i^* + \delta]$. We assume that the space averaged production $\bar{\alpha}_i(t) = \int_0^1 \alpha_i(t,x)dx$ is independent of δ.

$i = 1, \ldots, n$, we define the *reduced space-averaged dynamics* as

$$\begin{aligned}
\frac{d\hat{\bar{E}}_i(t)}{dt} &= \bar{\alpha}_i(t) - \frac{1}{\eta_i}\left[\hat{\bar{E}}_i(t)\hat{\bar{S}}(t)\frac{\tilde{a}_i\theta_i^*}{\tilde{d}_i} - \hat{\bar{c}}_i(t)\right] - (\gamma_i + 1)(\hat{\bar{E}}_i(t) + \hat{\bar{c}}_i(t)), \\
\frac{d\hat{\bar{c}}_i(t)}{dt} &= \frac{1}{\eta_i}\left[\hat{\bar{E}}_i(t)\hat{\bar{S}}(t)\frac{\tilde{a}_i\theta_i^*}{\tilde{d}_i} - \hat{\bar{c}}_i(t)\right], \\
\frac{d\bar{S}(t)}{dt} &= \bar{\alpha}_s(t) - \sum_{j=1}^{n}\frac{1}{\eta_j}\left[\hat{\bar{E}}_j(t)\hat{\bar{S}}(t)\frac{\tilde{a}_j\theta_j^*}{\tilde{d}_j} - \hat{\bar{c}}_i(t)\right] - (\gamma_s + 1)(\hat{\bar{S}}(t) + \sum_{j=1}^{n}\hat{\bar{c}}_j(t)),
\end{aligned} \tag{11a}$$

$$\theta_i^* = \begin{cases} \int_0^1 \hat{v}_{E_i}(x)\hat{v}_S(x)dx & \text{for Case I} \\ \hat{v}_S(x_i^*) & \text{for Case II} \\ \hat{v}_{E_i}(x_s^*) & \text{for Case III} \end{cases}, \tag{11b}$$

where $\hat{\bar{E}}_i(0) = \bar{E}_i(0)$, $\hat{\bar{S}}(0) = \bar{S}(0)$, $\hat{\bar{c}}_i(0) = \bar{c}_i(0)$, as given by (7), and $\hat{v}_{E_i}(x)$, $\hat{v}_{c_i}(x)$, and $\hat{v}_S(x)$ are given by (10). Then, we have the following main result of this paper (see SI Section 2.3, Theorem 3 for a formal statement with the proof).

Result 1. *Consider system* (6) *and let* $\boldsymbol{z}(t,x) = [E_1(t,x), \ldots, E_n(t,x), c_1(t,x), \ldots, c_n(t,x), S(t,x)]^T$ *with* $\bar{\boldsymbol{z}}(t) = \int_0^1 \boldsymbol{z}(t,x)dx$. *Consider system* (11) *and let* $\hat{\bar{\boldsymbol{z}}}(t) = [\hat{\bar{E}}_1(t), \ldots, \hat{\bar{E}}_n(t), \hat{\bar{c}}_1(t), \ldots, \hat{\bar{c}}_n(t), \hat{\bar{S}}(t)]^T$. *Then, for all* $t \geq 0$ *and* ϵ, δ *sufficiently small*

$$||\bar{\boldsymbol{z}}(t) - \hat{\bar{\boldsymbol{z}}}(t)|| = \begin{cases} \mathcal{O}(\epsilon) & \textit{for Case I} \\ \mathcal{O}(\epsilon) + \mathcal{O}(\delta) & \textit{for Case II, III} \end{cases}. \tag{12}$$

By virtue of this result, we can use the simple and convenient ODE model in equations (11) to describe the space-averaged dynamics of the PDE system (6). In particular, from (11) it appears that spatial effects are lumped into the BCF approximation θ_i^*. Therefore, in order to determine how spatial heterogeneity affects system dynamics, it is sufficient to analyze how dynamics is affected by parameter θ_i^* and how the expression of θ_i^* is, in turn, affected by spatial localization and molecule size (see (11b) and (2)).

Remark 1. As discussed in SI Section 2.3, as $\epsilon \to 0^+$, the spatial profile of diffusing molecules approaches that of their available volume profile, that is,

$$\underbrace{E_i(t,x) \approx \bar{E}_i(t)\hat{v}_{E,i}(x)}_{\text{Case I and Case III}}, \quad \underbrace{c_i(t,x) \approx \bar{c}_i(t)\hat{v}_{c,i}(x)}_{\text{Case I}}, \quad \underbrace{S(t,x) \approx \bar{S}(t)\hat{v}_S(x)}_{\text{Case I and Case II}},$$

for the other spatially fixed species we have that their concentrations are localized in a manner as their production terms .

The consequence of Remark 1 is that knowledge of the space averaged dynamics from system (11) also leads to knowledge of the spacial profiles of the species within the cell. This information is used to propose a method to estimate the BCF from experimental data (See SI Section 2.11)

Remark 2. The approximation result holds for $\epsilon \ll 1$, that is, diffusion is much faster than any other time scales in (6). However, in SI Section 2.4 we motivate why the approximation should still hold (for which the relationship (9) is key) if $\eta_i/\epsilon = \mathcal{O}(1)$ (binding and unbinding between E_i and S occurs at a similar timescale as diffusion), and confirmed via numerical simulations in Section 1.4.

The BCF θ_i^* in (11b) is temporally constant and thus the reduced model has the same dimensionality as the well-mixed model (8), yet captures the role of spatial heterogeneity in the interactions between cellular species. Therefore, θ_i^* is a practical and accurate approximation of the BCF when $\epsilon \ll 1$ (sufficient for Case I) and $\delta \ll 1$ (needed for Cases II-III).

1.3.2 Dependence of the BCF on species size and localization

When diffusion is fast and the expression of spatially fixed species is localized, the BCF is well approximated by θ_i^* given in (11b). Substituting (2) into (11b) and denoting the radius of gyration of E_i and S by $r_{e,i}$ and r_s, respectively, we can rewrite θ_i^* as

$$\theta_i^* = \begin{cases} \dfrac{\int_0^1 e^{-\frac{r_{e,i}^2+r_s^2}{(r^*)^2}\hat{\rho}(x)}dx}{[\int_0^1 e^{-(r_{e,i}/r^*)^2\hat{\rho}(x)}dx][\int_0^1 e^{-(r_s/r^*)^2\hat{\rho}(x)}dx]} & \text{for Case I} \\ \dfrac{e^{-(r_s/r^*)^2\hat{\rho}(x_i^*)}}{\int_0^1 e^{-(r_s/r^*)^2\hat{\rho}(x)}dx} & \text{for Case II} \\ \dfrac{e^{-(r_{e,i}/r^*)^2\hat{\rho}(x_s^*)}}{\int_0^1 e^{-(r_{e,i}/r^*)^2\hat{\rho}(x)}dx} & \text{for Case III} \end{cases} . \tag{13}$$

From (13), we observe that θ_i^*, depends on the spatial localization of spatially fixed species (i.e,. x_i^* and x_s^*), the radius of gyration of diffusing species, r^* (2), and the nominalized local density of DNA length $\hat{\rho}(x)$.

Using (13), we graphically illustrate the dependence of θ_i^* on $r_{e,i}$, r_s, r^*, x_i^* and x_s^* in Figure 4. By analyzing Figure 4, we observe the following:

Case I: the BCF is always greater than or equal to that of the well-mixed model (8) (where $\theta_i^* = 1$ for all i) and this discrepancy increases with the size of E_i and S. Intuitively, as the size of E_i and S increases, they are pushed out of the chromosome and co-localize near the cell poles, thus they are confined to a smaller volume to interact and hence their effective binding strength increases. If only one of the species is large (with respect to r^*), while the other one is small, then the large species will be ejected from the chromosome and thus will not be homogeneously distributed throughout the cell, however $\theta_i^* \approx 1$, and thus a well-mixed model is valid despite this spatial heterogeneity.

Case II and III: where one of the species diffuses (size r_y) and the other is fixed at $x = x^*$, the BFC is different from unity when r_y is sufficiently large. We observe that $\theta_i^* < 1$ for $x^* \leq 0.4$ and appears to approach zero near $x^* = 0$ for large r_y/r^*. Similarly, for $x^* \geq 0.65$, $\theta_i^* > 1$. This occurs because as the size of the diffusing species increases, the species is ejected from the chromosome onto the cell poles and therefore it is more likely to interact with species fixed at the cell-poles than those near mid-cell. Between $0.4 \leq x^* \leq 0.65$ there exists a region where $\theta_i^* = 1$ for all r_y/r^*. This provides additional evidence that a well-mixed model may be appropriate despite severe intracellular heterogeneity.

When $\hat{\rho}(x)$ is assumed to be a step function, the upper bound for θ_i^* is $1/\Delta x$ for Case I-III, as derived in SI Section 2.5, where Δx is the distance between the end of the chromosome and the cell poles as shown in Figure 1. Furthermore, the lower bound for Case I was unity and for Case II-III it was zero.

The value of the BCF provides a measure to determine the extent to which spatial effects modulate the biomolecular dynamics. Therefore, an experimental method to estimate the BCF is desirable. In SI Section 2.11, we propose such a method that only requires knowledge of Δx and of the value of concentration of freely diffusing species inside and outside the nucleoid.

In SI Section 2.13, we consider how the BCF can vary temporally as the cell divides and the chromosome density shifts from being concentrated primarily near mid-cell to quarter-cell. We demonstrate that the BCF can vary by over 50% in time for the case where one species is stationary and localized near mid-cell. Furthermore, in SI Section 2.14 we show how the BCF is affected when we consider exclusion effects from the DNA of a pole localized high copy plasmid. We show that for the case where both reactant freely diffuse, the BCF decreases as the amount of plasmid DNA increases. For the case where one reactant is spatially fixed and the other freely diffuses, we show that the BCF decreases for a species localized at the cell poles and increases for a species localized near quarter-cell, as the amount of plasmid DNA increases.

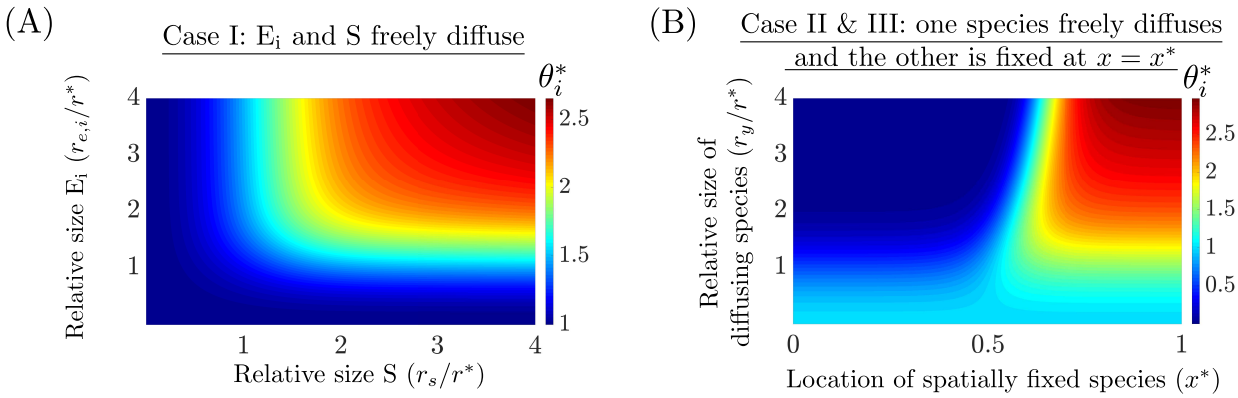

Figure 4: **The BCF in the limit of fast diffusion and localization of spatially fixed species**. Approximation of the BCF denoted by θ_i^* (13) is provided for Case I and for Case II/Case III. (A) For Case I, where $\mathrm{E_i}$ and S both freely diffuse, $\theta_i \geq 1$ and increases when both the size of $\mathrm{E_i}$ ($r_{e,i}$) and S (r_s) are sufficiently large (with respect to r^*). (B) For Case II and III, where one of the species diffuses (size r_y) and the other is fixed at $x = x^*$, θ_i^* is different from unity when the radii of the diffusion species is sufficiently large. We observe that $\theta_i^* < 1$ for $x^* \leq 0.4$ and appears to approach zero near $x^* = 0$ for large r_y/r^*. Similarly, for $x^* \geq 0.65$, $\theta_i^* > 1$. Between $0.4 \leq x^* \leq 0.65$ there exists a region that $\theta_i^* = 1$ for all r_y/r^*.

1.4 Application to Core Processes and Genetic Circuits

In this section we apply the results of the time scale separation analysis from Section 1.3 in order to both determine and modulate the effects of intracellular heterogeneity on core processes, such as transcription and translation, and on genetic circuit behavior.

1.4.1 Application of the reduced ODE model to transcription and translation

In this section, we investigate how and the extent to which intracellular heterogeneity affects the core biological processes of transcription and translation, which are responsible for protein production. We model a gene (D) being transcribed by RNAP (S) to form a DNA-RNAP complex ($\mathrm{c_s}$) to produce mRNA (m). The mRNA is then translated by ribosomes (R) to form mRNA-ribosome complex ($\mathrm{c_m}$) which produces protein P. The chemical reactions are given by

$$\underbrace{\mathrm{D} + \mathrm{S} \underset{\mathrm{d_s}}{\overset{\mathrm{a_s}}{\rightleftharpoons}} \mathrm{c_s} \xrightarrow{\kappa_\mathrm{s}} \mathrm{m} + \mathrm{S} + \mathrm{D}}_{\text{transcription, Case II}}, \quad \underbrace{\mathrm{m} + \mathrm{R} \underset{\mathrm{d_m}}{\overset{\mathrm{a_m}}{\rightleftharpoons}} \mathrm{c_m} \xrightarrow{\kappa_\mathrm{m}} \mathrm{P} + \mathrm{R} + \mathrm{m}}_{\text{translation, Case I}}, \quad \mathrm{P} \xrightarrow{\mu} \emptyset, \tag{14}$$

$$\mathrm{c_s} \xrightarrow{\mu} \emptyset, \quad \emptyset \xrightarrow{\alpha_\mathrm{s}} \mathrm{S} \xrightarrow{\mu} \emptyset, \quad \mathrm{m} \xrightarrow{\gamma+\mu} \emptyset, \quad \mathrm{c_m} \xrightarrow{\gamma} \mathrm{R} \quad \mathrm{c_m} \xrightarrow{\mu} \emptyset \quad \emptyset \xrightarrow{\alpha_\mathrm{r}} \mathrm{R} \xrightarrow{\mu} \emptyset,$$

where a_s and d_s are the association and dissociation rate constants, respectively, between RNAP and the gene D, κ_s is the catalytic rate constant of formation of mRNA m, a_m and d_m are the association and dissociation rate constants, respectively, between ribosomes and mRNA, κ_m is the catalytic rate constant of formation of protein P, α_s is the production rate of RNAP, α_r is the ribosome production rate, μ is the cell growth rate constant (set to unity in our nondimensionalization), and γ is the mRNA degradation rate constant. The transcription reaction is in the form of Case II (Table 1) since the gene does not freely diffuse and the RNAP freely diffuses. The translation process falls under Case I, since both mRNA and ribosomes freely diffuse. We assume that the total concentration of D is conserved, so that $D_T(x) = D(t,x) + c_s(t,x)$ and that $D_T(x)$ is localized at $x = x^*$. From (11), the dimensionless reduced space averaged dynamics corresponding to (14)

are given by

$$\begin{aligned}
\frac{d\bar{c}_s(t)}{dt} &= a_s\theta_s^*\bar{D}(t)\bar{S}(t) - (d_s+\kappa_s+1)\bar{c}_s(t),\\
\frac{d\bar{S}(t)}{dt} &= \bar{\alpha}_s(t) - a_s\theta_s^*\bar{D}(t)\bar{S}(t) + (\kappa_s+d_s)\bar{c}(t) - \bar{S}(t),\\
\frac{d\bar{m}(t)}{dt} &= \kappa_s\bar{c}_s(t) - a_m\theta_R^*\bar{R}(t)\bar{m}(t) + (d_m+\kappa_m)\bar{c}(t) - (\gamma+1)\bar{m}(t)\\
\frac{d\bar{c}_m(t)}{dt} &= a_m\theta_R^*\bar{R}(t)\bar{m}(t) - (d_m+\kappa_m+1+\gamma)\bar{c}(t),\\
\frac{d\bar{R}(t)}{dt} &= \bar{\alpha}_r(t) - a_m\theta_R^*\bar{R}(t)\bar{m}(t) + (\gamma+d_m+\kappa_m)\bar{c}_m(t) - \bar{R}(t), \quad \frac{d\bar{P}(t)}{dt} = \kappa_m\bar{c}_m(t) - \bar{P}(t).
\end{aligned} \tag{15}$$

Concentration variables are nondimensionalized with respect to the total steady state space averaged RNAP ($\bar{S}_T(\infty) = \bar{\alpha}_s(\infty)/\mu$), since this quantity is a readily available in the literature. Letting r_s, r_m, and r_R, be the radius of gyration of RNAP, mRNA, and ribosomes, respectively, we compute the BCF's via (11b) and (2),

$$\theta_s^* = \hat{v}_s(x^*) = \frac{e^{-(r_s/r^*)^2\hat{\rho}(x^*)}}{\int_0^1 e^{-(r_s/r^*)^2\hat{\rho}(x)}dx}, \tag{16a}$$

$$\theta_R^* = \int_0^1 \hat{v}_m(x)\hat{v}_R(x)dx = \frac{\int_0^1 e^{-\frac{r_m^2+r_R^2}{(r^*)^2}\hat{\rho}(x)}dx}{[\int_0^1 e^{-(r_m/r^*)^2\hat{\rho}(x)}dx][\int_0^1 e^{-(r_R/r^*)^2\hat{\rho}(x)}dx]}, \tag{16b}$$

where $\hat{v}_s(x) = \frac{v_s(x)}{\int_0^1 v_s(x)dx}$, $\hat{v}_m(x) = \frac{v_m(x)}{\int_0^1 v_m(x)dx}$, $\hat{v}_R(x) = \frac{v_R(x)}{\int_0^1 v_R(x)dx}$, and $\hat{v}_c(x) = \frac{v_c(x)}{\int_0^1 v_c(x)dx}$ are the normalized available volume profiles of RNAP, mRNA, ribosomes, and of the mRNA-ribosome complex, respectively. Recall that the quantity $(r^*)^2$ is inversely proportional to the total DNA length per volume. We now consider the steady state behavior of system (15) by equating the time derivatives to zero. Specifically, we are interested in how the steady state levels of produced mRNA and protein are affected by θ_s^* and θ_r^* and, hence, how they depend on spatial quantities such as r_s/r^* r_m/r^*, r_R/r^*, and x^*.

Total mRNA steady state level: We are interested in investigating the role of spatial effects on the binding between RNAP and the DNA and thus on mRNA production. Here we analyze the steady state total mRNA levels ($\bar{m}_T = \bar{m} + \bar{c}_m$) of (15) rather than the free amount of mRNA (m), since $\bar{m}_T$ is independent of θ_R^* as shown by

$$\bar{m}_T = \kappa_s\bar{c}_s/(\gamma+1) \text{ with } \quad \bar{c}_s = \bar{D}_T\frac{\bar{S}\theta_S^*/K_s}{1+\bar{S}\theta_S^*/K_s}, \tag{17}$$

where $\bar{D}_T = \int_0^1 D_T(x)dx$, $K_s = d_s/a_s$, $K_R = d_m/a_m$. If $\theta_S^* = 1$ in (17), then the predicted total mRNA steady state level will be identical to that of a well-mixed model (as in (8)). From (16) and Figure 4-B, if the RNAP radius of gyration is sufficiently large with respect to r^* then θ_S^* may be different from unity (depending on x^*), in which case spatial effects arise. If the DNA is localized near mid-cell ($x^* \approx 0$), then it implies that $\theta_S^* < 1$ from Figure 4-B and, as a consequence, a decreased steady state total mRNA level will result. Furthermore, for very large values of r_s/r^* and $x^* \approx 0$ we have that $\theta_S^* \to 0$ and the total mRNA steady state levels will approach zero. Similarly, if the DNA is localized near the cell-poles ($x^* \approx 1$), then it implies that $\theta_S^* > 1$ from Figure 4-B and, as a consequence, an increased steady state total mRNA level. This phenomenon occurs because as the excluded volume effects of RNAP are amplified (large r_s/r^*), RNAP will localize primarily in the cell poles and hence transcribe pole-localized DNA more efficiently than DNA near mid-cell (or any region where the local chromosome density is high). When designing genetic circuits, a plasmid backbone is chosen to provide a certain DNA copy number, however the backbone also determines where in the cell the plasmid localizes [9, 10, 11]. Therefore, based on our results, localization also affects steady state total mRNA level. If instead of introducing the DNA via a plasmid, the DNA is integrated directly into the chromosome, then the location of integration site should be a parameter to consider.

Figure 5-A shows the behavior of the steady state total mRNA level as a function of r_s/r^* and of the location of the transcribed gene, when compared to the level predicted by the well mixed model. Simulations confirm that total mRNA levels are higher for pole localized genes than those near mid-cell and that the discrepancy increases with the size of RNAP relative to r^*. The agreement between the full PDE model ((62) in SI Section 2.6) and the reduced ODE model (15) provides numerical validation of the model reduction

results (explicitly shown in SI Figure 11). In the SI Section 2.6, we show in Figure 9 the transient response corresponding to Figure 5, for which the full-PDE and reduced models agree. Furthermore, in SI Figure 9, we also verify that as the size of RNAP increases, it is indeed ejected from the chromosome and adopts its available volume profile (Remark 1). Furthermore, in SI-Figure 10, we demonstrate that these results hold independent of the binding and unbinding speed between RNAP and DNA (Remark 2). In SI Section 2.12 we propose an experimental method to test the hypothesis that mid-cell genes are transcribed less effectively than pole localized genes.

In [28] it was estimated that $r_s = 6.5 \pm 0.1$ nm, which implies that $r_s/r^* \approx 0.3$. From Figure 4-B, this implies that $\theta_s^* \approx 1.06$ when the DNA is at the cell poles and $\theta_s^* \approx 0.94$ when the DNA is near mid-cell, thus the we expect the binding strength between RNAP and the DNA to deviate by 6% from that of a well-mixed model. From (17), if $S\theta_S^*/K_s << 1$, then $\bar{m}_T = \frac{\theta_S^* \kappa_s \bar{D}_T \bar{S}}{K_s(\gamma+1)}$; thus in this regime the mRNA concentration is proportional to θ_S^*. So we expect at most a 6% difference in steady state mRNA concentration with respect to what is predicted by a well-mixed model.

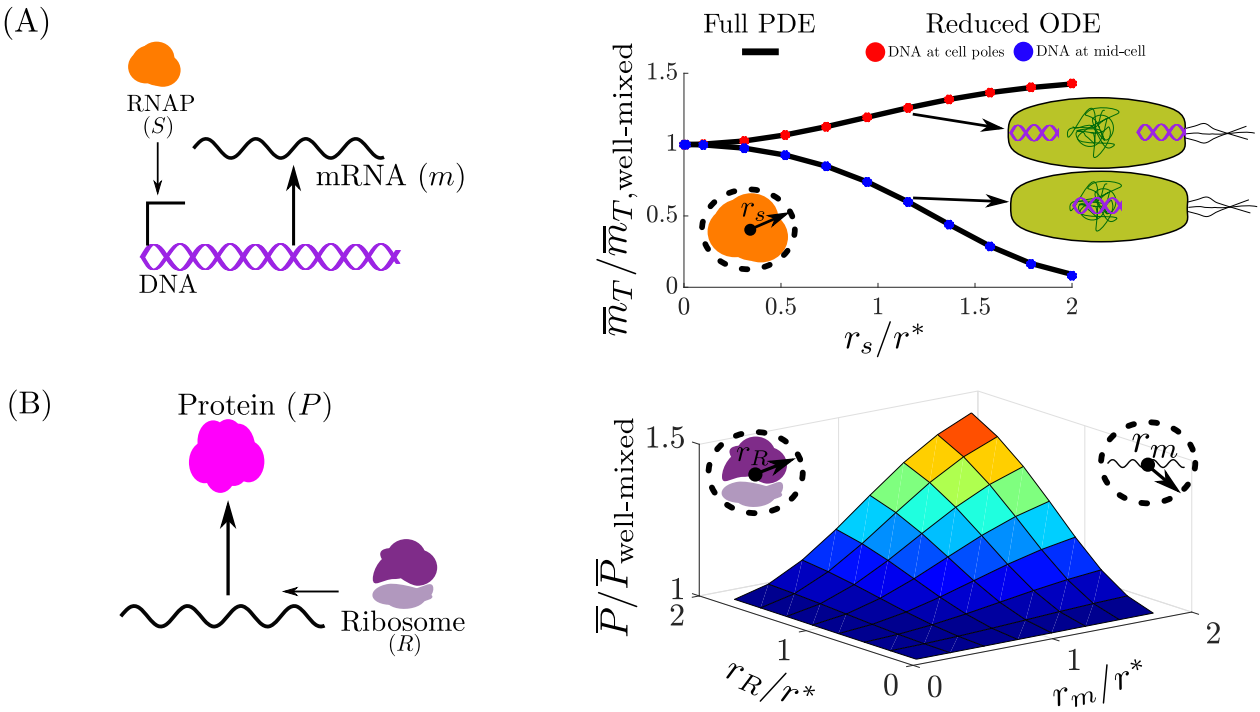

Figure 5: **Spatial heterogeneity effects on steady state total mRNA and protein levels** (A) The space averaged total mRNA ($\bar{m}_T$) concentration predicted by the full PDE model ((62) in SI Section 2.6) and the reduced ODE model (15) normalized by that of the well-mixed model ($\bar{m}_{T,\text{well-mixed}}$) as the size of the RNAP (r_s) varies with respect to r^*. With respect to the well-mixed model, the amount of mRNA decreases (increases) when the DNA is localized near mid-cell (cell poles). (B) The space averaged protein concentration ($\bar{P}$) predicted by the full PDE model ((62) in SI Section 2.6) normalized by that of the well-mixed model ($\bar{P}_{\text{well-mixed}}$) as the size of the of mRNA (r_m) and ribosome (r_R) varies with respect to r^*. The amount of protein increases when both the mRNA and ribosome size increases. We set $r_s/r^* = 1 \times 10^{-3}$, such that $\theta_S \approx 1$ and thus the result is independent of the spatial location where the gene is expressed. We refer to the well-mixed model as (15) with (16) given by $\theta_S^* = 1$ and $\theta_R^* = 1$. The parameter values and full simulation details are provided in SI Section 2.6

Protein steady state level: The steady state protein levels of (15) are given by

$$\bar{P} = \kappa_m \bar{c}_m, \quad \text{with} \quad \bar{c}_m(t) = \bar{m}_T \frac{\bar{R}/K_R\theta_R^*}{1 + \bar{R}/K_R\theta_R^*}. \tag{18}$$

From (17) and (18), if $\theta_S^* = 1$ and $\theta_R^* = 1$, then protein steady state level will be identical to that of a well-mixed model. From (16) and Figure 4-A, we conclude that $\theta_R^* \geq 1$ and increases with r_s/r^* and r_m/r^*. Increasing r_s/r^* and r_m/r^* implies that the ribosomes and mRNA are further excluded from the

chromosome onto the cell poles. Once localized at the cell-poles, the mRNA and ribosomes are more likely to bind. Figure 5-B shows the behavior of the steady state protein levels as a function of r_m and r_R, when compared to the level predicted by the well mixed-model for the full PDE model ((62) in SI Section 2.6). Simulations confirm that protein levels with respect to a well-mixed model increases when both the mRNA and ribosome size are sufficiently large. In SI-Figure 13, we show that the reduced ODE model (15) is within 2% of the full PDE model (SI (62)) for the result in Figure 5-B. In the SI Section 2.6 we show in Figure 12 the transient response corresponding to Figure 5, for which the full-PDE and reduced model agree. Furthermore, in SI Figure 12 we verify that as the size of ribosome and mRNA increase, they are ejected from the chromosome and and become distributed according to their available volume profile (Remark 1). Furthermore, in SI-Figure 14-15, we demonstrate that these results hold independent of the binding and unbinding speed between ribosomes and mRNA (Remark 2).

It is well known that most mRNA-ribosome complexes exists in configurations with multiple ribosomes bounded (polysomes) [29, 30]. To capture the prevalence of these polysomes, we model the translation process accounting for the fact that one mRNA can be bound to multiple ribosomes. We first model the mRNA binding simultaneously to $N_r - 1$ ribosomes to form the $\mathrm{c_l}$ complex, to which another ribosome binds to to form the fully loaded $\mathrm{c_t}$ complex. The leading ribosome with a complete peptide is released from $\mathrm{c_t}$ at a rate κ_t to yield protein P. This is described by the following set of biochemical reactions:

$$\underbrace{\mathrm{m} + (\mathrm{N_r} - 1)\mathrm{R} \underset{\mathrm{d_l}}{\overset{\mathrm{a_l}}{\rightleftharpoons}} \mathrm{c_l}}_{\text{ribosome loading}}, \quad \mathrm{c_l} + \mathrm{R} \underset{\mathrm{d_t}}{\overset{\mathrm{a_t}}{\rightleftharpoons}} \underbrace{\mathrm{c_t} \xrightarrow{\kappa_t} \mathrm{P} + \mathrm{R} + \mathrm{c_l}}_{\text{peptide release}}. \tag{19}$$

While the ribosome loading reaction in (19) is not in the form of the chemical reactions (1), which assume bimolecular reactions, we can nevertheless apply our results as follows (see SI Section 2.7 for details). Specifically, ribosome and mRNA profiles will still approach their available volume profiles (Remark 1), that is, $R(t,x) \approx \bar{R}(t)\hat{v}_r(x)$, $m(t,x) \approx \bar{m}(t)\hat{v}_m(x)$, and $c_l(t,x) \approx \bar{c}_l(t)\hat{v}_{c_l}(x)$ where $v_{c_l}(x) = v_r^{N_r-1}(x)v_m(x)$ (recall (9)) and $\hat{v}_{c_l}(x) = v_{c_l}(x)/[\int_0^1 v_{c_l}dx]$. This is verified through simulations in SI Section 2.7, Figure 16. By virtue of the reactants in (19) mirroring their available volume profiles and (7b), we can approximate the BCF of the loading θ_l^* and translation θ_t^* reactions in (19), given as

$$\theta_l^* = \frac{\int_0^1 v_m(x)v_R^{N_r-1}(x)dx}{[\int_0^1 v_m(x)dx][\int_0^1 v_R(x)dx]^{N_r-1}} = \frac{\int_0^1 e^{-\frac{r_m^2+(\sqrt{N_r-1}r_R)^2}{(r^*)^2}\hat{\rho}(x)}dx}{[\int_0^1 e^{-(r_m/r^*)^2\hat{\rho}(x)}dx][\int_0^1 e^{-(r_R/r^*)^2\hat{\rho}(x)}dx]^{N_r-1}}.$$

$$\theta_t^* = \frac{\int_0^1 v_{c_l}(x)v_R(x)dx}{[\int_0^1 v_{c_l}(x)dx][\int_0^1 v_R(x)dx]} = \frac{\int_0^1 e^{-\frac{r_m^2+(\sqrt{N_r}r_R)^2}{(r^*)^2}\hat{\rho}(x)}dx}{[\int_0^1 e^{-\frac{r_m^2+(\sqrt{N_r-1}r_R)^2}{(r^*)^2}\hat{\rho}(x)}dx][\int_0^1 e^{-(r_R/r^*)^2\hat{\rho}(x)}dx]}.$$

In SI Section 2.7, Figure 16-D, we show computationally that θ_l^* and θ_t^* are good approximations to the BCF. At this point, we can write the ODE corresponding to this system of reactions and just modify the association rate constants by θ_l^* and θ_t^*, as shown in SI Section 2.7, Equation (66). Let $K_d = (d_l/a_l)^{1/(N_r-1)}$, $K_t = (d_t + \kappa_t)/a_t$, $\beta_l = (\gamma+1)/d_l$, and $\beta_t = (\gamma+1)/(\kappa_t + d_t)$, if $\beta_l, \beta_t, \bar{R}/K_t \ll 1$ (dilution and mRNA degradation is much slower than the rate of ribosome unbinding and K_t is sufficiently large comparer to $\bar{R}$ [52]), then a simple expression for the steady state protein concentration is given by

$$\bar{P} = \kappa_t \bar{m}_T \theta_t^* \bar{R}/K_t \underbrace{\frac{\theta_l^*(\bar{R}/K_d)^{N_r-1}}{1+\theta_l^*(\bar{R}/K_d)^{N_r-1}}}_{\text{ribosome loading}}, \tag{20}$$

where $\bar{m}_T$ is given by (17).

In [13] it was estimated that $r_m = 20$ nm and $r_R = 10$ nm, which implies that $r_m/r^* \approx 0.88$ and $r_R/r^* \approx 0.44$. Assuming the average distance between ribosomes on an mRNA to be 70 nucleotides [31], for a 700 nucleotide mRNA (e.g., GFP or RFP), then we have $N_r = 10$. Thus, for these values, $\theta_l^* \approx 1.56$ and $\theta_t^* \approx 1.07$. This implies that the forward rate in the reaction of 9 ribosomes binding to an mRNA (a_l) is amplified by 56% and the rate at which an additional ribosome binds to this complex (a_t) increases by 7% with respect to a well-mixed model. From (20), this would imply up to 67% increase in protein production with respect to a well-mixed model.

Taken together, these results suggest that while a well-mixed ODE model may be sufficient to describe transcription, it is not sufficiently descriptive to capture spatial effects on translation. In this case,the BCF should be incorporated in the ODE. Additionally, these results are indicative that for other processes in the cell where complexes of similar size as polysomes are formed, then spatial effects will likely be substantial.

1.4.2 Gene expression regulation by transcription factors

Regulation of gene expression is often performed by transcription factors (TFs) [1]. A transcription factor can either enhance (for activators) or repress (for repressors) transcription. Spatial affects play an identical role in gene regulation via activators as they do in gene regulation via RNAP (Figure 5), thus we focus on transcriptional repressors. In this section, we model transcription regulation where a repressor $\mathrm{P_r}$ dimerizes to form dimer $\mathrm{c_1}$ (e.g., TetR dimerizes before binding to a gene [32]) and then blocks transcription of gene D that produces protein P. The biochemical reactions corresponding to this process are:

$$\emptyset \xrightarrow{\alpha} \mathrm{P_r}, \quad \underbrace{\mathrm{P_r} + \mathrm{P_r} \underset{\mathrm{d_1}}{\overset{\mathrm{a_1}}{\rightleftharpoons}} \mathrm{c_1}}_{\text{Case I}}, \quad \underbrace{\mathrm{c_1} + \mathrm{D} \underset{\mathrm{d_2}}{\overset{\mathrm{a_2}}{\rightleftharpoons}} \mathrm{c_2}}_{\text{Case II}}, \quad \mathrm{D} \xrightarrow{\kappa} \mathrm{P}, \quad \mathrm{P_r} \xrightarrow{\gamma_\mathrm{r}} \emptyset, \quad \mathrm{P} \xrightarrow{\gamma_\mathrm{p}} \emptyset, \tag{21}$$

where α is the production rate of $\mathrm{P_r}$, a_1 (d_1) is the association (dissociation) rate constant to form the $\mathrm{c_1}$ complex, a_2 (d_2) is the association (dissociation) rate constant to form the $\mathrm{c_2}$ complex, κ is the catalytic rate constant to produce protein P, and γ_r and γ_p are the degradation rate constant of P_r and P, respectively. Notice that we have lumped the transcription and translation process to produce $\mathrm{P_r}$ into one production reaction and similarly for P. From the results of Section 1.4.1, we know that $\bar{\alpha}(t)$ depends on the location where $\mathrm{P_r}$ is expressed (higher if its coding DNA is near the cell poles than mid-cell) and the size of it's mRNA (higher for longer mRNAs). Similarly, κ depends on the location where $\mathrm{P_r}$ is expressed and it's mRNA size. Using the results from Section 1.4.1 we can explicitly model these dependences, however, we opt not to do so to solely investigate the role of spatial effects on transcriptional repression. Since the repressor $\mathrm{P_r}$, freely diffuses, the dimerization reaction belongs to Case I. The gene D is spatially fixed and it is repressed by the freely diffusing $\mathrm{c_1}$, thus this interaction falls under Case II. We assume that the total concentration of D is conserved, so that $D_T(x) = D(t,x) + c_2(t,x)$ and that $D_T(x)$ is localized at $x = x^*$. The reduced ODE model corresponding to (21) obeys

$$\begin{aligned} &\frac{d\bar{P}_r(t)}{dt} = \bar{\alpha}(t) - \gamma_r \bar{P}_r(t), \quad \frac{d\bar{c}_1(t)}{dt} = a_1\theta_1^* \bar{P}_r^2(t) - d_1 c_1(t) - a_2\theta_2^* \bar{c}_1(t)\bar{D}(t) + d_2\bar{c}_2(t), \\ &\frac{d\bar{c}_2(t)}{dt} = a_2\theta_2^*\bar{D}(t)\bar{c}_i(t) - d_2\bar{c}_2(t), \quad \bar{D}(t) = 1 - \bar{c}_2(t), \quad \frac{d\bar{P}(t)}{dt} = \kappa\bar{D}(t) - \gamma_p\bar{P}(t). \end{aligned} \tag{22}$$

Concentration variables were nondimensionalized with respect to the space averaged total DNA $\bar{D}_T = \int_0^1 D_T(x)dx$. From our main result, the BCF's are given by

$$\theta_1^* = \int_0^1 \hat{v}_{P_r}^2(x)dx = \frac{\int_0^1 v_{P_r}^2(x)dx}{[\int_0^1 v_{P_r}(x)dx]^2}, \quad \theta_2^* = \hat{v}_{c_1}(x^*) = \frac{v_{c_1}(x^*)}{\int_0^1 v_{c_1}(x)dx}, \quad v_{P_r}(x) = e^{-(r/r^*)^2\hat{\rho}(x)}, \tag{23}$$

where r is the radius of gyration of $\mathrm{P_r}$, $v_{P_r}(x)$ and $v_{c_1}(x)$ are the available volume profiles of $\mathrm{P_r}$ and $\mathrm{c_1}$, respectively, and from (9), $v_{c_1}(x) = v_{P_r}^2(x)$.

We now consider the steady state behavior of system (22) by equating the time derivatives to zero. Specifically, we are interested in how the steady state levels of P is affected by the spatial quantities r/r^* and x^*. From setting (22) to steady state, we obtain

$$\bar{P} = \frac{\kappa}{\gamma_p}\bar{D}, \quad \text{where} \quad \bar{D} = \frac{1}{1 + (\bar{P}_r/K)^2\theta^*}, \quad \theta^* = \theta_1^*\theta_2^* = \hat{v}_{P_r}^2(x^*), \tag{24}$$

where $K = \sqrt{K_{d,1}K_{d,2}}$ and $K_{d,i} = d_i/a_i$ for $i = 1, 2$. From (24) and (23), we observe that θ^* contains all the spatial information, which includes the size of $\mathrm{P_r}$ and the location of the target gene D. If $\theta^* = 1$, then the protein concentration would be the same as the well-mixed model. The ratio $K/\sqrt{\theta^*}$ can be thought of as an effective disassociation rate constant of the repressor. If D is located near mid-cell ($x^* \approx 0$ in (23)), then for $r/r^* \ll 1$ we have $\theta^* \approx 1$ (see Figure 4), but as r/r^* increases, we have that $\theta^* < 1$ and asymptotically approaches zero as $r/r^* \to \infty$. Similarly, if D is located near the cell poles ($x^* \approx 1$ in (23)), then for

$r/r^* \ll 1$ we have $\theta^* \approx 1$ (see Figure 4), but as r/r^* increases, we have that $\theta^* > 1$. Thus, the efficacy of a transcriptional repressor regulating genes in the chromosome (cell-poles) decreases (increases) with TF size. Intuitively, this occurs because as the TF size increases, excluded volume effects will push it out of the chromosome onto the cell-poles (see Remark 1), thus interacting with DNA near the cell-poles more frequently than with DNA near mid-cell. Numerical simulations validate our predictions as shown in Figure 6, where increasing the transcription factor size leads to higher (lower) repression when the target DNA is localized at the cell poles (mid-cell) with respect to a well-mixed model. The simulation results also show agreement between the predictions of the full PDE ((70) in SI Section 2.8) and reduced ODE model (22) (as shown explicitly in SI Figure 19). Figure 17 in SI Section 2.8, further shows the temporal trajectories corresponding to Figure 6, also showing agreement between the full PDE model and the reduced ODE model. Finally, all our results hold independent of the binding and unbinding speeds of the transcription factor dimerizing and of the dimer binding to the DNA (Figure 18 in SI Section 2.8). In SI Section 2.12 we propose an experimental method to test the hypothesis that mid-cell genes are regulated less effectively than pole localized genes.

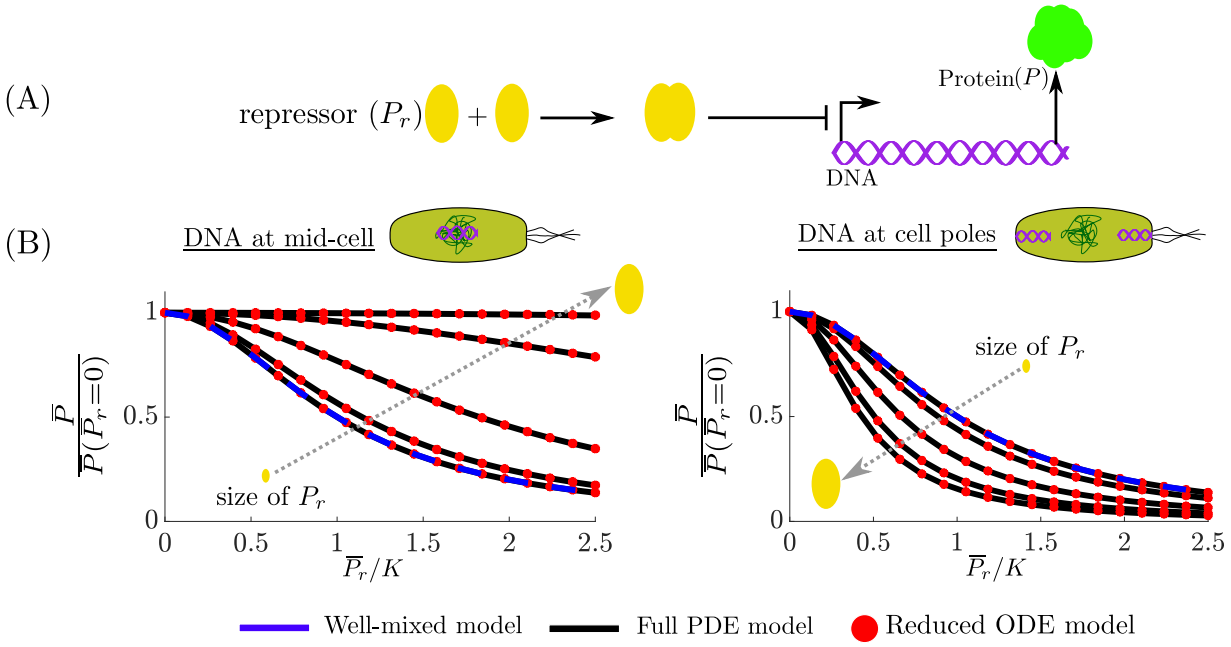

Figure 6: **Spatial heterogeneity effects in transcriptional regulation**. (A) The repressor P_r dimerizes and regulates the production of protein P. (B) The steady state space-averaged concentration per-cell of $\bar{P}$ normalized by its value when $\bar{P}_r = 0$ (24) for the PDE model ((70) in SI Section 2.8), the well-mixed model ((22) with $\theta_1^* = \theta_2^* = 1$), and the reduced ODE model (22) when the DNA is located near mid-cell ($x^* \approx 0$ in (24)) and when the DNA is located at the cell-poles ($x^* \approx 1$) for several sizes of P_r. The parameter values and full simulation details are provided in SI Section 2.8.

The reactions in (21) can be easily extended to CRISPRi/dCas9 repression systems [33], where instead of two identical species dimerizing, we have two distinct freely diffusing species bind (dCas9 and guide RNA) to form the complex gRNA-dCas9, which targets a desired DNA sequence. Exploiting the insight gained from analyzing (21), we expect that due to the large size of dCas9 [34] (which is further augmented as it forms a complex with the gRNA), it will regulate pole localized DNA (e.g,. ColE1 plasmid DNA [9]) more efficiently than genes in mid-cell (e.g,. chromosomally integrated) and thus spatial effects are expected to be more significant when using CRISPRi/dCas9 in genetic circuit design. Specifically, based on approximate values found in the literature, we estimated that $\theta^* \approx 1$ for a transcription factor, while θ^* can range between 0.9 and 1.1 for dCas9-enabled repression. This indicates that a well-mixed model is appropriate for modeling transcription factor-enabled repression of gene expression but may not be sufficient to capture effects of spatial heterogeneity arising with larger repressing complexes such as with dCas9/gRNA (see SI Section 2.8 for details).

1.4.3 Genetic Oscillator

As a final example, we consider the repressor-activator clock genetic circuit designed in [35] and shown in Figure 7-A. This circuit produces sustained oscillations if tuned within an appropriate parameter range [36, 1]. The circuit consists of two proteins $\mathrm{P_a}$ and $\mathrm{P_r}$. Protein $\mathrm{P_a}$, is an activator which dimerizes to form $\mathrm{P_{a,2}}$ and then binds to its own gene $\mathrm{D_a}$ to form complex $\mathrm{c_{a,1}}$ to initiate transcription. The dimer $\mathrm{P_{a,2}}$ also binds to the gene $\mathrm{D_r}$, which transcribes $\mathrm{P_r}$ to form complex $\mathrm{c_{a,2}}$ and initiates transcription. Protein $\mathrm{P_r}$, dimerizes to form $\mathrm{P_{r,2}}$ and then represses $\mathrm{P_a}$ by binding to $\mathrm{D_a}$ to form complex $\mathrm{c_r}$. The biochemical reactions corresponding to this circuit are:

$$\underbrace{\mathrm{P_a} + \mathrm{P_a} \underset{\mathrm{d_1}}{\overset{\mathrm{a_1}}{\rightleftharpoons}} \mathrm{P_{a,2}},}_{\text{Case I, } \mathrm{P}_a \text{ diffuses}} \quad \underbrace{\mathrm{P_r} + \mathrm{P_r} \underset{\mathrm{d_2}}{\overset{\mathrm{a_2}}{\rightleftharpoons}} \mathrm{P_{r,2}},}_{\text{Case II, } \mathrm{P}_r \text{ diffuses}} \quad \underbrace{\mathrm{P_{a,2}} + \mathrm{D_a} \underset{\mathrm{d_3}}{\overset{\mathrm{a_3}}{\rightleftharpoons}} \mathrm{c_{a,1}}, \quad \mathrm{P_{r,2}} + \mathrm{D_a} \underset{\mathrm{d_5}}{\overset{\mathrm{a_5}}{\rightleftharpoons}} \mathrm{c_r},}_{\text{Case III, } \mathrm{P}_{a,2} \text{ and } \mathrm{P}_{r,2} \text{ diffuse and } \mathrm{D_a} \text{ fixed}} \quad \underbrace{\mathrm{P_{a,2}} + \mathrm{D_r} \underset{\mathrm{d_4}}{\overset{\mathrm{a_4}}{\rightleftharpoons}} \mathrm{c_{a,2}},}_{\text{Case II, } \mathrm{P}_{a,2} \text{ diffuse and } \mathrm{D_r} \text{ fixed}}$$

$$\mathrm{D_a} \xrightarrow{\kappa_1} \mathrm{P_a}, \quad \mathrm{D_r} \xrightarrow{\kappa_2} \mathrm{P_r}, \quad \mathrm{P_a} \xrightarrow{\gamma_a} \emptyset, \quad \mathrm{P_r} \xrightarrow{\gamma_r} \emptyset, \quad \mathrm{c_{a,1}} \xrightarrow{\kappa_3} \mathrm{P_a}, \quad \mathrm{c_{a,2}} \xrightarrow{\kappa_4} \mathrm{P_r}, \tag{25}$$

where a_i (d_i) for $i = 1, \ldots, 5$ are association (dissociation) rate constants, γ_a (γ_r) is the degradation rate constant of $\mathrm{P_a}$ ($\mathrm{P_r}$) κ_1 (κ_2) is the basal rate at which gene $\mathrm{D_a}$ ($\mathrm{D_r}$) is transcribed, and κ_3 (κ_4) is the rate at which the DNA-transcription-factor complexes are transcribed for $\mathrm{D_a}$ ($\mathrm{D_r}$). We assume that the total concentration of $\mathrm{D_a}$ is conserved, so that $D_{a,T}(x) = D_a(t,x) + c_{a,1}(t,x) + c_r(t,x)$ and that $\mathrm{D_{a,T}}$ is localized at $x = x_a^*$. Similarly, we assume that the total concentration of $\mathrm{D_r}$ is conserved, so that $D_{r,T}(x) = D_r(t,x) + c_{a,2}(t,x)$ and that $\mathrm{D_{r,T}}$ is localized at $x = x_r^*$. The reduced ODE model corresponding to (25) is given by:

$$\begin{aligned}
\frac{d\bar{P}_a(t)}{dt} =& \kappa_1 \bar{D}_a(t) + \kappa_3 \bar{c}_{a,1}(t) - \gamma_a \bar{P}_a(t), \quad \frac{d\bar{P}_r(t)}{dt} = \kappa_2 \bar{D}_r(t) + \kappa_4 \bar{c}_{a,2}(t) - \gamma_r \bar{P}_r(t), \\
\frac{d\bar{P}_{a,2}(t)}{dt} =& a_1\theta_1^* \bar{P}_a^2(t) - d_1 \bar{P}_{a,2}(t) - a_3\theta_3^* \bar{P}_{a,2}(t)\bar{D}_a(t) + d_3 \bar{c}_{a,1}(t) - a_4\theta_4^* \bar{P}_{a,2}(t)\bar{D}_r(t) + d_4 \bar{c}_{a,2}(t), \\
\frac{d\bar{P}_{r,2}(t)}{dt} =& a_2\theta_2^* \bar{P}_r^2(t) - d_2 \bar{P}_{r,2}(t) - a_5\theta_5^* \bar{P}_{r,2}(t)\bar{D}_a(t) + d_5 \bar{c}_r(t), \quad \frac{d\bar{c}_{a,1}(t)}{dt} = a_3\theta_3^* \bar{P}_{a,2}(t)\bar{D}_a(t) - d_3 \bar{c}_{a,1}(t), \\
\frac{d\bar{c}_{a,2}(t)}{dt} =& a_4\theta_4^* \bar{P}_{a,2}(t)\bar{D}_r(t) - d_4 \bar{c}_{a,2}(t), \quad \frac{d\bar{c}_r(t)}{dt} = a_5\theta_5^* \bar{P}_{r,2}(t)\bar{D}_a(t) - d_5 \bar{c}_r(t), \\
\bar{D}_a(t) =& 1 - \bar{c}_{a,1}(t) - \bar{c}_r(t), \quad \bar{D}_r(t) = \bar{D}_{r,T} - \bar{c}_{a,2}(t).
\end{aligned} \tag{26a}$$

Concentration variables were nondimensionalized with respect to the space averaged total DNA $\bar{D}_{a,T} = \int_0^1 D_{a,T}(x)dx$. Applying our main result, the BCF's are given by

$$\theta_1^* = \int_0^1 \hat{v}_{P_a}^2(x)dx, \quad \theta_2^* = \int_0^1 \hat{v}_{P_r}^2(x)dx, \quad \theta_3^* = \hat{v}_{P_{a,2}}(x_a^*), \quad \theta_4^* = \hat{v}_{P_{a,2}}(x_r^*), \quad \theta_5^* = \hat{v}_{P_{r,2}}(x_a^*), \tag{26b}$$

where $\hat{v}_{P_a}(x)$, $\hat{v}_{P_r}(x)$, $\hat{v}_{P_{a,2}}(x)$, and $\hat{v}_{P_{r,2}}(x)$ are the normalized available volume profiles (i.e,. $\hat{v}_{P_a}(x) = v_{P_a}(x))/\int_0^1 v_{P_a}(x)dx)$ of $\mathrm{P_a}$, $\mathrm{P_r}$, $\mathrm{P_{a,2}}$, and $\mathrm{P_{r,2}}$, respectively. From (9), notice that $v_{P_{a,2}}(x) = v_{P_a}^2(x)$ and $v_{P_{r,2}}(x) = v_{P_r}^2(x)$. The available volume profiles are given by

$$v_{P_a}(x) = e^{-(r_a/r^*)^2 \hat{\rho}(x)}, \quad v_{P_r}(x) = e^{-(r_r/r^*)^2 \hat{\rho}(x)}, \tag{27}$$

where r_a and r_r are the radius of gyration of $\mathrm{P_a}$ and $\mathrm{P_r}$, respectively. Approximating $\bar{P}_{a,2}(t)$, $\bar{P}_{r,2}(t)$, $\bar{c}_{a,1}(t)$, $\bar{c}_{a,2}(t)$ and $\bar{c}_r(t)$ at their quasi-steady state (since $d_i \gg \gamma_a, \gamma_r$ for $i = 1, \ldots, 5$, [1]), we obtain

$$\bar{P}_{a,2}(t) = \frac{a_1\theta_1}{d_1}\bar{P}_a^2(t), \quad \bar{P}_{r,2}(t) = \frac{a_2\theta_2}{d_2}\bar{P}_r^2(t),$$

$$\bar{c}_{a,1}(t) = \frac{a_3\theta_3}{d_3}\bar{P}_{a,2}(t)\bar{D}_a(t), \quad \bar{c}_{a,2}(t) = \frac{a_4\theta_4}{d_4}\bar{P}_{a,2}(t)\bar{D}_r(t), \quad \bar{c}_r(t) = \frac{a_5\theta_5}{d_5}\bar{P}_{r,2}(t)\bar{D}_a(t),$$

and, therefore, we can further reduce (26) to

$$\frac{d\bar{P}_a}{dt} = \frac{\alpha_{0,A} + \alpha_A\left(\frac{\bar{P}_a}{K_{d,1}}\right)^2}{1 + \left(\frac{\bar{P}_a}{K_{d,1}}\right)^2 + \left(\frac{\bar{P}_r}{K_{d,2}}\right)^2} - \gamma_A \bar{P}_a, \quad \frac{d\bar{P}_r}{dt} = \frac{\alpha_{0,R} + \alpha_R\left(\frac{\bar{P}_a}{K_{d,3}}\right)^2}{1 + \left(\frac{\bar{P}_a}{K_{d,3}}\right)^2} - \gamma_R \bar{P}_r \tag{28a}$$

where $\alpha_{0,A} = \kappa_1 \bar{D}_{a,T}$ ($\alpha_{0,R} = \kappa_2 \bar{D}_{r,T}$) is the basal production rate of $\mathrm{P_a}$ ($\mathrm{P_r}$), $\alpha_A = \kappa_3$ ($\alpha_R = \kappa_4 \bar{D}_{r,T}$) is the additional production rate of $\mathrm{P_a}$ ($\mathrm{P_r}$) due to activation from $\mathrm{P_a}$, and

$$K_{d,1} = \frac{d_1 d_3}{\theta^*_{A,1} a_1 a_3}, \quad K_{d,2} = \frac{d_2 d_5}{\theta^*_R a_2 a_5}, \quad K_{d,3} = \frac{d_1 d_4}{\theta^*_{A,2} a_1 a_4}, \tag{28b}$$

$$\theta^*_{A,1} = \theta^*_1 \theta^*_3 = \hat{v}_{P_a}(x^*_a), \quad \theta^*_R = \theta^*_2 \theta^*_5 = \hat{v}_{P_r}(x^*_a), \quad \theta^*_{A,2} = \theta^*_1 \theta^*_4 = \hat{v}_{P_a}(x^*_r). \tag{28c}$$

The form of the dynamics given by (28) was theoretically analyzed in [36, 1], and it was shown that the values of $K_{d,i}$ for $i = 1, 2, 3$, were critical in determining whether sustained oscillations occur. From (28b), these parameters depend on (28c) and thus on the size of $\mathrm{P_a}$ and $\mathrm{P_r}$ through the available volume profiles (27) and the location of $\mathrm{D_a}$ and $\mathrm{D_r}$ (x^*_a and x^*_r). Numerical simulations demonstrate how these spatial parameters affect circuit behavior. In our simulation setup, the parameters are chosen such that the well-mixed model ((26) with $\theta^*_R = \theta^*_{A,1} = \theta^*_{A,2} = 1$) oscillates, the DNA of $\mathrm{P_a}$ and $\mathrm{P_r}$ are localized at the cell poles and have the same copy number (i.e., $x^*_a = x^*_r$ and $\bar{D}_{r,T} = \bar{D}_{a,T} = 1$), the size of $\mathrm{P_r}$ is chosen to be small $r_r/r^* \ll 1$ (thus $\theta^*_R \approx 1$), and the size of $\mathrm{P_a}$ is varied (thus varying $\theta^*_{A,1}$ and $\theta^*_{A,2}$). Since $\mathrm{D_a}$ is localized at the cell poles, it implies $x^*_a \approx 1$ and from (28c), we observe that if $r_a/r^* \ll 1 \implies \theta^*_{A,1} \approx \theta^*_{A,2} \approx 1$ and $\theta^*_{A,1}, \theta^*_{A,2}$ increase as r_a/r^* increases. The results of these simulations are shown in Figure 7. When $r_a/r^* \ll 1$, the full PDE model ((72) in SI Section 2.9), the reduced ODE model (26), and the well-mixed model are all in agreement and sustained oscillations are observed. By contrast, when $r_a/r^* = 1$, the PDE and reduced model (which are in agreement with each other as explicitly shown in SI Figure 21) predict that sustained oscillations will no longer occur. Furthermore, in SI Section 2.9 we demonstrate in Figure 22 that indeed as the size of $\mathrm{P_a}$ increases it is excluded from the chromosome onto the cell poles while the spatial profile of $\mathrm{P_r}$ is homogeneously distributed throughout the cell since $r_r/r^* \ll 1$ (Remark 1).

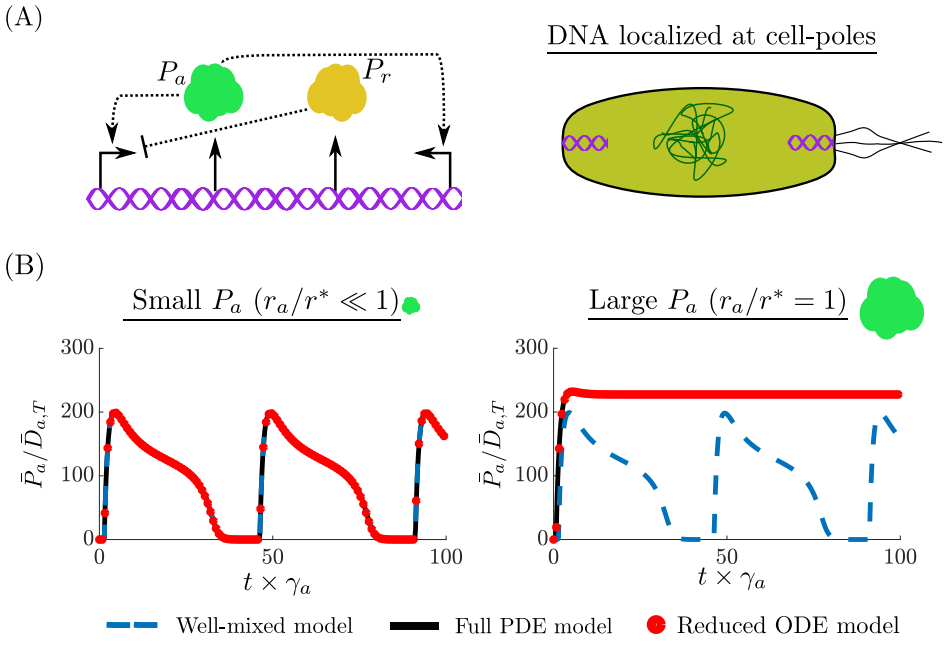

Figure 7: **Spatial effects on the dynamics of genetic circuits**. (A) The activator-repressor clock where $\mathrm{P_r}$ represses $\mathrm{P_a}$ and $\mathrm{P_a}$ activates itself and $\mathrm{P_r}$. Both proteins are expressed from the same cell-pole localized plasmid. (B) The temporal evolution of $\mathrm{P_a}$ is given for the full-PDE model ((72) in SI Section 2.9), the reduced ODE model (26), and the well-mixed model (same as (26) with $\theta^*_{A,1} = \theta^*_{A,2} = \theta^*_R = 1$). When $\mathrm{P_a}$ is small ($r_a/r^* \ll 1$), all three models predict sustained oscillations. When $\mathrm{P_a}$ is large ($r_a/r^* = 1$), the full-PDE model and the reduced ODE model predict the oscillations will cease. For both simulations $r_r/r^* \ll 1 \implies \theta^*_R \approx 1$. The full simulation details and parameter values are given in SI Section 2.9.

Discussion

We derived a reduced order ODE model of genetic circuits with the same dimension as traditional ODE well-mixed models; yet, it captures effects of spatial heterogeneity within bacterial cells (11). In particular, our reduced model is the same as a well-mixed model where all the association rate constants are multiplied by the binding correction factor (BCF). This factor depends on the size and location (if fixed in space) of the reacting species, according to an analytical formula that we derived from first principles (11b) and its value can be estimated experimentally through simple procedures (SI Section 2.11). We have mathematically demonstrated that this reduced order model is a good approximation of the space-averaged dynamics resulting from a reaction-diffusion PDE model under the assumption of fast diffusion. It can therefore be used in place of PDE models, providing substantial advantages for both simulation and mathematical analysis.

We applied this model to analyze the effects of spatial heterogeneity on core biological processes and genetic circuits. Specifically, motivated by the fact that DNA, ribosomes, and mRNA have been shown to localize within the cell [4, 14, 5], we analyzed the transcription and translation processes. We determined that mRNA levels are lower (higher) when the gene is localized near the mid-cell (cell poles). We also showed that when the target gene of a transcriptional repressor is near mid-cell (cell poles) the effective repression is lower (higher) with respect to that of the well-mixed model. This discrepancy is amplified as the size of the transcription factor increases. The extent of these spatial effects depends on how different the value of the BCF is from unity. Based on parameters found in the literature, we determined that for the processes of transcription and its regulation the BCF should be close to unity and hence a well-mixed ODE model should be sufficient. However, in situations where the nucleoid is highly compacted (from overexpressing mRNA [13] or translational inhibition [37]), we expect that the available volume profile (2) approaches small values and, as a consequence, the value of the BCF can substantially deviate from unity (11b).

Our results provide additional interpretations of well-known biological phenomena. For example, it has been shown that the expression rate of chromosomal genes depends on the locus where the gene is inserted [38]; that the nucleoid dynamically changes shape to control gene expression and transcription regulation [4, 39] (e.g., see SI Section 2.13 for how a time varying chromosome density modulates the BCF); and that coregulation and coexpression among genes depends on their spatial distance [40]. For a fixed amount of mRNA, we showed that spatial heterogeneity leads to higher translation rates since both mRNA and ribosome are pushed out of the chromosome into a smaller region near the cell poles, which results in larger effective binding affinity. How larger, it depends on the value of the BCF. For a polysome with 10 translating ribosomes, the value of the BCF can deviate from unity by 56% in the ribosome loading step and by 7% in the peptide release step. These estimates are believed to be conservative since we did not account for the exclusion effects from the peptide chains attached to the translating ribosome, which will result in even more pronounced spatial effects. Therefore, a well-mixed model may not be sufficient to capture the effects of spatial heterogeneity on translation.

Our modeling framework can be easily extended to other aspects of gene expression. For example, we may consider co-transcriptional translation [41]. In this case, as a result of translation being localized at the gene location, the effective ribosome binding site strength will also depend on gene location through the BCF. We may also consider the role of spatial heterogeneity on orthogonal translational machinery [42]. From our models, we predict that one can tune the rate at which orthogonal ribosomes are formed by creating larger synthetic 16S rRNA. Furthermore, once the production of orthogonal ribosomes is placed in a feedback form to decouple genetic circuits [42], our framework suggests that the feedback efficiency may depend on the spatial location of the synthetic 16S rRNA gene. The value of the parameter r^*, whose squared value is inversely proportional to the average chromosome density (2), is critical in determining the extent of spatial effects. In this study we indirectly estimated a value of r^* based on [13]. However, a more comprehensive study should be conducted to estimate r^* for several contexts (SI Section 2.11), or equivalently to estimate extent of excluded volume effects, which may easily be performed via superresolution imaging [14].

In summary, this paper provides a general and convenient modeling framework to account for DNA localization and excluded volume effects on intracellular species dynamics. While other phenomena contributing to intracellular spatial heterogeneity, such as crowding [43], sliding, hopping, and dimensionality [17], exist, this is a first step towards creating a general framework to modify current models to capture spatial information. Our model can be used both as an analysis and a design tool for genetic circuits, in which variables such as gene location and regulator size may be considered as additional design parameters.

Author Contributions

C.B. performed the research, developed the mathematical analysis, and wrote the article. D.D.V. designed the research, assisted with the mathematical analysis, and edited the article.

Acknowledgments

This work was supported in part by NSF Expeditions, Grant Number 1521925, AFOSR grant FA9550-14-1-0060, the NSF Graduate Research Fellowships Program, and the Ford Foundation Predoctoral Fellowship. We thank Jean-Jacques Slotine for the technical discussions on contraction theory. We thank Theodore Grunberg and Yili Qian for reviewing the article and helpful discussions

References

[1] D. Del Vecchio and R. M. Murray, *Biomolecular Feedback Systems*. 2014.

[2] U. Alon, "An Introduction to Systems Biology: Design Principles of Biological Circuits," 2007.

[3] N. S. Wingreen and K. C. Huang, "Physics of Intracellular Organization in Bacteria," *Annual Review of Microbiology*, vol. 69, no. 1, pp. 361–379, 2015.

[4] X. Weng and J. Xiao, "Spatial organization of transcription in bacterial cells," *Trends in Genetics*, vol. 30, no. 7, pp. 287–297, 2014.

[5] L. A. van Gijtenbeek, A. Robinson, A. M. van Oijen, B. Poolman, and J. Kok, "On the Spatial Organization of mRNA, Plasmids, and Ribosomes in a Bacterial Host Overexpressing Membrane Proteins," *PLoS Genetics*, vol. 12, no. 12, pp. 1–28, 2016.

[6] S. Saberi and E. Emberly, "Non-Equilibrium Polar Localization of Proteins in Bacterial Cells," *PLoS ONE*, vol. 8, no. 5, pp. 1–9, 2013.

[7] C. A. Brackley, S. Taylor, A. Papantonis, P. R. Cook, and D. Marenduzzo, "Nonspecific bridging-induced attraction drives clustering of DNA-binding proteins and genome organization," *Proceedings of the National Academy of Sciences*, vol. 110, no. 38, pp. E3605–E3611, 2013.

[8] C. K. Macnamara and M. A. J. Chaplain, "Spatio-temporal models of synthetic genetic oscillators," *Mathematical Biosciences and Engineering*, vol. 14, no. 1, pp. 249–262, 2016.

[9] S. Yao, D. R. Helinski, and A. Toukdarian, "Localization of the naturally occurring plasmid ColE1 at the cell pole," *Journal of Bacteriology*, vol. 189, no. 5, pp. 1946–1953, 2007.

[10] G. Ebersbach and K. Gerdes, "Plasmid Segregation Mechanisms," *Annual Review of Genetics*, vol. 39, no. 1, pp. 453–479, 2005.

[11] Y. Wang, P. Penkul, and J. N. Milstein, "Quantitative Localization Microscopy Reveals a Novel Organization of a High-Copy Number Plasmid," *Biophysical Journal*, vol. 111, no. 3, pp. 467–479, 2016.

[12] J. A. Englaender, J. A. Jones, B. F. Cress, T. E. Kuhlman, R. J. Linhardt, and M. A. Koffas, "Effect of Genomic Integration Location on Heterologous Protein Expression and Metabolic Engineering in E. coli," *ACS Synthetic Biology*, vol. 6, no. 4, pp. 710–720, 2017.

[13] M. Castellana, S. Hsin-Jung Li, and N. S. Wingreen, "Spatial organization of bacterial transcription and translation," *Proceedings of the National Academy of Sciences*, vol. 113, no. 33, pp. 9286–9291, 2016.

[14] S. Bakshi, A. Siryaporn, M. Goulian, and J. C. Weisshaar, "Superresolution imaging of ribosomes and RNA polymerase in live Escherichia coli cells," *Molecular Microbiology*, vol. 85, no. 1, pp. 21–38, 2012.

[15] R. Stoof, A. Wood, and A. Goni-Moreno, "A model for the spatio-temporal design of gene regulatory circuits," *bioRxiv*, p. 522946, 2019.

[16] J. Halatek and E. Frey, "Rethinking pattern formation in reaction-diffusion systems," *Nature Physics*, vol. 14, no. 5, pp. 507–514, 2018.

[17] S. Soh, M. Byrska, K. Kandere-Grzybowska, and B. A. Grzybowski, "Reaction-diffusion systems in intracellular molecular transport and control," *Angewandte Chemie - International Edition*, vol. 49, no. 25, pp. 4170–4198, 2010.

[18] H. de Jong, "Modeling and Simulation of Genetic Regulatory Systems: A Literature Review," *Journal of Computational Biology*, vol. 9, no. 1, pp. 67–103, 2002.

[19] C. Barajas and D. D. Vecchio, "Genetic Circuit-Host Ribosome Transactions : Diffusion-Reaction Model," *Acc*, pp. 1533–1540, 2019.

[20] H. Teimouri, E. Korkmazhan, J. Stavans, and E. Levine, "Sub-cellular mRNA localization modulates the regulation of gene expression by small RNAs in bacteria," *Physical Biology*, vol. 14, no. 5, 2017.

[21] A. Amir and S. van Teeffelen, "Getting into shape: How do rod-like bacteria control their geometry?," *Systems and Synthetic Biology*, vol. 8, no. 3, pp. 227–235, 2014.

[22] Leah Edelstein-Keshet, "Mathematical Models in Biology," *Siam*, vol. XXXIII, no. 2, pp. 81–87, 2012.

[23] D. Mishra, P. M. Rivera, A. Lin, D. Del Vecchio, and R. Weiss, "A load driver device for engineering modularity in biological networks," *Nature Biotechnology*, vol. 32, no. 12, pp. 1268–1275, 2014.

[24] S. H. Cho, J. M. Godin, C.-H. Chen, W. Qiao, H. Lee, and Y.-H. Lo, "Review Article: Recent advancements in optofluidic flow cytometer," *Biomicrofluidics*, vol. 4, p. 043001, dec 2010.

[25] W. Chen, M. Niepel, and P. Sorger, "Classic and contemporary approaches to modeling biochemical reactions," *Genes & Development*, vol. 24, pp. 1861–1875, 2010.

[26] C. Grossmann, H.-G. Roos, and M. Stynes, *Numerical Treatment of Partial Differential Equations*. 2007.

[27] G. Strang, *Computational science and engineering*. Wellesley-Cambridge Press Wellesley, 2007.

[28] O. Meisenberger, I. Pilz, and H. Heumann, "Small-angle x-ray study of DNA-dependent RNA polymerase subunit $\alpha 2$ from Escherichia coli," *FEBS Letters*, vol. 120, no. 1, pp. 57–60, 1980.

[29] I. Andreeva, R. Belardinelli, and M. V. Rodnina, "Translation initiation in bacterial polysomes through ribosome loading on a standby site on a highly translated mRNA," *Proceedings of the National Academy of Sciences of the United States of America*, vol. 115, no. 17, pp. 4411–4416, 2018.

[30] F. W. Ruscetti and L. A. Jacobson, "Accumulation of 70S monoribosomes in Escherichia coli after energy source shift-down.," *Journal of Bacteriology*, vol. 111, no. 1, pp. 142–151, 1972.

[31] P. P. Dennis and H. Bremer, "Modulation of Chemical Composition and Other Parameters of the Cell at Different Exponential Growth Rates," *EcoSal Plus*, vol. 3, no. 1, 2008.

[32] J. L. Ramos, M. Mart, A. J. Molina-henares, W. Tera, R. Brennan, and R. Tobes, "TetR family of transcriptional," vol. 69, no. 2, pp. 1–31, 2005.

[33] M. H. Larson, L. A. Gilbert, X. Wang, W. A. Lim, J. S. Weissman, and L. S. Qi, "CRISPR interference (CRISPRi) for sequence-specific control of gene expression," *Nature Protocols*, vol. 8, no. 11, pp. 2180–2196, 2013.

[34] G. J. Gibson and M. Yang, "What rheumatologists need to know about CRISPR/Cas9," *Nature Reviews Rheumatology*, vol. 13, no. 4, pp. 205–216, 2017.

[35] M. R. Atkinson, M. A. Savageau, J. T. Myers, and A. J. Ninfa, "Development of genetic circuitry exhibiting toggle switch or oscillatory behavior in Escherichia coli," *Cell*, vol. 113, no. 5, pp. 597–607, 2003.

[36] D. Del Vecchio, "Design and analysis of an activator-repressor clock in E. Coli," in *Proceedings of the American Control Conference*, pp. 1589–1594, 2007.

[37] A. Sanamrad, F. Persson, E. G. Lundius, D. Fange, A. H. Gynna, and J. Elf, "Single-particle tracking reveals that free ribosomal subunits are not excluded from the Escherichia coli nucleoid," *Proceedings of the National Academy of Sciences*, vol. 111, no. 31, pp. 11413–11418, 2014.

[38] M.-A. Sánchez-Romero, D. Lee, E. Sánchez-Morán, and S. Busby, " Location and dynamics of an active promoter in Escherichia coli K-12 ," *Biochemical Journal*, vol. 441, no. 1, pp. 481–485, 2012.

[39] J. K. Fisher, A. Bourniquel, G. Witz, B. Weiner, M. Prentiss, and N. Kleckner, "Four-dimensional imaging of E. coli nucleoid organization and dynamics in living cells," *Cell*, vol. 153, no. 4, pp. 882–895, 2013.

[40] L. Pannier, E. Merino, K. Marchal, and J. Collado-Vides, "Effect of genomic distance on coexpression of coregulated genes in E. coli," *PLoS ONE*, vol. 12, no. 4, pp. 1–20, 2017.

[41] S. Bakshi, H. Choi, and J. C. Weisshaar, "The spatial biology of transcription and translation in rapidly growing Escherichia coli," *Frontiers in Microbiology*, vol. 6, no. JUL, pp. 1–15, 2015.

[42] A. P. Darlington, J. Kim, J. I. Jiménez, and D. G. Bates, "Dynamic allocation of orthogonal ribosomes facilitates uncoupling of co-expressed genes," *Nature Communications*, vol. 9, no. 1, 2018.

[43] M. Tabaka, T. Kalwarczyk, J. Szymanski, S. Hou, and R. Holyst, "The effect of macromolecular crowding on mobility of biomolecules, association kinetics, and gene expression in living cells," *Frontiers in Physics*, vol. 2, no. September, pp. 1–14, 2014.

[44] M. Renardy and R. C. Rogers, "An Introduction to Partial Differential Equations," *Differential Equations*, vol. 13, no. 2, pp. 1–5, 2003.

[45] W. Lohmiller and J. J. E. Slotine, "On Contraction Analysis for Non-linear Systems," *Automatica*, vol. 34, no. 6, pp. 683–696, 1998.

[46] G. Russo and J. J. E. Slotine, "Symmetries, stability, and control in nonlinear systems and networks," *Physical Review E - Statistical, Nonlinear, and Soft Matter Physics*, vol. 84, no. 4, 2011.

[47] D. Del Vecchio and J. J. E. Slotine, "A contraction theory approach to singularly perturbed systems," *IEEE Transactions on Automatic Control*, vol. 58, no. 3, pp. 752–757, 2013.

[48] E. I., J. M. Ortega, and W. C. Rheinboldt, "Iterative Solution of Nonlinear Equations in Several Variables," *Mathematics of Computation*, vol. 25, no. 114, p. 398, 1971.

[49] R. A. Horn and C. R. Johnson, *Matrix Analysis*. Cambridge: Cambridge University Press, 2012.

[50] H. Weinberger, "Invariant sets for weakly coupled parabolic and elliptic systems," *Rend. Mat. Univ. Roma*, vol. 8, no. l, pp. 295–310, 1975.

[51] W. F. Trench, *Trench_Real_Analysis*. 2010.

[52] A. Gyorgy, J. I. Jiménez, J. Yazbek, H. H. Huang, H. Chung, R. Weiss, and D. Del Vecchio, "Isocost Lines Describe the Cellular Economy of Genetic Circuits," *Biophysical Journal*, vol. 109, no. 3, pp. 639–646, 2015.

[53] B. P. Bratton, R. A. Mooney, and J. C. Weisshaar, "Spatial distribution and diffusive motion of rna polymerase in live Escherichia coli," *Journal of Bacteriology*, vol. 193, no. 19, pp. 5138–5146, 2011.

[54] T. E. Kuhlman and E. C. Cox, "Gene location and DNA density determine transcription factor distributions in Escherichia coli," *Molecular Systems Biology*, vol. 8, no. 610, pp. 1–13, 2012.

[55] H. Lederer, K. Tovar, G. Baer, R. P. May, W. Hillen, and H. Heumann, "The quaternary structure of Tet repressors bound to the Tn10-encoded tet gene control region determined by neutron solution scattering.," *The EMBO Journal*, vol. 8, no. 4, pp. 1257–1263, 1989.

[56] I. Pilz, K. Goral, O. Kratky, N. G. Wade-Jardetzky, O. Jardetzky, and R. P. Bray, "Small-Angle X-Ray Studies of the Quaternary Structure of the Lac Repressor from Escherichia Coli," *Biochemistry*, vol. 19, no. 17, pp. 4087–4090, 1980.

[57] L. B. Harrington, K. W. Doxzen, E. Ma, J. J. Liu, G. J. Knott, A. Edraki, B. Garcia, N. Amrani, J. S. Chen, J. C. Cofsky, P. J. Kranzusch, E. J. Sontheimer, A. R. Davidson, K. L. Maxwell, and J. A. Doudna, "A Broad-Spectrum Inhibitor of CRISPR-Cas9," *Cell*, vol. 170, no. 6, pp. 1224–1233.e15, 2017.

[58] S. Tabor, "Expression Using the T7 RNA Polymerase/Promoter System," *Current Protocols in Molecular Biology*, 2004.

[59] E. Knobloch and R. Krechetnikov, "Problems on time-varying domains: Formulation, dynamics, and challenges," *Acta Applicandae Mathematicae*, vol. 137, no. 1, pp. 123–157, 2015.

[60] K. Hayashi, N. Morooka, Y. Yamamoto, K. Fujita, K. Isono, S. Choi, E. Ohtsubo, T. Baba, B. L. Wanner, H. Mori, and T. Horiuchi, "Highly accurate genome sequences of Escherichia coli K-12 strains MG1655 and W3110," *Molecular Systems Biology*, 2006.

Supplementary Material

2 Time Scale Separation Proofs

2.1 Preliminaries:

Notation: Let $\boldsymbol{z} = [z_1, \ldots, z_n]^T \in \mathbb{R}^n$ (where superscript T denotes the transpose operation) and the j-th component of $\boldsymbol{z}$ is denoted by $\boldsymbol{z}^j$. A vector of zeros is denoted as $\boldsymbol{0}_n = [0, \ldots, 0]^T \in \mathbb{R}^n$ and we use $\boldsymbol{A} = \text{diag}(\boldsymbol{v}) \in \mathbb{R}^{n\times n}$ to refer to a square matrix with all zeros in the off-diagonals and diagonal elements specified by the vector $\boldsymbol{v}$. The (j,k)-th element of matrix $\boldsymbol{A}$ is denoted by $\boldsymbol{A}^{j,k}$ and $\boldsymbol{I}_{n,n}$ is the identity matrix acting on $\mathbb{R}^n$. Let $\mathbb{R}^n_+ = \{[z_1, \ldots, z_n]^T : z_i > 0, i = 1, \ldots, n\}$ denote the positive orthant of $\mathbb{R}^n$. For a Hilbert space H with inner product $\langle \cdot, \cdot \rangle_H$, we denote the norm as $|| \cdot ||_H = \sqrt{\langle \cdot, \cdot \rangle_H}$. Finally, let overbars denote spatial integration $\bar{u} := \int_0^1 u(x)dx$.

Definition 1. (Linear Differential Operator) Let $v(x) : [0,1] \to \mathbb{R}_+$ be a smooth function, and consider the following linear differential operator:

$$\mathcal{L}_v(y) := \frac{d}{dx}\left[v^2(x)\frac{d}{dx}\left[\frac{y(x)}{v(x)}\right]\right], \tag{29}$$

with domain $D(\mathcal{L}_v) = \{y \in L^2(0,1) : v^2 \frac{d}{dx}\left[\frac{y}{v}\right]\big|_{x=0,1} = 0\}$:

Next, we introduce the Hilbert space $L^2_v(0,1)$ that we use for our analysis. This space is isomorphic to $L^2(0,1)$ however, the operator (29) is self-adjoint with respect to the inner product in $L^2_v(0,1)$.

Definition 2. (Weighted $L^2(0,1)$ space) For smooth $v : [0,1] \to \mathbb{R}_+$ we denote $L^2_v(0,1)$ as a weighted space of the square integrable functions such that $f \in L^2_v(0,1)$ if and only if $: \frac{f}{\sqrt{v(x)}} \in L^2(0,1)$. The inner-product is defined as $\langle f, g\rangle_v := \int_0^1 \frac{f(x)g(x)}{\hat{v}}dx$, for $f, g \in L^2_v(0,1)$ and $\hat{v}(x) = \frac{v(x)}{\bar{v}}$. Furthermore, let $\boldsymbol{v} = [v_1(x), \ldots, v_n(x)]^T$, where $v_i(x) : [0,1] \to \mathbb{R}_+$ is smooth, then $\boldsymbol{z} \in L^2_{\boldsymbol{v}}((0,1), \mathbb{R}^n)$ if $\boldsymbol{z}^i \in L^2_{v_i}(0,1)$ for $i = 1, \ldots, n$, and the inner product in this space is defined as $\langle \boldsymbol{f}, \boldsymbol{g}\rangle_{\boldsymbol{v}} := \int_0^1 \boldsymbol{f}^T(x)[\text{diag}(\hat{\boldsymbol{v}})]^{-1}\boldsymbol{g}(x)dx$, for $\boldsymbol{f}, \boldsymbol{g} \in L^2_{\boldsymbol{v}}((0,1), \mathbb{R}^n)$, where $\hat{\boldsymbol{v}}^i(x) = \frac{\boldsymbol{v}^i(x)}{\bar{\hat{\boldsymbol{v}}}^i}$.

Remark 3. (Norm equivalence between L^2 and L^2_v) For smooth $v : [0,1] \to \mathbb{R}_+$, let $\hat{v}(x) = v(x)/\bar{v}$, $\hat{v}_* = \min_{x\in[0,1]} \hat{v}(x)$ and $\hat{v}^* = \max_{x\in[0,1]} \hat{v}(x)$, the norms defined on $L^2_v(0,1)$ and $L^2(0,1)$ are related by

$$\frac{1}{\sqrt{\hat{v}^*}}||y||_{L^2} \leq ||y||_{L^2_v} \leq \frac{1}{\sqrt{\hat{v}_*}}||y||_{L^2},$$

for any $y \in L^2_v(0,1)$. Thus, when performing convergence analysis we may use the norms defined in $L^2_v(0,1)$ and $L^2(0,1)$ interchangeably.

Lemma 1. *(Negative semi-definite and self-adjoint Operator) For smooth $v : [0,1] \to \mathbb{R}_+$, let $\mathcal{L}_v$ be as in Definition 1. This operator has the following properties:*

I Has countably many, real, and distinct eigenvalues such that $\lambda_1 > \ldots > \lambda_n > \ldots$ *and* $\lim_{n\to\infty} \lambda_n = -\infty$

II The set of corresponding eigenfunctions $\{\psi_i(x)\}$ *form a complete orthonormal basis for* $L^2_v(0,1)$ *(Definition 2)*

III $\lambda_1 = 0$ *and* $\psi_1 = \hat{v}(x) = \frac{v(x)}{\bar{v}}$

Proof: The proof of (I) and (II) follow from Sturm-Liouville theory [44]. To prove (III), we take the weighted inner product of both side of $\mathcal{L}_v\psi_i = \lambda_i\psi_i$ with ψ_i, we use orthonormality, use integration by parts, and apply the boundary conditions:

$$\begin{aligned}\lambda_i &= \langle \psi_i, \mathcal{L}_v(\psi_i)\rangle_v \\ &= \int_0^1 \frac{\psi_i}{\hat{v}}\frac{d}{dx}\left(v^2\frac{d}{dx}\left(\frac{\psi_i}{v}\right)\right)dx \\ &= \cancelto{0}{\left[\frac{\psi_i}{\hat{v}}v^2\frac{d}{dx}\left(\frac{\psi_i}{v}\right)\right]_{x=0,1}} - \int_0^1 \bar{v}\left(v\frac{d}{dx}\left(\frac{\psi_i}{v}\right)\right)^2 dx \\ &\leq 0.\end{aligned} \tag{30}$$

The maximum of (30) is achieved ($\lambda_1 = 0$) for $\psi_1 = \hat{v}(x)$, since substituting $\hat{v}(x)$ directly into $\mathcal{L}_v$, one observes that $\mathcal{L}_v(\hat{v}(x)) = 0$ and we have that $||\psi_1||_{L^2_v} = \sqrt{\langle\psi_1,\psi_1\rangle_v} = 1$, therefore $\lambda_i < 0, \forall i > 1$. ■

The following will introduce the notion of contracting dynamical systems. A dynamical system is said to be contracting within an open and connected subspace of the state space, if all trajectories starting within this region converge exponentially to each other. We provide sufficient conditions to guarantee that a dynamical system is contracting, and finally show that contracting systems have a particular robustness property. The robustness property will be exploited several times in our analysis to perform our model reduction.

Theorem 1. *Let* $\dot{\boldsymbol{z}} = \boldsymbol{f}(t,\boldsymbol{z})$ *be a dynamical system in the Hilbert space* $H = \mathbb{R}^n$ *where* $\boldsymbol{f}$ *is a smooth nonlinear function. A dynamical system is said to be contracting within an open and connected subspace of the state space* $\chi \subseteq H$*, if all trajectories starting within this region converge exponentially to each other. A sufficient condition for a system to be contracting in* H *is the existence a uniformly positive definite matrix* $\boldsymbol{P}(t,\boldsymbol{z}) \in \mathbb{R}^{n\times n}$ *and constant* $\lambda > 0$ *such that*

$$\frac{1}{2}\left[\frac{\partial \boldsymbol{f}}{\partial \boldsymbol{z}}^T\boldsymbol{P} + \boldsymbol{P}\frac{\partial \boldsymbol{f}}{\partial \boldsymbol{z}} + \dot{\boldsymbol{P}}\right] \leq -\xi\boldsymbol{P}, \forall \boldsymbol{z} \in \chi, \forall t \geq 0 \tag{31}$$

where ξ *is the contraction rate of the system and* $\dot{\boldsymbol{P}}$ *is the total time derivative of* $\boldsymbol{P}$*.*

Proof: See Theorem 2 in [45]. ■

Lemma 2. *(Hierarchies of contracting systems) Let*

$$\frac{d\boldsymbol{z}(t)}{dt} = \frac{d}{dt}\begin{bmatrix}\boldsymbol{z}_1(t)\\ \boldsymbol{z}_2(t)\end{bmatrix} = \begin{bmatrix}\boldsymbol{f}_1(t,\boldsymbol{z}_1)\\ \boldsymbol{f}_2(t,\boldsymbol{z}_1,\boldsymbol{z}_2)\end{bmatrix} \tag{32}$$

be dynamical systems in the Hilbert space $H = \mathbb{R}^{n+m}$ *where* $\boldsymbol{f}_1 : [0,\infty)\times\mathbb{R}^n \to \mathbb{R}^n$ *and* $\boldsymbol{f}_2 : [0,\infty)\times\mathbb{R}^n\times\mathbb{R}^m \to \mathbb{R}^m$ *are smooth nonlinear functions. Then, sufficient conditions for (32) to be contracting in* $\chi = \chi_1 \oplus \chi_2$*, where* χ_1 *and* χ_2 *are open connected subspaces of* $\mathbb{R}^n$ *and* $\mathbb{R}^m$*, respectively, are*

I $\frac{\partial \boldsymbol{f}_1}{\partial \boldsymbol{z}_1}$ *satisfies (31) in* χ_1 *for some* $\boldsymbol{P}_1 \in \mathbb{R}^{n\times n}$ *such that* $\boldsymbol{P}_1 = \boldsymbol{P}_1^T > 0$

II $\frac{\partial \boldsymbol{f}_2}{\partial \boldsymbol{z}_2}$ *satisfies (31) in* χ_2 *for some* $\boldsymbol{P}_2 \in \mathbb{R}^{m\times m}$ *such that* $\boldsymbol{P}_2 = \boldsymbol{P}_2^T > 0$

III $\frac{\partial \boldsymbol{f}_2}{\partial \boldsymbol{z}_1}$ *is uniformly bounded for all* $t \geq 0$*,* $\boldsymbol{z}_1 \in \chi_1$*, and* $\boldsymbol{z}_2 \in \chi_2$

Proof: See hierarchal structures in [45] and applied in [46] ■

Lemma 3. *(Robustness property of contracting systems) Assume that* $\dot{\boldsymbol{z}} = \boldsymbol{f}(t,\boldsymbol{z})$ *satisfies the conditions of Theorem 1, for some* $\boldsymbol{P}(t,\boldsymbol{z}) = \boldsymbol{P}(t,\boldsymbol{z})^T > 0$ *in a region* $\chi \subseteq H$*, and thus it is contracting with some contraction rate* ξ*. Furthermore, assume that there exists a positive constant* λ^* *(* λ_**) that upper (lower)*

bounds the maximum (minimum) eigenvalue of $\boldsymbol{P}$ for all $t \geq 0$. Consider the "perturbed" system $\dot{\boldsymbol{z}}_{\boldsymbol{p}} = \boldsymbol{f}(t, \boldsymbol{z}_p) + \boldsymbol{d}(t, \boldsymbol{z}_p)$, and suppose there exists $L_1, L_2, \zeta, \epsilon > 0$ such that $\zeta/\epsilon > \xi$ and $||\boldsymbol{d}(t, \boldsymbol{z}_p)||_H \leq L_1 e^{-\zeta/\epsilon t} + L_2\epsilon$ for all $t \geq 0$ and $\boldsymbol{z}_p \in \chi$. Then, there exists $L^*, \epsilon^* > 0$ such that for all $\boldsymbol{z}(0), \boldsymbol{z}_p(0) \in \chi$ and $0 < \epsilon < \epsilon^*$, the solutions $\boldsymbol{z}_p(t)$ and $\boldsymbol{z}(t)$ satisfy

$$||\boldsymbol{z}_p(t) - \boldsymbol{z}(t)||_H \leq \sqrt{\frac{\lambda^*}{\lambda_*}}\Big(||\boldsymbol{z}_p(0) - \boldsymbol{z}(0)||_H e^{-\xi t} + L^*\epsilon\Big), \quad \forall t \geq 0.$$

Proof: This follows from the result of Seciton 3.7 Result vii in [45]. Let $R_z(0)$ be the length of the straight path connecting $\boldsymbol{z}_p(0)$ and $\boldsymbol{z}(0)$, that is, $R_z(0) = \int_{\boldsymbol{z}(0)}^{\boldsymbol{z}_p(0)} ||\delta z(0)||_H = ||\boldsymbol{z}_p(0) - \boldsymbol{z}(0)||_H$, where δz is the virtual displacement (see [45] for details. Each point in the straight path connecting $\boldsymbol{z}_p(0)$ and $\boldsymbol{z}(0)$ evolves in time and we denote the length of the path connecting these points be given by $R_z(t)$. Precisely, $R_z(t) = \int_{\boldsymbol{z}}^{\boldsymbol{z}_p} ||\delta z(t)||_H$. Notice that

$$||\boldsymbol{z}_p(t) - \boldsymbol{z}(t)||_H \leq R_z(t), \tag{33}$$

since the straight line path is the shortest path between the trajectories (they would be equal if the initial straight line segment remained a line for all time, but this is only the case for constant vector fields). Let $R(t) = \int_{\boldsymbol{z}}^{\boldsymbol{z}_p} ||P^{1/2}\delta z||_H$. Notice that

$$\sqrt{\lambda_*} R_z(t) \leq R(t) \leq \sqrt{\lambda^*} R_z(t). \tag{34}$$

From Equation 15 in [45], we have that $\dot{R} + \xi R \leq ||\boldsymbol{P}^{1/2} d||_H$ and thus

$$R(t) \leq R(0)e^{-\xi t} + \sqrt{\lambda^*}\int_0^t ||\boldsymbol{d}(\tau)||_H e^{-\xi(t-\tau)d\tau}.$$

From (34), we have that

$$\sqrt{\lambda_*} R_z(t) \leq \sqrt{\lambda^*} R_z(0)e^{-\xi t} + \sqrt{\lambda^*}\int_0^t ||\boldsymbol{d}(\tau)||_H e^{-\xi(t-\tau)d\tau}.$$

Finally, by (33), this implies that

$$\begin{aligned} ||\boldsymbol{z}_p(t) - \boldsymbol{z}(t)||_H &\leq \sqrt{\frac{\lambda^*}{\lambda_*}}\Big(||\boldsymbol{z}_p(0) - \boldsymbol{z}(0)||_H e^{-\xi t} + \int_0^t L_1 e^{-(\zeta/\epsilon)\tau} e^{-\xi(t-\tau)} d\tau + \frac{L_2\epsilon}{\xi}\Big) \\ &\leq \sqrt{\frac{\lambda^*}{\lambda_*}}\Big(||\boldsymbol{z}_p(0) - \boldsymbol{z}(0)||_H e^{-\xi t} + \frac{L_1}{\zeta}\frac{\epsilon}{1 - \epsilon\xi/\zeta} + \frac{L_2\epsilon}{\xi}\Big). \end{aligned}$$

The desired result holds for $\epsilon^* = \zeta/(2\xi)$ and $L^* = 2L_1/\zeta + L_2/\xi$. ■

2.2 Solutions of diffusing states converge to the null space of the differential operator $\boldsymbol{\mathcal{L}_v}$

Let $\boldsymbol{v} : [0,1] \to \mathbb{R}_+^{n_d}$ be a smooth vector-valued function and $\boldsymbol{V}(x) = \text{diag}(\boldsymbol{v}(x))$. For the state vectors $\boldsymbol{z}_s(t,x) \in H_s := L^2((0,1), \mathbb{R}^{n_s}), \forall t \geq 0$ and $\boldsymbol{z}_d(t,x) \in H_d := L^2_{\boldsymbol{v}}((0,1), \mathbb{R}^{n_d}), \forall t \geq 0$, consider the following reaction-diffusion system:

$$\begin{aligned} &\frac{\partial \boldsymbol{z}_s(t,x)}{\partial t} = \boldsymbol{f}_s(t, x, \boldsymbol{z}_s, \boldsymbol{z}_d), \quad t \geq 0, x \in [0,1], \\ &\frac{\partial \boldsymbol{z}_d(t,x)}{\partial t} = \frac{1}{\epsilon}\boldsymbol{D}\boldsymbol{\mathcal{L}_v}(\boldsymbol{z}_d) + \boldsymbol{f}_d(t, x, \boldsymbol{z}_s, \boldsymbol{z}_d), \quad t \geq 0, x \in (0,1), \\ &\boldsymbol{V}^2(x)\frac{d}{dx}\big[\boldsymbol{V}^{-1}(x)\boldsymbol{z}_d(t,x)\big]\Big|_{x=0,1} = \boldsymbol{0}_n \quad t > 0, \\ &\boldsymbol{z}_s(0,x) = \boldsymbol{z}_{s,0}(x), \quad x \in [0,1], \\ &\boldsymbol{z}_d(0,x) = \boldsymbol{z}_{d,0}(x), \quad x \in [0,1], \end{aligned} \tag{35a}$$

where $\epsilon \in \mathbb{R}_+$, $\boldsymbol{f}_s : [0,\infty) \times [0,1] \times \mathbb{R}^{n_s} \times \mathbb{R}^{n_d} \to \mathbb{R}^{n_s}$ and $\boldsymbol{f}_d : [0,\infty) \times [0,1] \times \mathbb{R}^{n_s} \times \mathbb{R}^{n_d} \to \mathbb{R}^{n_d}$ are smooth functions, $\boldsymbol{D} = \text{diag}([D_1, \ldots, D_{n_d}]^T)$ such that $D_i > 0$ for all $i = 1, \ldots, n_d$, $\boldsymbol{z}^i_{s,0} : [0,1] \to \mathbb{R}_+$, $\boldsymbol{z}^i_{d,0} : [0,1] \to \mathbb{R}_+$, and

$$\boldsymbol{\mathcal{L}}_{\boldsymbol{v}}(\boldsymbol{z}_d) = \frac{d}{dx}\left[\boldsymbol{V}^2(x)\frac{d}{dx}\left[\boldsymbol{V}^{-1}(x)\boldsymbol{z}_d\right]\right] \tag{35b}$$

is such that $\boldsymbol{\mathcal{L}}_{\boldsymbol{v}} = [\mathcal{L}_{\boldsymbol{v}^1}(\boldsymbol{z}^1_d), \ldots, \mathcal{L}_{\boldsymbol{v}^{n_d}}(\boldsymbol{z}^{n_d}_d)]^T$ where $\mathcal{L}_{\boldsymbol{v}^i}(\boldsymbol{z}^i_d)$ is an in Definition 1. The elements of $\boldsymbol{z}_d$ may be thought of as "freely diffusing" and those of $\boldsymbol{z}_s$ as "spatially fixed". For the general system (35), we show in this section that the spatial profiles of the diffusing species $\boldsymbol{z}_d$, approach those of $\boldsymbol{v}(x)$, that is, the null space of $\boldsymbol{\mathcal{L}}_{\boldsymbol{v}}$ when $\epsilon \ll 1$.

Assumption 1. Consider the system given by (35)

I There exists a positively invariant set $\chi \subset \mathbb{R}^{n_s+n_d}$ such that if $[\boldsymbol{z}^T_s(0,x), \boldsymbol{z}^T_d(0,x)]^T \in \chi, \forall x \in [0,1]$, then $[\boldsymbol{z}^T_s(t,x), \boldsymbol{z}^T_d(t,x)]^T \in \chi, \forall x \in [0,1], \forall t \geq 0$.

II There exists a positive constant $M > 0$ such that

$$||\boldsymbol{f}_d(t,x,\boldsymbol{z}_s,\boldsymbol{z}_d)||_{H_d} \leq M, \quad \forall t \geq 0, \forall [\boldsymbol{z}^T_s, \boldsymbol{z}^T_d]^T \in \chi.$$

Let $\boldsymbol{z}^\perp_d(t,x) = \boldsymbol{z}_d(t,x) - \hat{\boldsymbol{V}}(x)\bar{\boldsymbol{z}}_d(t)$ where $\bar{\boldsymbol{z}}_d(t) = \int_0^1 \boldsymbol{z}_d(t,x)dx$ and $\hat{\boldsymbol{V}}(x) = \left[\int_0^1 \boldsymbol{V}(x)dx\right]^{-1}\boldsymbol{V}(x)$. The dynamics of $\boldsymbol{z}^\perp_d(t,x)$ are given by

$$\begin{aligned}
&\frac{\partial \boldsymbol{z}^\perp_d(t,x)}{\partial t} = \frac{1}{\epsilon}\boldsymbol{D}\boldsymbol{\mathcal{L}}_{\boldsymbol{v}}(\boldsymbol{z}^\perp_d) + \boldsymbol{f}^\perp_d(t,x,\boldsymbol{z}_s,\boldsymbol{z}_d), \quad t > 0, x \in (0,1),\\
&\boldsymbol{V}(x)\frac{d}{dx}\left[\boldsymbol{V}^{-1}(x)\boldsymbol{z}^\perp_d(t,x)\right]\Big|_{x=0,1} = \boldsymbol{0}_n \quad t > 0,\\
&\boldsymbol{z}^\perp_d(0,x) = \boldsymbol{z}_{d,0}(x) - \hat{\boldsymbol{V}}(x)\bar{\boldsymbol{z}}_d(0), \quad x \in (0,1),
\end{aligned} \tag{35c}$$

where

$$\boldsymbol{f}^\perp_d(t,x,\boldsymbol{z}_s,\boldsymbol{z}_d) = \boldsymbol{f}_d(t,x,\boldsymbol{z}_s,\boldsymbol{z}_d) - \hat{\boldsymbol{V}}(x)\int_0^1 \boldsymbol{f}_d(t,x,\boldsymbol{z}_s,\boldsymbol{z}_d)dx.$$

The following theorem is a direct consequence of the operator $\boldsymbol{\mathcal{L}}_{\boldsymbol{v}}$ from Definition 1 being self-adjoint and negative semi-definite. This result will show that the infinite dimensional left over dynamics $\boldsymbol{z}^\perp_d(t,x)$ become order ϵ after a fast transient.

Theorem 2. *Consider the system defined by* (35). *Suppose that Assumption 1 holds and* $[\boldsymbol{z}^T_{s,0}(x), \boldsymbol{z}^T_{d,0}(x)]^T \in \chi, \forall x \in [0,1]$, *where* χ *is defined in Assumption 1-I. Then, there exists* $\zeta, L_\perp > 0$ *such that for all* $\epsilon > 0$, *the solution* $\boldsymbol{z}^\perp_d(t,x)$ *of* (35c), *satisfies*

$$||\boldsymbol{z}^\perp_d(t,x)||_{H_d} \leq ||\boldsymbol{z}^\perp_d(0,x)||_{H_d}e^{-\zeta t/\epsilon} + L_\perp\epsilon, \quad \forall t \geq 0.$$

Proof:

Let $\psi(t) = ||\boldsymbol{z}^\perp_d(t,x)||^2_{H_d}/2$ and $\tau = t/\epsilon$ thus

$$\frac{d\psi(\tau)}{d\tau} = \langle \boldsymbol{z}^\perp_d, \frac{\partial \boldsymbol{z}^\perp_d}{\partial \tau}\rangle_{\boldsymbol{v}} = \langle \boldsymbol{z}^\perp_d, \boldsymbol{D}\boldsymbol{\mathcal{L}}_{\boldsymbol{v}}(\boldsymbol{z}^\perp_d)\rangle_{\boldsymbol{v}} + \epsilon\langle \boldsymbol{z}^\perp_d, \boldsymbol{f}^\perp_d(t,x,\boldsymbol{z}_s,\bar{\boldsymbol{z}}_d,\boldsymbol{z}^\perp_d)\rangle_{\boldsymbol{v}}.$$

The following proof uses a similar logic as the the min-max theorem for matrices [49] to derive and upper bound for $\langle \boldsymbol{z}^\perp_d, \boldsymbol{D}\boldsymbol{\mathcal{L}}_{\boldsymbol{v}}(\boldsymbol{z}^\perp_d)\rangle_{\boldsymbol{v}}$. Let $\lambda_{i,j}$ and $\psi_{i,j}$ denote the j-th eigenvalue and eigenfunction, respectively, of $\mathcal{L}_{\boldsymbol{v}^i}(\cdot)$ (i.e,. $\mathcal{L}_{\boldsymbol{v}^i}(\psi_{i,j}) = \lambda_{i,j}\psi_{i,j}$). Recall that $\{\psi_{i,j}\}$ forms a complete orthonormal basis for $L^2_{\boldsymbol{v}^i}(0,1)$ (Lemma 1-II). From the orthonormality of the eigenfunctions, linearity of $\boldsymbol{\mathcal{L}}^i_{\boldsymbol{v}} = \mathcal{L}_{\boldsymbol{v}^i}$, and the ordering of eigenvalues (Lemma 1-I), notice that:

$$
\begin{aligned}
\langle \boldsymbol{z}_d^{\perp}, \boldsymbol{D}\boldsymbol{\mathcal{L}}_{\boldsymbol{v}}(\boldsymbol{z}_d^{\perp})\rangle_{\boldsymbol{v}} &= \sum_{i=1}^{n_d} \langle \boldsymbol{z}_d^{\perp,i}, D_i \boldsymbol{\mathcal{L}}_{\boldsymbol{v}}^i(\boldsymbol{z}_d^{\perp,i})\rangle_{\boldsymbol{v}^i} \\
&= \sum_{i=1}^{n_d} \Big\langle \sum_{j=2}^{\infty} \langle \boldsymbol{z}_d^{\perp,i}, \psi_{i,j}\rangle_{\boldsymbol{v}^i} \psi_{i,j}, D_i \boldsymbol{\mathcal{L}}_{\boldsymbol{v}}^i \big(\sum_{j=2}^{\infty} \langle \boldsymbol{z}_d^{\perp,i}, \psi_{i,j}\rangle_{\boldsymbol{v}^i} \psi_{i,j} \big) \Big\rangle_{\boldsymbol{v}^i} \\
&= \sum_{i=1}^{n_d} \Big\langle \sum_{j=2}^{\infty} \langle \boldsymbol{z}_d^{\perp,i}, \psi_{i,j}\rangle_{\boldsymbol{v}^i} \psi_{i,j}, \sum_{j=2}^{\infty} \langle \boldsymbol{z}_d^{\perp,i}, \psi_{i,j}\rangle_{\boldsymbol{v}^i} D_i \boldsymbol{\mathcal{L}}_{\boldsymbol{v}}^i \big(\psi_{i,j}\big) \Big\rangle_{\boldsymbol{v}^i} \\
&= \sum_{i=1}^{n_d} \Big\langle \sum_{j=2}^{\infty} \langle \boldsymbol{z}_d^{\perp,i}, \psi_{i,j}\rangle_{\boldsymbol{v}^i} \psi_{i,j}, \sum_{j=2}^{\infty} D_i \lambda_{i,j} \langle \boldsymbol{z}_d^{\perp,i}, \psi_{i,j}\rangle_{\boldsymbol{v}^i} \psi_{i,j} \Big\rangle_{\boldsymbol{v}^i} \\
&= \sum_{i=1}^{n_d} \sum_{j=2}^{\infty} D_i \lambda_{i,j} \langle \boldsymbol{z}_d^{\perp,i}, \psi_{i,j}\rangle_{\boldsymbol{v}^i}^2 \\
&\leq \sum_{i=1}^{n_d} D_i \lambda_{i,2} \sum_{j=2}^{\infty} \langle \boldsymbol{z}_d^{\perp,i}, \psi_{i,j}\rangle_{\boldsymbol{v}^i}^2 \\
&= \sum_{i=1}^{n_d} D_i \lambda_{i,2} \langle \boldsymbol{z}_d^{\perp,i}, \boldsymbol{z}_d^{\perp,i}\rangle_{\boldsymbol{v}^i} \\
&\leq -|\bar{\lambda}_2| \langle \boldsymbol{z}_d^{\perp}, \boldsymbol{z}_d^{\perp}\rangle_{\boldsymbol{v}} \\
&= -2|\bar{\lambda}_2| \psi(\tau)
\end{aligned}
$$

where $\bar{\lambda}_2 = \max_{i=1,\dots n_d} (\{D_i \lambda_{2,i}\})$. The fact that $[\boldsymbol{z}_{s,0}^T(x), \boldsymbol{z}_{d,0}^T(x)]^T \in \chi, \forall x \in [0,1]$ implies that $[\boldsymbol{z}_s^T(t,x), \boldsymbol{z}_d^T(t,x)]^T \in \chi, \forall x \in [0,1], \forall t \geq 0$ by Assumption 1-I. By the cauchy-Schwarz inequality, Assumption 1-II, and the fact that $\boldsymbol{f}_d^{\perp}$ is a projection of $\boldsymbol{f}_d$ (thus $||\boldsymbol{f}_d^{\perp}||_{H_d}|| \leq ||\boldsymbol{f}_d||_{H_d}$) we have that $|\langle \boldsymbol{z}_d^{\perp}, \boldsymbol{f}_d^{\perp}\rangle_{\boldsymbol{v}}| \leq ||\boldsymbol{f}_d^{\perp}||_{H_d} ||\boldsymbol{z}_d^{\perp}||_{H_d} \leq M ||\boldsymbol{z}_d^{\perp}||_{H_d}$. Let $\nu \in (0,1)$ thus

$$
\begin{aligned}
\frac{d\psi(\tau)}{d\tau} &\leq -2|\bar{\lambda}_2|\psi(\tau) + \epsilon M \psi^{1/2}(\tau) \\
&\leq -2(1-\nu)|\bar{\lambda}_2|\psi(\tau) - 2\nu|\bar{\lambda}_2|\psi(\tau) + \epsilon M \psi^{1/2}(\tau) \\
&\leq -2(1-\nu)|\bar{\lambda}_2|\psi(\tau), \quad \forall \psi > \big[\frac{\epsilon M}{2\nu|\bar{\lambda}_2|}\big]^2.
\end{aligned}
$$

Therefore,

$$
\psi(\tau) \leq \psi(0) e^{-2(1-\nu)|\bar{\lambda}_2|\tau} + \big[\frac{\epsilon M}{2\nu|\bar{\lambda}_2|}\big]^2, \forall \tau \geq 0.
$$

Finally,

$$
||\boldsymbol{z}_d^{\perp}(t,x)||_{H_d} \leq ||\boldsymbol{z}_d^{\perp}(0,x)||_{H_d} e^{-\zeta t/\epsilon} + \frac{M}{\sqrt{2}\nu|\bar{\lambda}_2|}\epsilon,
$$

where $\zeta = (1-\nu)|\bar{\lambda}_2|$ and $L_{\perp} = \frac{M}{\sqrt{2}\nu|\bar{\lambda}_2|}$. ■

2.3 Model Reduction of Enzymatic-like Reaction In the Limit of Fast diffusion

The spatial-temporal dynamics of E_i, S, and c_i as described by the biochemical reactions (1) in the main text, are given in dimensionless form by

$$\begin{aligned}
\frac{\partial E_i(t,x)}{\partial t} &= -\frac{d}{dx}\big[J(x,E_i)\big] + \alpha_i(t,x) + \frac{1}{\eta_i}\Big[-E_i(t,x)S(t,x)\frac{\tilde{a}_i}{\tilde{d}_i} + c_i(t,x)\Big] \\
&\qquad - (\gamma_i+1)(E_i(t,x)+c_i(t,x)), \\
\frac{\partial c_i(t,x)}{\partial t} &= -\frac{d}{dx}\big[J(x,c_i)\big] + \frac{1}{\eta_i}\Big[E_i(t,x)S(t,x)\frac{\tilde{a}_i}{\tilde{d}_i} - c_i(t,x)\Big], \qquad (36a)\\
\frac{\partial S(t,x)}{\partial t} &= -\frac{d}{dx}\big[J(x,S)\big] + \alpha_s(t,x) + \sum_{j=1}^{n}\frac{1}{\eta_j}\Big[-E_j(t,x)S(t,x)\frac{\tilde{a}_j}{\tilde{d}_j} + c_j(t,x)\Big] \\
&\qquad - (\gamma_s+1)(S(t,x)+\sum_{j=1}^{n} c_j(t,x)),
\end{aligned}$$

where the flux term and the boundary conditions are given in Table 2 for three cases of interest, $\eta_i = 1/\tilde{d}_i$, and $\tilde{d}_i = \gamma_i + \gamma_s + d_i + \kappa_i + 1$. If applicable, $v_{E_i}(x)$, $v_s(x)$, $v_{c_i}(x)$ are the available volume profiles of E_i, S, and c_i, respectively, and let

$$\hat{v}_{E_i}(x) = \frac{v_{E_i}(x)}{\int_0^1 v_{E_i}(x)dx}, \quad \hat{v}_s(x) = \frac{v_s(x)}{\int_0^1 v_s(x)dx}, \quad \hat{v}_{c_i}(x) = \frac{v_{c_i}(x)}{\int_0^1 v_{c_i}(x)dx}. \qquad (36b)$$

Case	I: All species diffuse	II: Substrate diffuses and enzymes fixed	III: Enzymes diffuses and substrate fixed
Dimensionless Flux	$-\frac{d}{dx}\big[J(x,E_i)\big] = \frac{1}{\epsilon}\chi_{E_i}\mathcal{L}_{v_{E_i}}(E_i)$ $-\frac{d}{dx}\big[J(x,S)\big] = \frac{1}{\epsilon}\mathcal{L}_{v_S}(S)$ $-\frac{d}{dx}\big[J(x,c_i)\big] = \frac{1}{\epsilon}\chi_{c_i}\mathcal{L}_{v_{c_i}}(c_i)$	$-\frac{d}{dx}\big[J(x,E_i)\big] = 0$ $-\frac{d}{dx}\big[J(x,S)\big] = \frac{1}{\epsilon}\mathcal{L}_{v_S}(S)$ $-\frac{d}{dx}\big[J(x,c_i)\big] = 0$	$-\frac{d}{dx}\big[J(x,E_i)\big] = \frac{1}{\epsilon}\mathcal{L}_{v_{E_i}}(E_i)$ $-\frac{d}{dx}\big[J(x,S)\big] = 0$ $-\frac{d}{dx}\big[J(x,c_i)\big] = 0$
Boundary conditions	$J(0,E_i) = J(1,E_i) = 0$ $J(0,c_i) = J(1,c_i) = 0$ $J(0,S) = J(1,S) = 0$	$J(0,S) = J(1,S) = 0$	$J(0,E_i) = J(1,E_i) = 0$
ϵ	$(\mu L^2)/D_s$	$(\mu L^2)/D_s$	$(\mu L^2)/D_{E_1}$
Dimensionless diffusion	$\chi_{E_i} = D_{E_i}/D_s, \chi_{c_i} = D_{c_i}/D_s$		
Location of fixed species	N/A	x_i^*	x_s^*

Table 2: The flux dynamics and the boundary conditions corresponding to (36) for Cases I-III. Here $v_{E,i}(x)$, $v_S(x)$, and $v_{c,i}(x)$, are the available volume profiles of E_i, S, and c_i, respectively, and $\mathcal{L}_v$ is as in Definitions 1. The parameters D_{E_i}, D_{c_i}, and D_s, are the enzyme, complex, and substrate diffusion coefficients, respectively, ϵ is a dimensionless parameter that captures the speed of diffusion (with respect to dilution). A species being spatially fixed translates to the flux being zero throughout the whole spatial domain. In Case II, we denote the location of the fixed species E_i, as $x_i^* \in (0,1)$ for $i = 1,\ldots,n$. In Case III, we denote the location of the fixed species S, as $x_s^* \in (0,1)$.

We denote $\bar{E}_i(t)$, $\bar{S}(t)$, and $\bar{c}_i(t)$ to be the space averaged enzyme, substrate, and complex concentrations, respectively (e.g., $\bar{E}_i(t) = \int_0^1 E_i(t,x)dx$). The dynamics governing these space averaged variables are derived by integrating (36) in space and applying the boundary conditions and are given by:

$$\frac{d\bar{E}_i(t)}{dt} = \bar{\alpha}_i(t) - \frac{1}{\eta_i}\big[\frac{\tilde{a}_i}{\tilde{d}_i}\big[\int_0^1 E_i(t,x)S(t,x)dx\big] - \bar{c}_i(t)\big] - (\gamma_i+1)(\bar{E}_i(t)+\bar{c}_i(t)), \qquad (37a)$$

$$\frac{d\bar{c}_i(t)}{dt} = \frac{1}{\eta_i}\big[\frac{\tilde{a}_i}{\tilde{d}_i}\big[\int_0^1 E_i(t,x)S(t,x)dx\big] - \bar{c}_i(t)\big], \qquad (37b)$$

$$\frac{d\bar{S}(t)}{dt} = \bar{\alpha}_s(t) - \sum_{j=1}^{n}\frac{1}{\eta_j}\Big[\frac{\tilde{a}_j}{\tilde{d}_j}\big[\int_0^1 E_j(t,x)S(t,x)dx\big] - \bar{c}_j(t)\Big] - (\gamma_s+1)(\bar{S}(t)+\sum_{j=1}^{n}\bar{c}_j(t)), \qquad (37c)$$

where overbars denote spatially averaged variables. We make the follow assumptions necessary to state our main result

Assumption 2. Consider (36), for $i = 1, \ldots, n$, assume that

I the functions $\alpha_i(t,x)$ and $\alpha_s(t,x)$ are smooth in each argument

II there exists constant $\tilde{\alpha}_i > 0$ such that $0 < \alpha_i(t,x) \leq \tilde{\alpha}_i, \forall t \geq 0, \forall x \in [0,1]$

III there exists constant $\tilde{\alpha}_s > 0$ such that $0 \leq \alpha_s(t,x) \leq \tilde{\alpha}_s, \forall t \geq 0, \forall x \in [0,1]$

IV the functions $v_{E,i}(x)$, $v_S(x)$, and $v_{c_i}(x) = v_{E,i}(x)v_S(x)$ (as in Table 2) are smooth, strictly greater than zero, and bounded above by unity.

The following assumption makes precise what it means for the spatially fixed species $\mathrm{E_i}$ (in Case II) and S (in Case III) to be spatially localized at x_i^* and x_s^*, respectively.

Assumption 3. (Localization of spatially fixed species) Consider the system (36). Let $x_i^* \in (0,1)$ for Case II and $x_s^* \in (0,1)$ for Case III, be given by Table 2. Let $\delta^* = \min(x_1, \ldots, x_n, 1-x_1, \ldots, 1-x_n)$ for Case II and $\delta^* = \min(x_s^*, 1-x_s^*)$ for Case III. We assume that for a given $\delta > 0$ such that $\delta < \delta^*$, the functions $\alpha_i(t,x)$ and $\alpha_s(t,x)$ satisfy

- for Case II: $\alpha_i(t,x) \leq \delta$, for all $x \notin [x_i^* - \delta, x_i^* + \delta], \quad \forall t \geq 0$
- for Case III: $\alpha_s(t,x) \leq \delta$, for all $x \notin [x_s^* - \delta, x_s^* + \delta], \quad \forall t \geq 0,$

Furthermore, we assume for Cases I-III, that there exists $\bar{\alpha}_s^* > 0$, $\bar{\alpha}_{i,*} > 0$, and $\bar{\alpha}_i^* > 0$ for $i = 1, \ldots, n$ independent of δ, such that $\bar{\alpha}_{i,*} < \int_0^1 \alpha_i(t,x)dx \leq \bar{\alpha}_i^*, \forall t \geq 0$ and $\int_0^1 \alpha_s(t,x)dx \leq \bar{\alpha}_s^*, \forall t \geq 0$.

The following definition will provide the candidate reduced model to approximates (37).

Definition 3. (Reduced space-averaged dynamics) Let $x_i^* \in (0,1)$ for Case II and $x_s^* \in (0,1)$ for Case III, be given by Table 2. For $i = 1, \ldots, n$, consider the system

$$\begin{aligned}
\frac{d\hat{\bar{E}}_i(t)}{dt} &= \bar{\alpha}_i(t) - \frac{1}{\eta_i}\big[\hat{\bar{E}}_i(t)\hat{\bar{S}}(t)\frac{\tilde{a}_i\theta_i^*}{\tilde{d}_i} - \hat{\bar{c}}_i(t)\big] - (\gamma_i+1)(\hat{\bar{E}}_i(t) + \hat{\bar{c}}_i(t), \\
\frac{d\hat{\bar{c}}_i(t)}{dt} &= \frac{1}{\eta_i}\big[\hat{\bar{E}}_i(t)\hat{\bar{S}}(t)\frac{\tilde{a}_i\theta_i^*}{\tilde{d}_i} - \hat{\bar{c}}_i(t)\big], \\
\frac{d\bar{S}(t)}{dt} &= \bar{\alpha}_s(t) - \sum_{j=1}^n \frac{1}{\eta_j}\left[\hat{\bar{E}}_j(t)\hat{\bar{S}}(t)\frac{\tilde{a}_j\theta_j^*}{\tilde{d}_j} - \hat{\bar{c}}_i(t)\right] - (\gamma_s+1)(\hat{\bar{S}}(t) + \sum_{j=1}^n \hat{\bar{c}}_j(t)),
\end{aligned} \tag{38a}$$

$$\theta_i^* = \begin{cases} \int_0^1 \hat{v}_{E_i}(x)\hat{v}_S(x)dx & \text{for Case I} \\ \hat{v}_S(x_i^*) & \text{for Case II} \\ \hat{v}_{E_i}(x_s^*) & \text{for Case III} \end{cases}, \tag{38b}$$

where $\hat{\bar{E}}_i(0) = \bar{E}_i(0)$, $\hat{\bar{S}}(0) = \bar{S}(0)$, $\hat{\bar{c}}_i(0) = \bar{c}_i(0)$, as given by (37),and $\hat{v}_{E_i}(x)$, $\hat{v}_{c_i}(x)$, and $\hat{v}_S(x)$ are given by (36b).

Theorem 3. *Consider the system (36) and let*

$$\boldsymbol{z}(t,x) = [E_1(t,x), \ldots, E_n(t,x), c_1(t,x), \ldots, c_n(t,x), S(t,x)]^T, \quad \bar{\boldsymbol{z}}(t) = \int_0^1 \boldsymbol{z}(t,x)dx \tag{39}$$

Let $\epsilon > 0$, $x_i^* \in (0,1)$ and $x_s^* \in (0,1)$ be given for Case I-III by Table 2. Let $\hat{\bar{E}}_i(t)$, $\hat{\bar{S}}(t)$, and $\hat{\bar{c}}_i(t)$ be as in Definition 3 and let

$$\hat{\bar{\boldsymbol{z}}}(t) = [\hat{\bar{E}}_1(t), \ldots, \hat{\bar{E}}_n(t), \hat{\bar{c}}_1(t), \ldots, \hat{\bar{c}}_n(t), \hat{\bar{S}}(t)]^T.$$

Suppose that Assumptions 2 holds for Cases I-III. Then, there exists $L_1, \epsilon^* > 0$, $\Omega_z \subset L^2((0,1), \mathbb{R}^{2n+1})$ and $\Omega_{\bar{z}} \subset \mathbb{R}^{2n+1}$ such that for all $\boldsymbol{z}(0,x) \in \Omega_z$, $\bar{\boldsymbol{z}}(0) \in \Omega_{\bar{z}}$, $0 < \epsilon < \epsilon^*$, the solutions $\bar{\boldsymbol{z}}(t)$ and $\hat{\bar{\boldsymbol{z}}}(t)$ satisfy

$$||\bar{\boldsymbol{z}}(t) - \hat{\bar{\boldsymbol{z}}}(t)||_{\mathbb{R}^{2n+1}} \leq |\Delta_z|, \quad \forall t \geq 0, \tag{40}$$

where $|\Delta_z| = L_1\epsilon$ for Case I. For Cases II-III, if in addition, Assumption 3 holds for all $0 < \delta < \delta^*$, there exists $L_3 > 0$ such that for all $0 < \delta < \delta^*$, there exists $L_2(\delta)$ and $\Omega_{z,\delta} \subset L^2((0,1), \mathbb{R}^{2n+1})$ such that (40) holds for all $\boldsymbol{z}(0,x) \in \Omega_{z,\delta}$, $\bar{\boldsymbol{z}}(0) \in \Omega_{\bar{z}}$, $0 < \epsilon < \epsilon^*$ with $|\Delta_z| = L_2(\delta)\epsilon + L_3\delta$.

Remark 4. The constant $L_2(\delta)$, guaranteed to exist in Theorem 3 for Cases II-III, depends on δ. Therefore, for a given $\eta > 0$, if one wishes to to have $||\bar{\boldsymbol{z}}(t) - \hat{\bar{\boldsymbol{z}}}(t)||_{\mathbb{R}^{2n+1}} \leq \eta, \quad \forall t \geq 0$, then one would chose δ such that $L_3\delta < \eta$ and then choose ϵ sufficiently small (depending on δ) such that $L_2(\delta)\epsilon + L_3\delta \leq \eta$.

Remark 5. The set Ω_z, guaranteed to exist in Theorem 3, depends on δ in Cases II-III and this dependence is made precise in the proof.

Road map of proof: The rest of this section is dedicated towards proving Theorem 3. We first apply Theorem 2 to show that the spatial profile of a freely diffusing species converges to its available volume profile (e.g,. $v_{E,i}(x)$, $v_S(x)$, and $v_{c_i}(x)$) exponentially fast in the time scale associated with diffusion. If the localization assumption holds, then (37) has the form described by Definition 3, but with additional "disturbance" terms of order ϵ and δ. We proceed to demonstrate the system described in Definition 3 is contracting and apply the robustness property of contracting systems (Lemma 3) to show closeness between its solutions and those of (37).

The following result will define a positively invariant and bounded subset of $\mathbb{R}^{2n+1}$ such that solutions to (36) starting within this set at $t = 0$, remain within this set for all times and spatial values. To apply Theorem 2 to (36), the existence of such a positively invariant set is required by Assumption 1.

Claim 1. Consider the system given by (36), with Cases I-III specified by Table 2. Suppose Assumptions 2 holds. Let $\chi = \{\boldsymbol{z} \in \mathbb{R}^{2n+1} : \boldsymbol{z}^i \geq 0, \forall i \text{ and } \boldsymbol{z}^T\vec{n} \leq \Gamma\}$, where

$$\vec{n} = [\boldsymbol{b}^T, 2\boldsymbol{b}^T, 1], \quad \Gamma = \big(\sum_{j=1}^{n} \tilde{\alpha}_j + \tilde{\alpha}_S\big)/v_*, \quad v_* = \begin{cases} \min_{i=1}^{n} \min_{x\in[0,1]} \boldsymbol{v}_c & \text{for Case I} \\ \min_{x\in[0,1]} v_S(x) & \text{for Case II} \\ \min_{i=1}^{n} \min_{x\in[0,1]} \boldsymbol{v}_E & \text{for Case III} \end{cases},$$

$$\boldsymbol{b} = [1, \ldots, 1]^T \in \mathbb{R}^n, \quad \boldsymbol{v}_E = [v_{E_1}(x), \ldots, v_{E_n}(x)]^T, \quad \boldsymbol{v}_c = [v_{c_1}(x), \ldots, v_{c_n}(x)]^T.$$

Let $\boldsymbol{z}(t,x)$ be given by (39), if $\boldsymbol{z}(0,x) \in \chi, \forall x \in [0,1]$, then $\boldsymbol{z}(t,x) \in \chi, \forall t \geq 0, \forall x \in [0,1]$. Thus χ defines a positively invariant set of (36).

Proof: We apply Theorem 1 in [50], which states that for a parabolic PDE system with sufficiently smooth coefficients, a closed convex subset of euclidean space is positively invariant if the vector field corresponding to the "reaction dynamics" never points outwards at the boundaries of the set. To apply this theorem we first make a coordinate transformation. The spatial differential operator (as in Definition 1) for a general diffusing species $y(t,x)$ with available volume profile $v(x)$, given by

$$\mathcal{L}_v(y) = \frac{d}{dx}\big[v^2(x)\frac{d}{dx}(\frac{y(t,x)}{v(x)})\big] = v(x)\frac{\partial^2 y(t,x)}{\partial x^2} - y(t,x)\frac{\partial^2 v(x)}{\partial x^2},$$

is not in the standard form stipulated by Equation 1.2 in [50]. Therefore, for Cases I-III, the following coordinate transformation is made

$$\boldsymbol{u}(t,x) = \Lambda^{-1}\boldsymbol{z}(t,x), \quad \Lambda = \begin{cases} \text{diag}([\boldsymbol{v}_E^T, \boldsymbol{v}_c^T, v_S]^T) & \text{for Case I} \\ \text{diag}([\boldsymbol{b}^T, \boldsymbol{b}^T, v_S]^T) & \text{for Case II} \\ \text{diag}([\boldsymbol{v}_E^T, \boldsymbol{b}^T, 1]^T) & \text{for Case III} \end{cases}. \tag{41}$$

With the transformation $u(t,x) = y(t,x)/v(x)$, the differential operator $\hat{\mathcal{L}}_v$ given by

$$\hat{\mathcal{L}}_v(u) := \frac{1}{v}\mathcal{L}_v(uv) = v(x)\frac{\partial^2 u(t,x)}{\partial x^2} + 2\frac{\partial v(x)}{\partial x}\frac{\partial u(t,x)}{\partial x},$$

is in the postulated form. Let

$$\begin{aligned} f_{E_i}(t,x,\boldsymbol{z}) =& \alpha_i(t,x) - \frac{1}{\eta_i}\big[E_i(t,x)S(t,x)\frac{\tilde{a}_i}{\tilde{d}_i} - c_i(t,x)\big] - (\gamma_i + 1)(E_i(t,x) + c_i(t,x)), \\ f_{c_i}(t,x,\boldsymbol{z}) =& \frac{1}{\eta_i}\big[E_i(t,x)S(t,x)\frac{\tilde{a}_i}{\tilde{d}_i} - c_i(t,x)\big], \\ f_s(t,x,\boldsymbol{z}) =& \alpha_s(t,x) - \sum_{j=1}^{n}\frac{1}{\eta_j}\big[E_j(t,x)S(t,x)\frac{\tilde{a}_j}{\tilde{d}_j} - c_j(t,x)\big] - (\gamma_s + 1)(S(t,x) + \sum_{j=1}^{n} c_j(t,x)), \end{aligned} \tag{42}$$

and $\boldsymbol{f}(t,x,\boldsymbol{z}) = [f_{E_1},\dots,f_{E_n},f_{c_1},\dots,f_{c_n},f_s]^T$ is the vector field of the reaction dynamics of (36). The vector field corresponding to the reaction dynamics of the transformed system is given by $\hat{\boldsymbol{f}}(t,x,\boldsymbol{u}) := \Lambda^{-1}\boldsymbol{f}(t,x,\Lambda\boldsymbol{u})$. Let

$$\vec{n}_u(x) = \begin{cases} [\boldsymbol{v}_E^T, 2\boldsymbol{v}_c^T, v_S(x)]^T & \text{for Case I} \\ [\boldsymbol{b}^T, 2\boldsymbol{b}^T, v_S(x)]^T & \text{for Case II} \\ [\boldsymbol{v}_E^T, 2\boldsymbol{b}^T, 1]^T & \text{for Case III} \end{cases},$$

and $\chi_u(x) = \{\boldsymbol{u} \in \mathbb{R}^{2n+1} : \boldsymbol{u}^i \geq 0, \forall i \text{ and } \boldsymbol{u}^T\vec{n}_u(x) \leq \Gamma\}$. We now check that the vector field $\hat{\boldsymbol{f}}(t,x,\boldsymbol{u})$ does not point outward at all the boundary points of $\chi_u(x), \forall x \in [0,1]$. Checking that $\hat{\boldsymbol{f}}^i(t,x,\boldsymbol{u})\big|_{\boldsymbol{u}^i=0} \geq 0, \forall \boldsymbol{u} \in \chi_u(x), \forall x \in [0,1], \forall t \geq 0$ is equivalent to checking $\boldsymbol{f}^i(t,x,\boldsymbol{z})\big|_{\boldsymbol{z}^i=0} \geq 0$, thus notice that for $i = 1,\dots,n$

$$f_{E_i}(t,x,\boldsymbol{z})\big|_{E_i=0} = \alpha_i(t,x) + (d_i + \kappa_i + \gamma_s)c_i(t,x) \geq 0, \quad \forall \boldsymbol{z} \geq \boldsymbol{0}_{2n+1}, \forall x \in [0,1], \forall t \geq 0$$

$$f_{c_i}(t,x,\boldsymbol{z})\big|_{c_i=0} = \frac{1}{\eta_i}\big[E_i(t,x)S(t,x)\frac{\tilde{a}_i}{\tilde{d}_i}\big] \geq 0, \quad \forall \boldsymbol{z} \geq \boldsymbol{0}_{2n+1}, \forall x \in [0,1], \forall t \geq 0$$

and

$$f_s(t,x,\boldsymbol{z})\big|_{S=0} = \alpha_s(t,x) + \sum_{j=1}^{n}(d_j + \kappa_j + \gamma_j)c_j(t,x) \geq 0, \quad \forall \boldsymbol{z} \geq \boldsymbol{0}_{2n+1}, \forall x \in [0,1], \forall t \geq 0.$$

The set $\partial\chi_u(x) = \{\boldsymbol{u} \in \mathbb{R}^{2n+1} : \boldsymbol{u}^T(x)\vec{n}_u(x) = \Gamma\}$, corresponds to the boundary points defined by planar surface $\boldsymbol{u}^T(x)\vec{n}_u(x) = \Gamma$ with normal vector $\vec{n}_u(x)$, we need to check that for all boundary point $\boldsymbol{u}^* \in \partial\chi_u(x)$ we have that $\hat{\boldsymbol{f}}^T(t,x,\boldsymbol{u}^*) \leq 0, \forall x \in [0,1], \forall t \geq 0$:

$$\begin{aligned}
\hat{\boldsymbol{f}}^T(t,x,\boldsymbol{u}^*)\vec{n}_u(x) &= \big[\sum_{j=1}^{n}\alpha_j(t,x) - (\gamma_j+1)(\boldsymbol{u}^{j,*}\boldsymbol{\Lambda}^{j,j} + \boldsymbol{u}^{j+n,*}\boldsymbol{\Lambda}^{j+n,j+n}\big] \\
&\quad + \alpha_s(t,x) - (\gamma_s+1)(\boldsymbol{u}^{2n+1,*}\boldsymbol{\Lambda}^{2n+1,2n+1} + \sum_{j=1}^{n}\boldsymbol{u}^{j+n,*}\boldsymbol{\Lambda}^{j+n,j+n}) \\
&\leq \sum_{j=1}^{n}\tilde{\alpha}_j + \tilde{\alpha}_s - (\sum_{j=1}^{n}(\boldsymbol{u}^{j,*}\boldsymbol{\Lambda}^{j,j} + 2\boldsymbol{u}^{j+n,*}\boldsymbol{\Lambda}^{j+n,j+n}) + \boldsymbol{u}^{2n+1,*}\boldsymbol{\Lambda}^{2n+1,2n+1}) \\
&\leq \sum_{j=1}^{n}\tilde{\alpha}_j + \tilde{\alpha}_s - (\sum_{j=1}^{n}(\boldsymbol{u}^{j,*} + 2\boldsymbol{u}^{j+n,*}) + \boldsymbol{u}^{2n+1,*})v_*, \qquad \text{Assumption 2} \\
&\leq \big[\sum_{j=1}^{n}\tilde{\alpha}_j(x)\big] + \tilde{\alpha}_s(x) - \Gamma v_*, \quad \boldsymbol{u}^* \in \partial\chi_u(x), \forall x \in [0,1] \implies \boldsymbol{u}^{*,T}\vec{n} \leq \Gamma \\
&= \big[\sum_{j=1}^{n}\tilde{\alpha}_j\big] + \tilde{\alpha}_s - \big[\sum_{j=1}^{n}\tilde{\alpha}_j\big] - \tilde{\alpha}_s \\
&= 0, \quad \forall x \in [0,1], \forall t \geq 0.
\end{aligned}$$

Thus, $\chi_u(x)$ is a positively invariant set in the $\boldsymbol{u}(t,x)$ coordinates. The corresponding invariant set in the $\boldsymbol{z}(t,x)$ coordinates is given by χ. ■

Corollary 1. *The positivity of $E_i(t,x)$, $S(t,x)$, and $c_i(t,x)$ imply the positivity of $\bar{E}_i(t) = \int_0^1 E_i(t,x)dx$, $\bar{S}(t) = \int_0^1 S(t,x)dx$, and $\bar{c}_i(t) = \int_0^1 c_i(t,x)dx$.*

Definition 4. Consider the systems given by (36) and (37) and let Cases I-III correspond to those in Table 2. We define

$$\begin{aligned}
&\text{For Case I and Case III:} && E_i^{\perp}(t,x) = E_i(t,x) - \bar{E}_i(t)\hat{v}_{E_i}(x), \\
&\text{For Case I:} && c_i^{\perp}(t,x) = c_i(t,x) - \bar{c}_i(t)\hat{v}_{c_i}(x), \\
&\text{For Case I and Case II:} && S^{\perp}(t,x) = S(t,x) - \bar{S}(t)\hat{v}_S(x),
\end{aligned} \tag{43a}$$

and

$$\begin{aligned}
&\text{For Case I:} \quad \boldsymbol{w}^{\perp}(t,x) = [E_1^{\perp}, \dots, E_n^{\perp}, c_1^{\perp}, \dots, c_n^{\perp}, S^{\perp}]^T, \\
&\text{For Case II:} \quad \boldsymbol{w}^{\perp}(t,x) = S^{\perp}, \\
&\text{For Case III:} \quad \boldsymbol{w}^{\perp}(t,x) = [E_1^{\perp}, \dots, E_n^{\perp}]^T.
\end{aligned} \tag{43b}$$

Lemma 4. *Consider the systems given by (36) and let $\epsilon > 0$ be defined for Cases I-III by Table 2. Let $\boldsymbol{w}^{\perp}(t,x)$ be as in Definition 4 and suppose Assumption 2 holds. Let $\chi \subset \mathbb{R}^{2n+1}$ be as described in Claim 1 and let $\boldsymbol{z}(t,x)$ be given by (39). Then there exists $\zeta, L_{\perp} > 0$ such that for all $\boldsymbol{z}(0,x) \in \chi, \forall x \in [0,1]$ and $\epsilon > 0$, $\boldsymbol{w}^{\perp}(t,x)$ satisfies*

$$||\boldsymbol{w}^{\perp}(t,x)||_{L^2((0,1),\mathbb{R}^m)} \leq ||\boldsymbol{w}^{\perp}(0,x)||_{L^2((0,1),\mathbb{R}^m)} e^{\zeta t/\epsilon} + L_{\perp}\epsilon, \quad \forall t \geq 0,$$

where $m = 2n+1$ in Case I, $m = 1$ in Case II, and $m = n$ in Case III.

Proof: This results follows directly from Theorem 2 where Assumption 1-I is satisfied by χ and Assumption 1-II is satisfied by the smoothness of the reaction dynamics in (36), the compactness of the sets χ and $[0,1]$, and the temporal boundedness (Assumption 2). ■

Remark 6. From the proof of Theorem 2, one can observe that $L_{\perp}$ depends on the size of χ. Once Assumption 3 is made, the size of χ will depend on δ for Case II-III. Thus, $L_{\perp}$ depends on δ for Cases II-III.

Next we define the space averaged total enzyme and substrate quantities and show that these are the same for (37) and (38). Furthermore, we will show the dynamics for these quantities are governed by uncoupled, linear, and contracting ODEs.

Definition 5. (Total space average enzyme and substrate concentrations) For (37), we define the total space averaged enzyme and substrate for $i = 1. \dots, n$ as $\bar{E}_{i,T}(t) = \bar{E}_i(t) + \bar{c}_i(t)$, $\bar{S}_T(t) = \bar{S}(t) + \sum_{j=1}^n \bar{c}_j(t)$, respectively, and similarly for (38), we define $\hat{\bar{E}}_{i,T}(t) = \hat{\bar{E}}_i(t) + \hat{\bar{c}}_i(t)$ and $\hat{\bar{S}}_T(t) = \hat{\bar{S}}(t) + \sum_{j=1}^n \hat{\bar{c}}_j(t)$, the dynamics of these quantities are given by

$$\frac{d\bar{E}_{i,T}(t)}{dt} = \bar{\alpha}_i(t) - (\gamma_i + 1)\bar{E}_{i,T}(t), \quad \frac{d\bar{S}_T(t)}{dt} = \bar{\alpha}_s(t) - (\gamma_s + 1)\bar{S}_T(t), \tag{44a}$$

$$\frac{d\hat{\bar{E}}_{i,T}(t)}{dt} = \bar{\alpha}_i(t) - (\gamma_i + 1)\hat{\bar{E}}_{i,T}(t), \quad \frac{d\hat{\bar{S}}_T(t)}{dt} = \bar{\alpha}_s(t) - (\gamma_s + 1)\hat{\bar{S}}_T(t). \tag{44b}$$

Remark 7. For $i = 1, \dots, n$, $\bar{E}_{i,T}(t) = \hat{\bar{E}}_{i,T}(t), \forall t \geq 0$ and $\bar{S}_T(t) = \hat{\bar{S}}_T(t), \forall t \geq 0$ since from Definition 3, we have that $\bar{E}_{i,T}(0) = \hat{\bar{E}}_{i,T}(0)$ and $\bar{S}_T(0) = \hat{\bar{S}}_T(0)$.

Remark 8. From the linear and uncoupled structure of (44), it is clear that the dynamics for $\bar{E}_{i,T}(t)$ are contracting with contraction rate $\lambda_i = \gamma_i + 1$ for all $i = 1, \dots, n$. Similarly, the $\bar{S}_T(t)$ dynamics are contracting with contraction rate $\lambda_s = \gamma_s + 1$.

Claim 2. Consider the systems (37), (38), and (44). Let $\bar{\alpha}_i^*$, $\bar{\alpha}_{i,*}$, and $\bar{\alpha}_s^*$ be as in Assumption 3. Assume that $\bar{E}_{i,T}(0) \leq \bar{E}_{i,T}^*$, and that $\bar{S}_T(0) \leq \bar{S}_T^*$. Then

$$(I) \quad \bar{S}(t) \leq \bar{S}_T^*, \forall t \geq 0, \quad (II) \quad \hat{\bar{S}}(t) \leq \bar{S}_T^*, \forall t \geq 0, \quad (III) \quad \bar{E}_i(t) \leq \bar{E}_{i,T}^*, \forall t \geq 0,$$

where $\bar{E}_{i,T}^* = \frac{\bar{\alpha}_i^*}{\gamma_i + 1}$ and $\bar{S}_T^* = \frac{\bar{\alpha}_s^*}{\gamma_s + 1}$. Furthermore, if we assume that $\bar{E}_{i,*} \leq \bar{E}_i(0)$, where $\bar{E}_{i,*} = \frac{\bar{\alpha}_{i,*}}{\gamma_i + 1 + \tilde{a}_i \bar{S}_T^*}$, then we have that

$$(IV) \quad \bar{E}_{i,*} \leq \hat{\bar{E}}_i(t) \leq \bar{E}_{i,T}^*, \forall t \geq 0.$$

Proof: Let $\hat{\bar{S}}_T(t)$ be given by (44), and let $\hat{\bar{S}}_T^*(t)$ be given by

$$\frac{d\hat{\bar{S}}_T^*(t)}{dt} = \bar{\alpha}_s^* - (\gamma_s + 1)\hat{\bar{S}}_T^*(t) \implies \hat{\bar{S}}_T^*(t) = \hat{\bar{S}}_T^*(0)e^{-(\gamma_s+1)t} + (1 - e^{-(\gamma_s+1)t})\bar{S}_T^* \tag{45}$$

where $\hat{\bar{S}}_T^*(0) = \hat{\bar{S}}_T(0) = \bar{S}_T(0) \leq \bar{S}_T^*$, which implies that $\hat{\bar{S}}_T^*(t) \leq \bar{S}_T^*, \forall t \geq 0$. Let $e_{s,T}(t) = \hat{\bar{S}}_T^*(t) - \hat{\bar{S}}_T(t)$ such that

$$\dot{e}_{s,T}(t) = \underbrace{\bar{\alpha}_s^* - \bar{\alpha}_s(t)}_{\geq 0, \forall t \geq 0, \text{ Assumption 3}} - (\gamma_s + 1)e_s(t),$$

which implies that $\mathbb{R}_+$ is a positively invariant set for the $e_{s,T}(t)$ dynamics. Since $e_{s,T}(0) = 0$, this implies that $e_{s,T}(t) \geq 0, \forall t \geq 0$ and thus $\bar{S}_T(t) = \hat{\bar{S}}_T(t) \leq \hat{\bar{S}}_T^*(t) \leq \bar{S}_T^*, \forall t \geq 0$ (first equality from Remark 7). From the positivity of $\bar{S}(t)$ and $\bar{c}_i(t), \forall i =, \ldots, n$ (Corollary 1), we have that $\bar{S}(t) \leq \bar{S}_T(t) \leq \bar{S}_T^*, \forall t \geq 0$, thus proving (I). Similarly, $\hat{\bar{S}}(t) \leq \hat{\bar{S}}_T(t) \leq \bar{S}_T^*, \forall t \geq 0$, thus proving (II).

Let $\hat{\bar{E}}_{i,T}(t)$ be given by (44) and $\hat{\bar{E}}_i^*(t)$ be given by

$$\frac{d\hat{\bar{E}}_i^*(t)}{dt} = \bar{\alpha}_i^* - (\gamma_i + 1)\hat{\bar{E}}_i^*(t) \implies \hat{\bar{E}}_i^*(t) = \hat{\bar{E}}_i^*(0)e^{-(\gamma_i+1)t} + (1 - e^{-(\gamma_i+1)t})\bar{E}_{i,T}^*, \tag{46}$$

where $\hat{\bar{E}}_i^*(0) = \hat{\bar{E}}_{i,T}(0) = \bar{E}_{i,T}(0) \leq \bar{E}_{i,T}^*$, which implies that $\hat{\bar{E}}_i^*(t) \leq \bar{E}_{i,T}^*, \forall t \geq 0$. Let $e_{i,T}(t) = \hat{\bar{E}}_i^*(t) - \hat{\bar{E}}_{i,T}(t)$ and thus

$$\dot{e}_{i,T}(t) = \underbrace{\bar{\alpha}_i^* - \bar{\alpha}_i(t)}_{\geq 0, \forall t \geq 0, \text{ Assumption 3}} - (\gamma_i + 1)e_i(t),$$

which implies that $\mathbb{R}_+$ is a positively invariant set for the $e_{i,T}(t)$ dynamics. Since $e_{i,T}(0) = 0$, this implies that $e_{i,T}(t) \geq 0, \forall t \geq 0$ and thus $\bar{E}_{i,T}(t) = \hat{\bar{E}}_{i,T}(t) \leq \hat{\bar{E}}_i^*(t) \leq \bar{E}_{i,T}^*, \forall t \geq 0$ (first equality from Remark 7). From the positivity of $\bar{E}_i(t)$ and $\bar{c}_i(t)$ (Corollary 1), we have that $\bar{E}_i(t) \leq \bar{E}_{i,T}(t) \leq \bar{E}_{i,T}^*, \forall t \geq 0$, thus proving (III). By similar logic, we also have that $\hat{\bar{E}}_i(t) \leq \hat{\bar{E}}_{i,T}(t) \leq \bar{E}_{i,T}^*, \forall t \geq 0$, thus proving part of (IV).

Let $\hat{\bar{E}}_{i,*}(t)$ such that $\hat{\bar{E}}_{i,*}(0) = \hat{\bar{E}}_i(0)$ and

$$\frac{d\hat{\bar{E}}_{i,*}(t)}{dt} = \bar{\alpha}_{i,*} - (\gamma_i+1)\hat{\bar{E}}_{i,*}(t) - \tilde{a}_i\theta_i^*\hat{\bar{E}}_{i,*}(t)\bar{S}_T^* \implies \hat{\bar{E}}_{i,*}(t) = \hat{\bar{E}}_{i,*}(0)e^{-(\gamma_i+1+\tilde{a}_i\bar{S}_T^*)t} + (1-e^{-(\gamma_i+1+\tilde{a}_i\bar{S}_T^*)t})\bar{E}_{i,*}, \tag{47}$$

where $\hat{\bar{E}}_{i,*}(0) = \hat{\bar{E}}_i(0) = \bar{E}_i(0) \geq \bar{E}_{i,*}$, which implies that $\hat{\bar{E}}_{i,*}(t) \geq \bar{E}_{i,*}, \forall t \geq 0$. Let $e_i(t) = \hat{\bar{E}}_i(t) - \hat{\bar{E}}_{i,*}(t)$ such that

$$\dot{e}_i(t) = \underbrace{\bar{\alpha}_i(t) - \bar{\alpha}_{i,*}}_{\geq 0, \forall t \geq 0, \text{ Assumption 3}} - (\gamma_i + 1 + \tilde{a}_i\theta_i^*\bar{S}_T^*)e_i(t) + \tilde{a}_i\theta_i^*\hat{\bar{E}}_{i,*}(t)\underbrace{(\bar{S}_T^* - \hat{\bar{S}}(t))}_{\geq 0, \forall t \geq 0, \text{ by (II)}},$$

which implies that $\mathbb{R}_+$ is a positively invariant set for the $e_i(t)$ dynamics. Since $e_i(0) = 0$, this implies that $e_i(t) \geq 0, \forall t \geq 0$ and thus $\hat{\bar{E}}_{i,*}(t) \geq \bar{E}_{i,*}, \forall t \geq 0$. Thus proving (IV).

■

Remark 9. By Assumption 3, we have that $\bar{E}_{i,T}^*$ and $\bar{S}_T^*$ are independent of δ and thus these upper bounds for $\bar{E}_i(t)$ and $\bar{S}(t)$, respectively, are also independent δ.

The following results demonstrates that Assumption 3 implies that the concentration of fixed species is localized at the region specified in Table 2. The parameter $\delta > 0$, controls the amount of localization.

Proposition 1. Consider the systems given by (36). Let $x_i^* \in (0, 1)$ for Case II and $x_s^* \in (0, 1)$ for Case III, be given by Table 2. Suppose that Assumption 3 holds for x_i^*, x_s^*, and a given $\delta > 0$. Let $E_{i,T}(t, x) = E_i(t, x) + c_i(t, x)$ and $S_T(t, x) = S(t, x) + \sum_{j=1}^n c_j(t, x)$. Then, for all $E_{i,T}(0, x) \leq \delta, \forall x \notin [x_i^* - \delta, x_i^* + \delta]$ for Case II, and $S_T(0, x) \leq \delta, \forall x \notin [x_i^* - \delta, x_i^* + \delta]$ for Case III, we have that

1. Case II: $E_i(t, x) \leq \delta, \forall x \notin [x_i^* - \delta, x_i^* + \delta], \quad \forall t \geq 0, \forall i = 1, \ldots, n,$
2. Case III: $S(t, x) \leq \delta, \forall x \notin [x_s^* - \delta, x_s^* + \delta], \quad \forall t \geq 0,$

Proof: For Case II, $E_{i,T}(t, x)$ satisfies

$$\frac{\partial E_{i,T}(t, x)}{\partial t} = \alpha_i(t, x) - (\gamma_i + 1)E_{i,T}(t, x). \tag{48a}$$

For $c \notin [x_i^* - \delta, x_i^* + \delta]$ we have that $E_i(t,c) \leq E_{i,T}(t,c) \leq \frac{\alpha_i(t,c)}{\gamma_i+1} \leq \frac{1}{\gamma_i+1}\delta \leq \delta, \forall t \geq 0$. Similarly, for Case III, $S_T(t,x)$ satisfies

$$\frac{\partial S_T(t,x)}{\partial t} = \alpha_s(t,x) - (\gamma_s + 1)S_T(t,x). \tag{48b}$$

For $c \notin [x_s^* - \delta, x_s^* + \delta]$ we have that $S(t,c) \leq S_T(t,c) \leq \frac{\alpha_s(t,c)}{\gamma_s+1} \leq \frac{1}{\gamma_s+1}\delta \leq \delta, \forall t \geq 0$. ■

The following claim will aid us in rewriting (37) in the form of the reduced dynamics given by (38) with additional "disturbance" terms of order ϵ and δ. The claim is written to handle Case I-III.

Claim 3. For a given $y_1(t,x) \in H$ and $y_2(t,x) \in H$, where $H = L_2(0,1)$, suppose that $y_1(t,x), y_2(t,x) \geq 0, \forall t \geq 0, \forall x \in [0,1]$ and that there exists $y_1^*, y_2^* \in \mathbb{R}_+$ such that $||y_1(t,x)||_H \leq y_1^*, \forall t \geq 0$ and $||y_2(t,x)||_H \leq y_2^*, \forall t \geq 0$, let $\bar{y}_1(t) = \int_0^1 y_1(t,x)dx \leq \bar{y}_1^*$ and $\bar{y}_2(t) = \int_0^1 y_2(t,x)dx \leq \bar{y}_2^*$. Let $\hat{v}_1(x)$ and $\hat{v}_2(x)$ be smooth positive functions and denote $y_1^\perp(t,x) = y_1(t,x) - \bar{y}_1(t)\hat{v}_1(x)$ and $y_2^\perp(t,x) = y_2(t,x) - \bar{y}_2(t)\hat{v}_2(x)$.

1. There exists constant $k_1, k_2 > 0$ such that

$$\int_0^1 y_1(t,x)y_2(t,x)dx = \bar{y}_1(t)\bar{y}_2(t)\theta + \Delta(t), \quad \forall t \geq 0$$

   where $\theta = \int_0^1 \hat{v}_1(x)\hat{v}_2(x)dx$ and $|\Delta(t)| \leq k_1||y_1^\perp(t,x)||_H + k_2||y_2^\perp(t,x)||_H$.

2. Suppose that for a given $x^* \in (0,1)$ and $\delta > 0$ such that $[x^* - \delta, x^* + \delta] \subset [0,1]$ we have that $y_2(t,x) \leq \delta, \forall x \notin [x^* - \delta, x^* + \delta]$. Furthermore assume that $\bar{y}_1^*$ and $\bar{y}_2^*$ are independent of δ. Then there exists constant $k_3(\delta), k_4 > 0$ such that

$$\int_0^1 y_1(t,x)y_2(t,x)dx = \bar{y}_1(t)\bar{y}_2(t)\theta + \Delta(t), \quad \forall t \geq 0$$

   where $\theta = \hat{v}_1(x^*)$ and $|\Delta(t)| \leq k_3(\delta)||y_1^\perp(t,x)||_H + k_4\delta$.

Proof: To proof the first claim, notice that

$$\begin{aligned}
\int_0^1 y_1(t,x)y_2(t,x)dx &= \int_0^1 \big(\bar{y}_1(t)\hat{v}_1(x) + y_1^\perp(t,x)\big)\big(\bar{y}_2(t)\hat{v}_2(x) + y_2^\perp(t,x)\big)dx \\
&= \bar{y}_1(t)\bar{y}_2(t)\int_0^1 \hat{v}_1(x)\hat{v}_2(x)dx + \underbrace{\int_0^1 y_1^\perp(t,x)\big(\bar{y}_2(t)\hat{v}_2(x) + y_2^\perp(t,x)\big) + \bar{y}_1(t)\hat{v}_1(x)y_2^\perp(t,x)dx}_{\Delta(t)} \\
&= \bar{y}_1(t)\bar{y}_2(t)\theta + \Delta(t)
\end{aligned}$$

where $\theta = \int_0^1 \hat{v}_1(x)\hat{v}_2(x)dx$. Let $\hat{v}_1^* = \max_{x\in[0,1]}(\hat{v}_1(x))$ and leveraging the Cauchy-Schwarz inequality in H,

$$\begin{aligned}
\big|\Delta(t)\big| &= \left|\int_0^1 y_1^\perp(t,x)\big(\bar{y}_2(t)\hat{v}_2(x) + y_2^\perp(t,x)\big) + \bar{y}_1(t)\hat{v}_1(x)y_2^\perp(t,x)dx\right| \\
&= \left|\langle y_1^\perp(t,x), y_2(t,x)\rangle_H + \langle \bar{y}_1(t)\hat{v}_1(x), y_2^\perp(t,x)\rangle_H\right| \\
&\leq \left|\langle y_1^\perp(t,x), y_2(t,x)\rangle_H\right| + \left|\langle \bar{y}_1(t)\hat{v}_1(x), y_2^\perp(t,x)\rangle_H\right| \\
&\leq ||y_1^\perp(t,x)||_H||y_2(t,x)||_H + ||\bar{y}_1(t)\hat{v}_1(x)||_H||y_2^\perp(t,x)||_H \\
&\leq ||y_1^\perp(t,x)||_H y_2^* + \bar{y}_1^*\hat{v}_1^*||y_2^\perp(t,x)||_H,
\end{aligned}$$

thus $k_1 = y_2^*$ and $k_2 = \bar{y}_1^*\hat{v}_1^*$. For the second part of the claim, notice that

$$\bar{y}_2(t) = \int_0^{x^*-\delta} y_2(t,x)dx + \int_{x^*-\delta}^{x^*+\delta} y_2(t,x)dx + \int_{x^*+\delta}^1 y_2(t,x)dx = \int_{x^*-\delta}^{x^*+\delta} y_2(t,x)dx + \bar{y}_{2,\delta}(t)$$

where

$$\bar{y}_{2,\delta}(t) = \int_0^{x^*-\delta} y_2(t,x)dx + \int_{x^*+\delta}^1 y_2(t,x)dx \quad \text{and} \quad |\bar{y}_{2,\delta}(t)| \leq (x^* - \delta)\delta + (1 - x^* - \delta)\delta \leq 2\delta.$$

Next,

$$\begin{aligned}
\int_0^1 y_1(t,x)y_2(t,x)dx &= \int_0^1 \big(\bar{y}_1(t)\hat{v}_1(x) + y_1^{\perp}(t,x)\big)y_2(t,x)dx \\
&= \int_0^1 \bar{y}_1(t)\hat{v}_1(x)y_2(t,x)dx + \int_0^1 y_1^{\perp}(t,x)y_2(t,x)dx \\
&= \int_0^1 \bar{y}_1(t)\hat{v}_1(x)y_2(t,x)dx + \Delta_1(t) \\
&= \bar{y}_1(t)\big[\int_0^{x^*-\delta} \hat{v}_1(x)y_2(t,x)dx + \int_{x^*-\delta}^{x^*+\delta} \hat{v}_1(x)y_2(t,x)dx + \int_{x^*+\delta}^1 \hat{v}_1(x)y_2(t,x)dx\big] + \Delta_1(t) \\
&= \bar{y}_1(t)\int_{x^*-\delta}^{x^*+\delta} \hat{v}_1(x)y_2(t,x)dx + \Delta_2(t) + \Delta_1(t) \\
&= \bar{y}_1(t)\hat{v}_1(c)\int_{x^*-\delta}^{x^*+\delta} y_2(t,x)dx + \Delta_2(t) + \Delta_1(t), \text{ for some } c \in [x^*-\delta, x^*+\delta] \\
&= \bar{y}_1(t)\bar{y}_2(t)\hat{v}_1(c) - \bar{y}_1(t)\hat{v}_1(c)\bar{y}_{2,\delta}(t) + \Delta_2(t) + \Delta_1(t) \\
&= \bar{y}_1(t)\bar{y}_2(t)\hat{v}_1(c) + \Delta_3(t) + \Delta_2(t) + \Delta_1(t) \\
&= \bar{y}_1(t)\bar{y}_2(t)\hat{v}_1(x^*) + \Delta_4(t) + \Delta_3(t) + \Delta_2(t) + \Delta_1(t) \\
&= \bar{y}_1(t)\bar{y}_2(t)\theta + \Delta(t),
\end{aligned}$$

where $\theta = \hat{v}_1(x^*)$ and $\Delta(t) = \sum_{i=1}^4 \Delta_i(t)$, the existence of c is guaranteed by the mean-value theorem for integrals [51]. Notice that

$$|\Delta_1(t)| = \big|\int_0^1 y_1^{\perp}(t,x)y_2(t,x)dx\big| = \big|\langle y_1^{\perp}(t,x), y_2(t,x)\rangle_H\big| \leq ||y_2(t,x)||_H||y_1^{\perp}(t,x)||_H \leq y_2^*||y_1^{\perp}(t,x)||_H,$$

$$\begin{aligned}
|\Delta_2(t)| &= \Big|\bar{y}_1(t)\big[\int_0^{x^*-\delta} \hat{v}_1(x)y_2(t,x)dx + \int_{x^*+\delta}^1 \hat{v}_1(x)y_2(t,x)dx\big]\Big| \\
&\leq y_1^*\hat{v}_1^*\Big|\int_0^{x^*-\delta} y_2(t,x)dx + \int_{x^*+\delta}^1 y_2(t,x)dx\Big| \\
&= \bar{y}_1^*\hat{v}_1^*\Big|\bar{y}_{2,\delta}(t)\Big| \\
&\leq 2\bar{y}_1^*\hat{v}_1^*\delta
\end{aligned}$$

$$|\Delta_3(t)| = |\bar{y}_1(t)\hat{v}_1(c)\bar{y}_{2,\delta}(t)| \leq 2\bar{y}_1^*\hat{v}_1^*\delta,$$

the following uses the smoothness $\hat{v}_1(x)$ to guarantee uniform continuity i.e., the existence of $L_v > 0$ such that for all $x_1, x_2 \in (0,1)$, we have that $|\hat{v}_1(x_2) - \hat{v}_1(x_1)| \leq L_v|x_2 - x_1|$, and hence

$$|\Delta_4(t)| = \big|\bar{y}_1(t)\bar{y}_2(t)(\hat{v}_1(c) - \hat{v}_1(x^*))\big| \leq \bar{y}_1^*\bar{y}_2^*\big|\hat{v}_1(c) - \hat{v}_1(x^*)\big| \leq 2\bar{y}_1^*\bar{y}_2^*L_v\delta.$$

Finally,

$$\big|\Delta(t)\big| = \Big|\sum_{i=1}^4 \Delta_i(t)\Big| \leq \sum_{i=1}^4 \Big|\Delta_i(t)\Big| \leq k_3||y_1^{\perp}(t,x)||_H + k_4\delta,$$

where $k_3 = y_2^*$ and $k_4 = 2\bar{y}_1^*(2\hat{v}_1^* + \bar{y}_2^*L_v)$. ■

Remark 10. In the proof of Claim 3-2, y_2^* may depend on δ since we assume that $\bar{y}_2^*$ is independent of δ (one expects that y_2^* increases with decreasing δ), thus k_3 may depend on δ.

Corollary 2. *Consider the systems given by* (36). *The assumptions necessary to apply Claim 3 to*

$$\int_0^1 E_i(t,x)S(t,x)dx,$$

are satisfied by Claim 1, Proposition 1, and Claim 2 (along with Remark 9). Furthermore, considering the results from Lemma 4, we are guaranteed he existence of $L_i > 0$ for $i = 1, \dots, 5$ such that for all $\epsilon > 0$

$$\int_0^1 E_i(t,x)S(t,x)dx = \bar{E}_i(t)\bar{S}(t)\theta_i^* + \Delta_i(t), \quad \forall t \geq 0,$$

where θ_i^* is given by (38b) for Cases I-III (as in Table 2), and

$$|\Delta_i(t)| \leq \begin{cases} L_1\epsilon + L_2 e^{-\zeta t/\epsilon} & \text{for Case I} \\ L_3(\delta)\epsilon + L_4(\delta)e^{-\zeta t/\epsilon} + L_5\delta & \text{for Case II and Case III} \end{cases}, \tag{49}$$

where ζ is as in Lemma 4. The coefficients L_3 and L_4 may depend on δ by the discussion in Remark 6 and Remark 10.

Let $\bar{\boldsymbol{c}}(t) = [\bar{c}_1(t), \dots, \bar{c}_n(t)]^T$ where $\hat{\bar{c}}_i(t)$ is given by (37) , $\bar{\boldsymbol{E}}_T(t) = [\bar{E}_{1,T}(t), \dots, \bar{E}_{1,T}(t)]^T$ where $\bar{E}_{i,T}(t)$ is given by (44), $\hat{\bar{\boldsymbol{c}}}(t) = [\hat{\bar{c}}_1(t), \dots, \hat{\bar{c}}_n(t)]^T$, where $\hat{\bar{c}}_i(t)$ is given by (38), the $\bar{\boldsymbol{c}}(t)$ and $\hat{\bar{\boldsymbol{c}}}(t)$ dynamics may be written as

$$\frac{d\bar{\boldsymbol{c}}(t)}{dt} = \boldsymbol{f}_c(\bar{\boldsymbol{E}}_T, \bar{S}_T, \bar{\boldsymbol{c}}) + \boldsymbol{\Delta}(t), \tag{50a}$$

$$\frac{d\hat{\bar{\boldsymbol{c}}}(t)}{dt} = \boldsymbol{f}_c(\bar{\boldsymbol{E}}_T, \bar{S}_T, \hat{\bar{\boldsymbol{c}}}), \tag{50b}$$

where $\boldsymbol{\Delta}^i = \Delta_i(t)$ as in Corollary 2 and $\boldsymbol{f}_c : \mathbb{R}^n \times \mathbb{R} \times \mathbb{R}^n \to \mathbb{R}$ is given by

$$\boldsymbol{f}_c^i(\bar{\boldsymbol{E}}_T, \bar{S}_T, \hat{\bar{\boldsymbol{c}}}) = \frac{1}{\eta_i}\big[\big(\bar{\boldsymbol{E}}_T^i(t) - \hat{\bar{\boldsymbol{c}}}^i(t)\big)\big(\bar{S}_T(t) - \sum_{j=1}^n \hat{\bar{\boldsymbol{c}}}^j(t)\big)\frac{\tilde{a}_i\theta_i^*}{\tilde{d}_i} - \hat{\bar{\boldsymbol{c}}}^i(t)\big] = \frac{1}{\eta_i}\big[\hat{\bar{E}}_i(t)\hat{\bar{S}}(t)\frac{\tilde{a}_i\theta_i^*}{\tilde{d}_i} - \hat{\bar{\boldsymbol{c}}}^i(t)\big],$$

we used the fact that $\bar{E}_{i,T}(t) = \hat{\bar{E}}_{i,T}(t)$ and $\bar{S}_T(t) = \hat{\bar{S}}_T(t)$ (Remark 7). By the form of (50), it is clear that the $\bar{\boldsymbol{c}}(t)$ dynamics (50a) are in the form the $\hat{\bar{\boldsymbol{c}}}(t)$ (50b) with additional "perturbation" terms of order ϵ and δ. The variables $\bar{\boldsymbol{E}}_T(t)$, $\bar{S}_T(t)$, and $\bar{\boldsymbol{c}}(t)$ are enough to fully describe (37) and $\bar{\boldsymbol{E}}_T(t)$, $\bar{S}_T(t)$, and $\hat{\bar{\boldsymbol{c}}}(t)$ are enough to fully describe (38). Notice that

$$\frac{\partial \boldsymbol{f}_c^i(\bar{\boldsymbol{E}}_T, \bar{S}_T, \hat{\bar{\boldsymbol{c}}})}{\partial \bar{\boldsymbol{E}}_T^i} = \frac{1}{\eta_i}\hat{\bar{S}}(t)\frac{\tilde{a}_i\theta_i^*}{\tilde{d}_i}, \quad \frac{\partial \boldsymbol{f}_c^i(\bar{\boldsymbol{E}}_T, \bar{S}_T, \hat{\bar{\boldsymbol{c}}})}{\partial \bar{\boldsymbol{E}}_T^j} = 0, \quad \frac{\partial \boldsymbol{f}_c^i(\bar{\boldsymbol{E}}_T, \bar{S}_T, \hat{\bar{\boldsymbol{c}}})}{\partial \bar{\boldsymbol{S}}_T} = \frac{1}{\eta_i}\hat{\bar{E}}_i(t)\frac{\tilde{a}_i\theta_i^*}{\tilde{d}_i}, \tag{51}$$

and by Claim 2 these terms are uniformly bounded in time and for $i = 1, \dots, n$. Considering Lemma 2 with $\boldsymbol{z}_1(t) = [\bar{\boldsymbol{E}}_T^T(t), \bar{S}_T(t)]^T$ and $\boldsymbol{z}_2(t) = \hat{\bar{\boldsymbol{c}}}(t)$, then condition (I) is satisfied by the discussion in Remark 8 and condition (III) is satisfied by (51), thus we can treat $\bar{\boldsymbol{E}}_T$ and $\bar{S}_T(t)$ as time varying inputs to (50b) when showing that (II) is satisfied.

We now show that the dynamics (50b) are contracting and thus we can apply the robustness property of contracting systems (Lemma 3) to show that the solutions of (50b) and (50a) are close.

Lemma 5. *Consider the system (36) and let $\epsilon > 0$ be defined for Case I-III by Table 2. Let $\hat{\bar{\boldsymbol{c}}}(t)$ be given by (50b) and $\bar{\boldsymbol{c}}(t)$ be given by (50a). Suppose the conditions of Claim 1, Lemma 4, and Claim 2 hold. Then, there exists $L_{c,1}, \epsilon^* > 0$, such that for all $\epsilon \leq \epsilon^*$, the solutions $\hat{\bar{\boldsymbol{c}}}(t)$ and $\bar{\boldsymbol{c}}(t)$ satisfy*

$$|\hat{\bar{\boldsymbol{c}}}(t) - \bar{\boldsymbol{c}}(t)| \leq |\Delta_c|, \quad \forall t \geq 0, \tag{52}$$

where $|\Delta_c| = L_{c,1}\epsilon$ for Case I. For Cases II-III, if in addition, the conditions of Proposition 1 hold for all $0 \leq \delta \leq \delta^*$, there exists $L_{c,3} > 0$ such that for all $0 < \delta < \delta^*$, there exists $L_{c,2}(\delta)$ such that (52) is satisfied with $|\Delta_c| = L_{c,2}(\delta)\epsilon + L_{c,3}\delta$.

Proof: Consider the metric

$$\boldsymbol{P}(t) = \text{diag}([\frac{1}{\tilde{a}_1\theta_1^*\hat{\bar{E}}_1(t)}, \dots, \frac{1}{\tilde{a}_n\theta_n^*\hat{\bar{E}}_n(t)}]^T) \tag{53}$$

where $\hat{\bar{E}}_i(t)$ is given by (38). The total time derivative of $\boldsymbol{P}$ is given by

$$\dot{\boldsymbol{P}}(t) = -\boldsymbol{P}(t)\text{diag}(\boldsymbol{v}_p), \quad \text{where} \quad \boldsymbol{v}_p^i = \frac{d\hat{\bar{E}}_i(t)}{dt}/\hat{\bar{E}}_i(t) = \bar{\alpha}_i(t)/\hat{\bar{E}}_i(t) - (\gamma_i+1) - \tilde{a}_i\theta_i^*\hat{\bar{S}}(t) + (\gamma_s+k_i+d_i)\frac{\hat{\bar{c}}_i(t)}{\hat{\bar{E}}_i(t)}.$$

The Jacobian of (50b) is given by

$$\frac{\partial \boldsymbol{f}_c}{\partial \hat{\bar{\boldsymbol{c}}}} = -\text{diag}(\boldsymbol{v}_c) + \boldsymbol{\sigma}, \quad \text{where} \quad \boldsymbol{v}_c^i = \tilde{a}_i \theta_i^* \hat{\bar{S}}(t) + \tilde{d}_i,$$

and $\boldsymbol{\sigma}$ is a rank one matrix given by

$$\boldsymbol{\sigma} = [\tilde{a}_1 \theta_1^* \hat{\bar{E}}_1(t), \ldots, \tilde{a}_n \theta_n^* \hat{\bar{E}}_n(t)]^T [-1, \ldots, -1].$$

With the chosen metric $\boldsymbol{P}(t)$, we have that

$$\boldsymbol{P}\boldsymbol{\sigma} = -\underbrace{[1, \ldots, 1]^T [1, \ldots, 1]}_{\boldsymbol{\sigma}_1} \implies -n\boldsymbol{I}_{n,n} \leq \boldsymbol{\sigma}_1 \leq 0\boldsymbol{I}_{n,n}$$

since the symmetric rank one matrix $\boldsymbol{\sigma}_1$, has $n-1$ zero eigenvalues and the nontrivial eigenvalue is $\lambda_\sigma = -n$ for eigenvector $v_n = [1, \ldots, 1]^T$. Recalling the positivity of $\hat{\bar{E}}_i(t)$, $\hat{\bar{c}}_i(t)$, $\hat{\bar{S}}(t)$ (Claim 1), and $\bar{\alpha}_i(t)$, we have that

$$\begin{aligned}
1/2\left(\boldsymbol{P}(t)\frac{\partial \boldsymbol{f}_c}{\partial \boldsymbol{c}} + \frac{\partial \boldsymbol{f}_c^T}{\partial \boldsymbol{c}}\boldsymbol{P}(t) + \dot{\boldsymbol{P}}(t)\right) &= -\boldsymbol{P}\text{diag}(1/2\boldsymbol{v}_p + \boldsymbol{v}_c) + \boldsymbol{P}\boldsymbol{\sigma} \\
&\leq -\boldsymbol{P}\text{diag}(1/2\boldsymbol{v}_p + \boldsymbol{v}_c) \\
&\leq -\min_{i=1,\ldots,n}\left(1/2(\gamma_i + 1) + \gamma_s + \kappa_i + d_i\right)\boldsymbol{P} \\
&= -\xi\boldsymbol{P}.
\end{aligned}$$

By Theorem 1, the system (50b) is contracting with contraction rate $\xi = 1/2 + \gamma_s + \min_{i=1,\ldots,n}\left(1/2\gamma_i + \kappa_i + d_i\right)$. Assumptions 2, 3 imply that (49) holds for $\Delta_i(t)$ in (50a). Therefore, for a given $\delta > 0$, we apply the result from Lemma 3 to the nominal system (50b) and the perturbed system (50a). Let $\epsilon^* = \zeta/(2\xi)$ and recalling that $\bar{c}_i(0) = \hat{\bar{c}}_i(0)$, then by Lemma 3, there exists $l_1, l_2(\delta), l_3 > 0$ such that for all $\epsilon < \epsilon^*$

$$|\bar{c}_i(t) - \hat{\bar{c}}_i(t)| \leq Ml_1\epsilon, \quad \forall t \geq 0, \text{ for Case I} \quad |\bar{c}_i(t) - \hat{\bar{c}}_i(t)| \leq M(l_2(\delta)\epsilon + l_3\delta), \quad \forall t \geq 0, \text{ for Case II-III},$$

where M is a constant upper bound on the square root of the ratio of the biggest and smallest eigenvalues of $\boldsymbol{P}(t)$. Thus $L_{c,1} = Ml_1$, $L_{c,2}(\delta) = Ml_2(\delta)$, and $L_{c,3} = Ml_3$. We now show that M exists. Let $r(t)$ be the ratio of the biggest and smallest eigenvalues of $\boldsymbol{P}(t)$. By Claim 2, there exists $\bar{E}_{i,*}, \bar{E}_{i,T}^* \in \mathbb{R}_+$ independent of ϵ and δ such that $\bar{E}_{i,*} \leq \hat{\bar{E}}_i(t) \leq \bar{E}_{i,T}^*, \forall t \geq 0$, and thus

$$r(t) = \frac{\max_{i=1,\ldots,n} \tilde{a}_i\theta_i^* \hat{\bar{E}}_i(t)}{\min_{i=1,\ldots,n} \tilde{a}_i\theta_i^* \hat{\bar{E}}_i(t)} \leq \frac{\max_{i=1,\ldots,n} \tilde{a}_i\theta_i^* \bar{E}_{i,T}^*}{\min_{i=1,\ldots,n} \tilde{a}_i\theta_i^* \bar{E}_{i,*}} \implies M^2 = \frac{\max_{i=1,\ldots,n} \tilde{a}_i\theta_i^* \bar{E}_{i,T}^*}{\min_{i=1,\ldots,n} \tilde{a}_i\theta_i^* \bar{E}_{i,*}}.$$

■

Corollary 3. *Recall Definition 5 and Remark 7, we have that*

$$|\bar{E}_i(t) - \hat{\bar{E}}_i(t)| = |\bar{E}_{i,T}(t) - \bar{c}_i(t) - (\hat{\bar{E}}_{i,T}(t) - \hat{\bar{c}}_i(t))| = |\hat{\bar{c}}_i(t) - \bar{c}_i(t)| \leq |\Delta_c|$$

and

$$|\bar{S}(t) - \hat{\bar{S}}(t)| = |\bar{S}_T(t) - \sum_{j=1}^n \bar{c}_j(t) - (\hat{\bar{S}}_T(t) - \sum_{j=1}^n \hat{\bar{c}}_j(t))| = |\sum_{j=1}^n \hat{\bar{c}}_j(t) - \bar{c}_j(t)| \leq \sum_{j=1}^n |\hat{\bar{c}}_j(t) - \bar{c}_j(t)| \leq n|\Delta_c|$$

where $|\Delta_c|$ is as in Lemma 5. Thus, the quantity $|\Delta_z|$ as claimed to exist in Theorem 3, may be given by $|\Delta_z| = |\Delta_c|\sqrt{2 + n^2}$.

Remark 11. We now comment on the sets $\Omega_z \in \mathbb{R}^{n+1}$ and $\Omega_{\bar{z}} \in \mathbb{R}^{n+1}$ as claimed to exist in Theorem 3. Let χ be as in Claim 1.

- For Cases I-III we require that $\boldsymbol{z}(0,x) \in \chi, \forall x \in [0,1]$ for Lemma 4 to hold. In Case I, $\Omega_z \in \mathbb{R}^{n+1} = \chi$. In Case II, for Proposition 1 to hold we also require that for $i = 1 \ldots, n$, that $E_i(0,x)+c_i(0,x) \leq \delta, \forall x \notin [x_i^* - \delta, x_i^* + \delta]$, thus Ω_z is the intersection between the set that satisfies this condition and χ. In Case III, for Proposition 1 to hold we also require that $S(0,x)+\sum_{j=1}^n c_j(0,x) \leq \delta, \forall x \notin [x_i^* - \delta, x_i^* + \delta]$, thus Ω_z is the intersection between the set that satisfies this condition and χ. As discussed in Remark 6, χ may depend on δ.

- For Claim 2 to hold, we assumed that $\bar{E}_{i,*} \leq \bar{E}_i(0)$, $\bar{E}_i(0)+\bar{c}_i(0) \leq \bar{E}_{i,T}^*$, and that $\bar{S}(0)+\sum_{j=1}^n \bar{c}_j(0) \leq \bar{S}_T^*$, thus $\Omega_{\tilde{z}}$ is the set that satisfies these conditions.

2.4 Fast Diffusion and Bingding Dynamics

The approximation result of Theorem 3, holds well if $\boldsymbol{w}^\perp$ is small, where $\boldsymbol{w}^\perp$ is given by Definition 4. This was guaranteed by Lemma 4 which is based on Theorem 2. The proof of Theorem 2 was based on the principle that the $\frac{1}{\epsilon}\boldsymbol{D}\boldsymbol{\mathcal{L}}_{\boldsymbol{v}}(\boldsymbol{z}_d^\perp)$ term dominates the $\boldsymbol{f}_d^\perp(t,x,\boldsymbol{z}_s,\boldsymbol{z}_d)$ term in (35c) and thus all solutions converged to $z_d^\perp \to 0$, the quasi-steady state of $\frac{1}{\epsilon}\boldsymbol{D}\boldsymbol{\mathcal{L}}_{\boldsymbol{v}}(\boldsymbol{z}_d^\perp)$. However, for (36), if ϵ and η_i are of similar order of magnitude, the corresponding term in $\boldsymbol{f}_d^\perp(t,x,\boldsymbol{z}_s,\boldsymbol{z}_d)$ may be comparable to $\frac{1}{\epsilon}\boldsymbol{D}\boldsymbol{\mathcal{L}}_{\boldsymbol{v}}(\boldsymbol{z}_d^\perp)$ and cannot be neglected. The terms ϵ and η_i being comparable corresponds to diffusion and the binding between $\mathrm{E_i}$ and S occurring at similar timescales, which often time occurs within the cell [2]. Here we show that when both diffusion and the binding dynamics dominate in (36), $z_d^\perp = 0$ is still the quasi-steady state, that is, all freely diffusing species mirror their available volume profile.

When both diffusion and the binding dynamics dominate in (36) we have that

$$\begin{aligned}
\frac{\partial E_i(t,x)}{\partial t} &= \underbrace{\frac{1}{\eta_i}\Big[-\eta_i\frac{d}{dx}\big[J(x,E_i)\big] - E_i(t,x)S(t,x)\frac{\tilde{a}_i}{\tilde{d}_i} + c_i(t,x)\Big]}_{\text{fast}} + \alpha_i(t,x) \\
&\qquad - (\gamma_i+1)(E_i(t,x)+c_i(t,x)), \\
\frac{\partial c_i(t,x)}{\partial t} &= \underbrace{\frac{1}{\eta_i}\Big[-\eta_i\frac{d}{dx}\big[J(x,c_i)\big] + E_i(t,x)S(t,x)\frac{\tilde{a}_i}{\tilde{d}_i} - c_i(t,x)\Big]}_{\text{fast}}, \\
\frac{\partial S(t,x)}{\partial t} &= \underbrace{\frac{1}{\eta_1}\Big[-\eta_1\frac{d}{dx}\big[J(x,S)\big] + \sum_{j=1}^n \frac{\eta_1}{\eta_j}(-E_j(t,x)S(t,x)\frac{\tilde{a}_j}{\tilde{d}_j} + c_j(t,x))\Big]}_{\text{fast}} + \alpha_s(t,x) \\
&\qquad - (\gamma_s+1)(S(t,x)+\sum_{j=1}^n c_j(t,x)).
\end{aligned} \tag{54}$$

We compute the quasi-steady state of the "fast dynamics in (54) for Cases I-III, that is $E_i(t,x)$, $c_i(t,x)$, and $S(t,x)$ such that

$$\begin{aligned}
0 &= \frac{1}{\eta_i}\Big[-\eta_i\frac{d}{dx}\big[J(x,E_i)\big] - E_i(t,x)S(t,x)\frac{\tilde{a}_i}{\tilde{d}_i} + c_i(t,x)\Big], \\
0 &= \frac{1}{\eta_i}\Big[-\eta_i\frac{d}{dx}\big[J(x,c_i)\big] + E_i(t,x)S(t,x)\frac{\tilde{a}_i}{\tilde{d}_i} - c_i(t,x)\Big], \\
0 &= \frac{1}{\eta_1}\Big[-\eta_1\frac{d}{dx}\big[J(x,S)\big] + \sum_{j=1}^n \frac{\eta_1}{\eta_j}(-E_j(t,x)S(t,x)\frac{\tilde{a}_j}{\tilde{d}_j} + c_j(t,x))\Big].
\end{aligned} \tag{55}$$

Case I: In this case, (55) is satisfied for

$$E_i(t,x) = \bar{E}_i(t)\hat{v}_{E_i}(x), \quad S(t,x) = \bar{S}(t)\hat{v}_S(x), \quad c_i(t,x) = \bar{c}_i(t)\hat{v}_{c_i}(x),$$

with the additional constraint that

$$E_i(t,x)S(t,x)\frac{\tilde{a}_i}{\tilde{d}_i} + c_i(t,x) = 0 \implies \bar{E}_i(t)\hat{v}_{E_i}(x)\bar{S}(t)\hat{v}_S(x)\frac{\tilde{a}_i}{\tilde{d}_i} + \bar{c}_i(t)\hat{v}_{c_i}(x) = 0, \forall x \in [0,1], \tag{56}$$

which in general (56) is a stringent condition since it is required to hold for all $x \in [0,1]$. However, by the key fact that $v_{c_i}(x) = v_{E_i}(x)v_S(x)$ ((9) in the main text), (56) is satisfied for all $x \in [0,1]$ by

$$\bar{c}_i(t) = \bar{E}_i(t)\bar{S}(t)\frac{\tilde{a}_i}{\tilde{d}_i}\theta_i^*, \quad \text{where} \quad \theta_i^* = \frac{\int_0^1 v_{E_i}(x)v_S(x)dx}{\left[\int_0^1 v_{E_i}(x)dx\right]\left[\int_0^1 v_S(x)dx\right]}.$$

Case II and III: For this cases, (55) is satisfied for

$$\text{Case II:} \quad S(t,x) = \bar{S}(t)\hat{v}_S(x), \quad \text{Case III:} \quad E_i(t,x) = \bar{E}_i(t)\hat{v}_{E_i}(x),$$

with the additional constraint that $E_i(t,x)S(t,x)\frac{\tilde{a}_i}{\tilde{d}_i} + c_i(t,x) = 0$ which implies that

$$\text{Case II:} \quad c_i(t,x) = E_i(t,x)\bar{S}(t)\hat{v}_S(x)\frac{\tilde{a}_i}{\tilde{d}_i}, \quad \text{Case III:} \quad E_i(t,x) = \bar{E}_i(t)\hat{v}_{E_i}(x)S(t,x)\frac{\tilde{a}_i}{\tilde{d}_i}. \tag{57}$$

Thus, when both diffusion and the binding dynamics dominate, the quasi-steady states are still those that correspond to freely diffusing species converging to their available volume profile. We observed that for Case I, this was possible by the fact that $v_{c_i}(x) = v_{E_i}(x)v_S(x)$. In a future study it should be shown that this quasi-steady state is a stable solution of the fast dynamics in (54).

2.5 Available Volume Profiles and Bounds on θ_i^*

Following [13], we introduce a model of the available volume profiles of a freely diffusing species within the DNA mesh of the cell. Let $\rho(x)$ be the local density of DNA length such that $\int_0^1 \rho(x)dx = \bar{\rho} = \frac{L_p}{V_p}$, where L_p is the total length of chromosome DNA, V_p the volume where the DNA polymer is confined, and let $\hat{\rho}(x) = \frac{\rho(x)}{2\bar{\rho}}$. For a species diffusing inside the cell with radius of gyration r, we model the available volume profile $v(x)$ as:

$$v(x) = e^{-\kappa\pi r^2 2\bar{\rho}\hat{\rho}(x)} = e^{-(r/r^*)^2\hat{\rho}(x)}, \tag{58}$$

where κ is an empirical coefficient (as discussed in [13]) and $r^{*2} = 1/(2\kappa\pi\bar{\rho})$. From the parameter values in [13], $r^* \approx 23$ nm. As commented in SI Section 2.11, r^* can be estimated for a given context (e.g., growth conditions and strain) by analyzing the concentration profile inside the cell of a freely diffusing species with a known radius of gyration, which is possible via superresolution imaging [14].

As shown in Figure 8, we estimate the chromosome density as a step function.

$$\hat{\rho}(x) = \begin{cases} \dfrac{1}{2(1-\Delta x)}, & x \in [0, 1-\Delta x] \\ 0, & x \in (1-\Delta x, 1] \end{cases} \implies \bar{v} = \int_0^1 v(x)dx = v_0(1-\Delta x) + \Delta x, \tag{59}$$

where $v_0 = e^{-\frac{(r/r^*)^2}{2(1-\Delta x)}}$ and Δx is the distance between the end of the chromosome and the cell poles (see Figure 1 in the main text). Its clear now, that our choice to define $\hat{\rho}(x) = \frac{\rho(x)}{2\bar{\rho}}$ was motivated by the fact that when $\Delta_x = 1/2$ (nucleoid evenly spread out between mid-cell and the halfway point between mid-cell and the cell poles), we have the convenient expressions $\hat{\rho}(0) = 1$ and $v_0 = e^{-(r/r^*)^2}$. Notice that $v_0 \to 0$ as $(r/r^*)^2 \to \infty$. Thus,

$$\hat{v}(x) = \frac{v(x)}{\bar{v}(x)} = \begin{cases} 0 \le \dfrac{v_0}{v_0(1-\Delta x) + \Delta x} \le 1, & x \in [0, 1-\Delta x] \\ 1 \le \dfrac{1}{v_0(1-\Delta x) + \Delta x} \le \dfrac{1}{\Delta x}, & x \in (1-\Delta x, 1] \end{cases}$$

Bounds on θ_i^* (13): For the species $\mathrm{E_i}$ and S as described in the main text with radius of gyration $r_{e,i}$ and r_s, respectively. The available volume profiles are given by

$$v_{E_i}(x) = e^{-(r_{e,i}/r^*)^2\hat{\rho}(x)} \quad \text{and} \quad v_S(x) = e^{-(r_s/r^*)^2\hat{\rho}(x)},$$

respectively, We summarize the bounds on θ_i^* as in (13) in the main text, assuming $\rho(x)$ is a step function as above. Let

$$v_{0,E_i} = v_{E_i}(0) = e^{-\frac{(r_{e,i}/r^*)^2}{2(1-\Delta x)}}, \quad \text{and} \quad v_{0,S} = v_S(0) = e^{-\frac{(r_s/r^*)^2}{2(1-\Delta x)}}, \tag{60}$$

and Case I-III as in (13) in the main text, the bounds on θ_i^* are given by

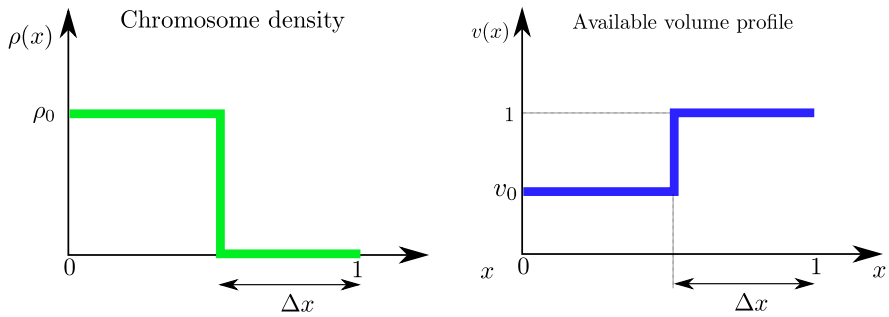

Figure 8: **Idealization of the chromosome density which yields a simple estimate of the available volume profile.** The chromosome density is approximated as a step function implying by (58) that the available volume profile is also a step function. Here Δx is the distance between the end of the chromosome and the cell poles.

- For **Case I**, this idealization implies that

$$\theta_i^* = \frac{v_{0,E_i} v_{0,S}(1-\Delta x) + \Delta x}{\left[v_{0,E_i}(1-\Delta x) + \Delta x\right]\left[v_{0,S}(1-\Delta x) + \Delta x\right]} \implies 1 \leq \theta_i \leq \frac{1}{\Delta x} \tag{61a}$$

  The upper limit of θ_i^* is $\frac{1}{\Delta x}$ and is reached as v_{0,E_i} <u>and</u> $v_{0,S}$ approach zero, which occurs as $r_{e,i}/r^* \to \infty$ and $r_s/r^* \to \infty$. The lower limit of θ_i^* is unity and is achieved if v_{0,E_i} <u>or</u> $v_{0,S}$ approach one, which occurs if any of the two species is sufficiently small ($r_{e,i}/r^* \ll 1$ or $r_s/r^* \ll 1$). Since $\theta_i^* \geq 1$, it implies that the binding betwen $\mathrm{E_i}$ and S is always equal to or greater than that predicted by a well-mixed model ((8) in the main text).

- For **Case II-III**, let x_i^* and x_s^* as in Assumption 3 in the main text and thus

$$a_i = \begin{cases} v_{0,S}, & \text{Case II} \\ v_{0,E_i}, & \text{Case III} \end{cases}, \tag{61b}$$

$$\theta_i^* = \begin{cases} 0 \leq \dfrac{a_i}{a_i(1-\Delta x) + \Delta x} \leq 1, & x_i^* \leq 1-\Delta x \text{ for Case II and } x_s^* \leq 1-\Delta x \text{ for Case III} \\ 1 \leq \dfrac{1}{a_i(1-\Delta x) + \Delta x} \leq \dfrac{1}{\Delta x}. & x_i^* > 1-\Delta x \text{ for Case II and } x_s^* > 1-\Delta x \text{ for Case III} \end{cases} \tag{61c}$$

  When $x_i^* \leq 1-\Delta x$ for Case II and $x_s^* \leq 1-\Delta x$ for Case III, we have that $\theta_i^* \leq 1$, the lower limit $\theta_i^* = 0$ is achieved when $r_e/r^* \to \infty$ for Case II ($r_s/r^* \to \infty$ for Case III), the upper limit $\theta_i^* = 1$ is achieved when $r_e/r^* \to 0$ for Case II ($r_s/r^* \to 0$ for Case III). When $x_i^* > 1-\Delta x$ for Case II and $x_s^* > 1-\Delta x$ for Case III, we have that $\theta_i^* \geq 1$, the lower limit $\theta_i^* = 1$ is achieved when $r_e/r^* \to 0$ for Case II ($r_s/r^* \to \infty$ for Case III), the upper limit $\theta_i^* = 1/\Delta x$ is achieved when $r_e/r^* \to \infty$ for Case II ($r_s/r^* \to \infty$ for Case III).

2.6 Protein Production: Transcription and Translation

We consider gene (D) being transcribed by RNAP (S) to form a DNA-RNAP complex (c_s) to produce mRNA (m) which is translated by ribosomes (R) to form mRNA-ribosome complex (c_m) which produces protein P. The mRNA's degrade at rate γ. The RNAP, and ribosomes are produced at rates $\alpha_s(t,x)$, $\alpha_r(t,x)$, respectively. We assume all species dilute at rate μ, the cells growth rate. The corresponding biochemical reactions are:

$$\underbrace{\mathrm{D} + \mathrm{S} \underset{\mathrm{d_s}}{\overset{\mathrm{a_s}}{\rightleftharpoons}} \mathrm{c_s} \xrightarrow{\kappa_\mathrm{s}} \mathrm{m} + \mathrm{S} + \mathrm{D}}_{\text{transcription, case II}}, \quad \underbrace{\mathrm{m} + \mathrm{R} \underset{\mathrm{d_m}}{\overset{\mathrm{a_m}}{\rightleftharpoons}} \mathrm{c_m} \xrightarrow{\kappa_\mathrm{m}} \mathrm{P} + \mathrm{R} + \mathrm{m}}_{\text{translation, case I}}$$

$$\emptyset \xrightarrow{\alpha_\mathrm{s}} \mathrm{S}, \quad \emptyset \xrightarrow{\alpha_\mathrm{r}} \mathrm{R}, \quad \mathrm{m} \xrightarrow{\gamma_\mathrm{i}} \emptyset, \quad \mathrm{C_m} \xrightarrow{\gamma_\mathrm{i}} \mathrm{R},$$

where γ is the mRNA degradation rate, a_s and d_s are the association and dissociation rate constants, respectively, between RNAP and the gene D, κ_s is the catalytic rate of formation of mRNA m, a_m and d_m

are the association and dissociation rate constants, respectively, between ribosomes and mRNA , κ_m is the catalytic rate of formation of protein P. We assume that the total concentration of D is conserved, so that $D_T(x) = D(t,x) + c_s(t,x)$ and that $D_T(x)$ is localized at $x = x^*$.

Spatial-temporal Dynamics: The dynamics corresponding to these biochemical reactions are given by:

$$\frac{\partial c_s(t,x)}{\partial t} = a_s S(t,x)D(t,x) - (d_s + \kappa_s)c_s(t,x) - c_s(t,x), \tag{62a}$$

$$\frac{\partial S(t,x)}{\partial t} = \mathcal{L}_s(S) + \alpha_s(t,x) + \big[- a_{s,i}D(t,x)S(t,x) + (d_s + \kappa_s)c_s(t,x)\big] - S(t,x), \tag{62b}$$

$$\frac{\partial m(t,x)}{\partial t} = \mathcal{L}_m(m) + \kappa_s c_s(t,x) - a_m m(t,x)R(t,x) + (\kappa_m + d_m)c_m(t,x) - (1+\gamma)m(t,x), \tag{62c}$$

$$\frac{\partial c_m(t,x)}{\partial t} = \mathcal{L}_c(c_m) + a_m m(t,x)R(t,x) - (\kappa_m + d_m + 1 + \gamma)c_m, \tag{62d}$$

$$\frac{\partial R(t,x)}{\partial t} = \mathcal{L}_R(R) + \alpha_R(t,x) + \big[a_m m(t,x)R(t,x) + (\kappa_m + d_m + \gamma)c_m(t,x)\big] - R(t,x). \tag{62e}$$

where the spatial variable has been normalized by L (cell-length) and the time variable has been normalized by $1/\mu$ the time scale associated with dilution. The flux dynamics and boundary conditions are given by,

$$\mathcal{L}_m(m) = -\frac{d}{dx}\big[J_m(x,m)\big], \quad J_m(x,m) = -\chi_m v_m(x)^2 \frac{d}{dx}\big[v_m(x)^{-1}m\big], \quad J_m(x,m)\big|_{x=0,1} = 0, \tag{63a}$$

$$\mathcal{L}_c(c_m) = -\frac{d}{dx}\big[J_c(x,c_m)\big], \quad J_c(x,c_m) = -\chi_c v_c(x)^2 \frac{d}{dx}\big[v_c(x)^{-1}c_m\big], \quad J_c(x,c_m)\big|_{x=0,1} = 0, \tag{63b}$$

$$\mathcal{L}_R(R) = -\frac{d}{dx}\big[J_R(x,R)\big], \quad J_R(x,R) = -\chi_R v_R(x)^2 \frac{d}{dx}\big[v_R(x)^{-1}R\big], \quad J_R(x,R)\big|_{x=0,1} = 0, \tag{63c}$$

$$\mathcal{L}_s(S) = -\frac{d}{dx}\big[J_s(x,S)\big], \quad J_s(x,S) = -\chi_s v_s(x)^2 \frac{d}{dx}\big[v_s(x)^{-1}S\big], \quad J_s(x,S)\big|_{x=0,1} = 0. \tag{63d}$$

where $v_m(x)$, $v_c(x)$, $v_R(x)$, and $v_s(x)$ are the available volume profiles for the mRNA, mRNA-ribosome complex, ribosome, and RNAP, respectively and $\chi_m = D_m/(L^2\mu)$, $\chi_c = D_c/(L^2\mu)$, $\chi_R = D_R/(L^2\mu)$, and $\chi_s = D_s/(L^2\mu)$, are the dimensionless diffusion coefficients for the mRNA, mRNA-ribosome complex, ribosome, and RNAP, respectively. The space averaged protein concentration $\bar{P}(t)$ is given by

$$\frac{d\bar{P}(t)}{dt} = \kappa_m \bar{c}_m(t) - \bar{P}(t), \quad \text{with} \quad \bar{c}_m(t) = \int_0^1 c_m(t,x)dx.$$

Values for dimensionless parameters:

We set all production rates with respect to that of RNAP such that $\bar{\alpha}_S = \int_0^1 \alpha_S(x)dx = 1$. All time scales relative to $\mu = 0.5$ 1/hr, consistent with the experiments [52] The total number of RNAP (N_{RNAP}) ranges between 2,000 -10,000 we took it to be 5,000 [14]. The total number of ribosomes (N_{ribo}) was taken to be $10,000$ and since both RNAP and ribosomes and RNAP are stable, it implies $\bar{\alpha}_r = \int_0^1 \alpha_r(x)dx = \frac{N_{\text{ribo}}}{N_{\text{RNAP}}} = 2$. mRNA degradation is about 10 times faster than dilution [2], therefore, $\gamma = 10$.The rate of transcription (translation) is about 80 (40) times faster than dilution [2], thus we choose $\kappa_s = 80$ and $\kappa_m = 40$. We assumed that the DNA is on a high copy plasmid (≈ 500 copies) and thus $\bar{D}_T = \int_0^1 D_T(x)dx = \frac{N_{\text{DNA}}}{N_{\text{RNAP}}} = 0.1$.

The association and dissociation rate constants are varied as shown below to show that all of our results hold dispiite fast binding and unbinding but we maintain the ratio $d_s/a_s = d_m/a_m = 1$.

The length of the cell is about 3μm and thus $L = 1.5\mu$m [13]. The diffusion coefficient of RNAP is taken to be $D_s = 0.22\mu m^2/s$ [53] and thus $\chi_s = 704$. The diffusion coefficient of free ribosomes is taken to be $D_r = 0.4\mu m^2/s$ [13] and thus $\chi_r = 1280$. In [14], the diffusion coefficient of polysomes is $0.05 \pm 0.02\mu m^2/s$, and thus we take the diffusion coefficient of a free mRNA to be the upper bound $0.07\mu m^2/s$ and thus $\chi_m = \chi_c = 224$.

For the following, the spatial profiles for the production rates are given proportional to their functional form since the constant that fully specifies them is such that the production rate per-cell satisfies the above values.

Additional simulation details for Figure 5-A in the main text: $D_T(x) \propto e^{-20x}$ when DNA near mid cell and $D_T(x) \propto e^{20(x-1)}$ when DNA at cell poles. The RNAP production was kept roughly spatially constant $\alpha_s(x) \propto e^{-.001x}$. The binding and unbinding coefficients for DNA-RNAP were $a_s = 1000$ and $d_s = 1000$. We set $a_m = d_m = 0$ such that mRNA did not bind to ribosomes and thus the free amount of mRNA is equivalent to the total mRNA.
Additional simulation details for Figure 5-B in the main text: $D_T(x) \propto e^{-.001x}$ is chosen to be roughly constant. The RNAP production was kept roughly spatially constant $\alpha_s(x) \propto e^{-.001x}$. The ribosome production was kept roughly spatially constant $\alpha_r(x) \propto e^{-.001x}$. The RNAP radius of gyration was taken to be $r_s/r^* = 0.001$ such that its excluded volume effects were negligible. The binding and unbinding coefficients for DNA-RNAP were $a_s = 1000$ and $d_s = 1000$. The binding and unbinding coefficients for ribosome-mRNA were $a_m = 10$ and $d_m = 10$.

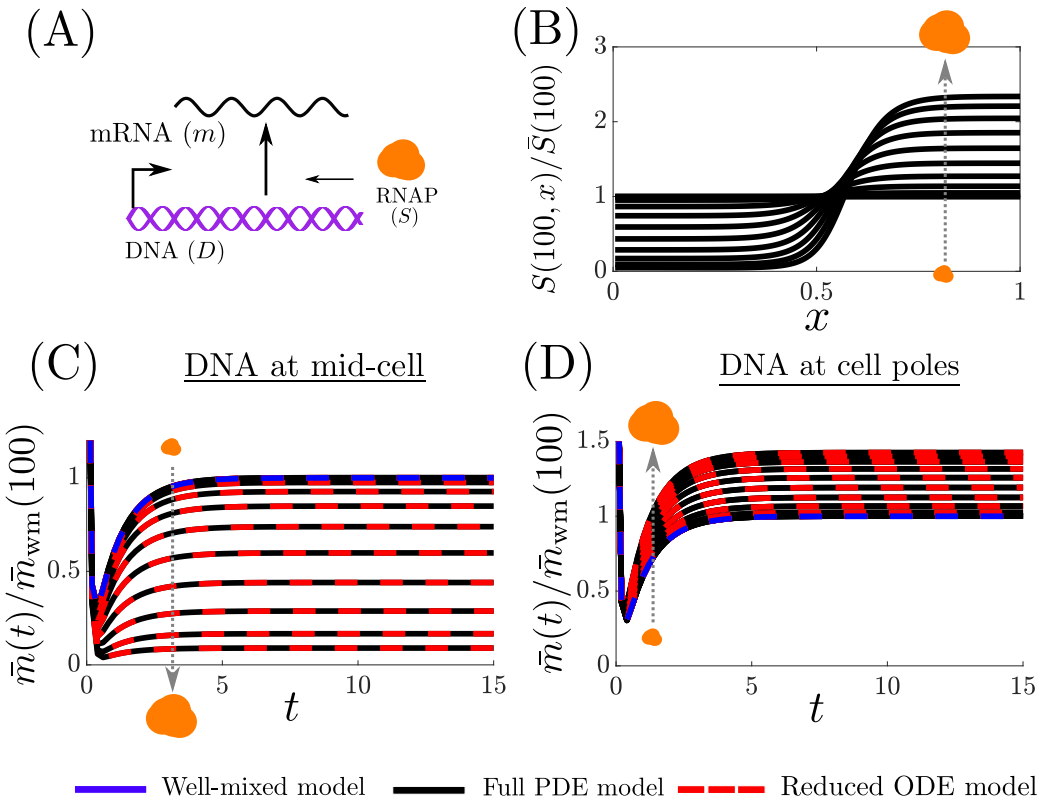

Figure 9: **RNAP steady state spatial profiles and space averaged mRNA transients** For the following we refer to the well-mixed model as (15) with (16) given by $\theta_s = 1$ and $\theta_r = 1$. Here time is nondimensionalized with the time scale associated with dilution. (A) DNA transcribed by RNAP (S) to form mRNA (m) (B) The steady state RNAP spatial profile predicted by (62), normalized by spatial averaged value. From the results on the main text this should mirror the normalized available volume profile, which it does (Remark 1). Note as the size of RNAP increases, it is further excluded from the chromosome. (C) The temporal space-average concentration of mRNA when the DNA is localized mid-cell for several sizes of RNAP for the well-mixed model, reduced ODE model (15) , and PDE (62). (D) The temporal space-average concentration of mRNA when the DNA is localized near the cell poles for several sizes of RNAP for the well-mixed model, reduced ODE model (15) , and PDE (62). The simulation set up and parameters are identical to those of Figure 5-A.

2.7 Multiple Ribosomes on a Single Strand of mRNA

The biochemical reactions that models a polysome with N_r bound ribosomes are given by

$$\underbrace{\mathrm{m} + (\mathrm{N_r} - 1)\mathrm{R} \underset{\mathrm{d_l}}{\overset{\mathrm{a_l}}{\rightleftharpoons}} \mathrm{c_l}}_{\text{ribosome loading}}, \quad \underbrace{\mathrm{c_l} + \mathrm{R} \underset{\mathrm{d_t}}{\overset{\mathrm{a_t}}{\rightleftharpoons}} \mathrm{c_t} \xrightarrow{\kappa_t} \mathrm{P} + \mathrm{R} + \mathrm{c_l}}_{\text{translation}}, \tag{64}$$

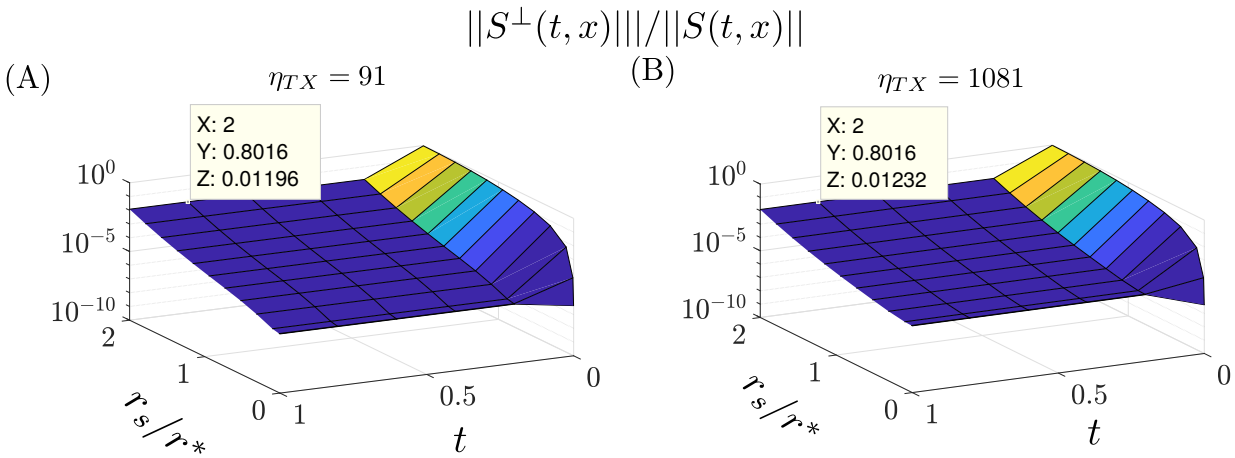

Figure 10: **The error in the RNAP approximation for several binding and unbinding speeds between DNA and RNAP** Let $S(t,x)$ be as in (62) and $S^{\perp}(t,x) = S(t,x) - \bar{S}(t)\hat{v}_s(x)$ be the a measure of the error in our approximation, where $||y(t,x)|| = (\int_0^1 (y^2(t,x)))^{1/2}$, and $\eta_{\text{TX}} = 1/(\kappa_s + d_s + 1)$. The values of η_{TX} are varied by modifying d_s while maintaining $a_s/d_s = 1$. Here time is nondimensionalized with the time scale associated with dilution. (A) The relative error in time for several values of r_s for $\eta_{\text{TX}} = 91 \implies d_s = 10$. (B) The relative error in time for several values of r_s for $\eta_{\text{TX}} = 1081 \implies d_s = 1000$. For both values of η_{TX} the error is high at $t = 0$ since the initial RNAP spatial profile is chosen to be a constant but quickly decays to less than 2%. The rest of the simulation set up and parameters are identical to those of Figure 5-A.

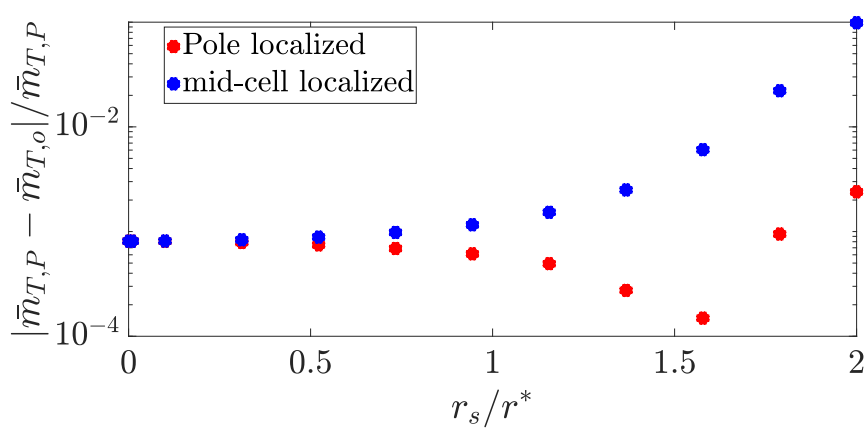

Figure 11: **The relative error between the space averaged PDE model and the reduced ODE model from the data in Figure 5-a in the main text** The relative error in the steady state space averaged mRNA for the full PDE model ($\bar{m}_{T,P}$) and the reduced model ($\bar{m}_{T,o}$) from the data in Figure 5-a in the main text. When the DNA is pole localized the relative error is less than 1% and when the DNA is localized near mid-cell the error is less than 10%.

where the first and second reaction model the loading and translation steps, respectively. The translation dynamics corresponding to (64) are given by

$$\frac{\partial m(t,x)}{\partial t} = \mathcal{L}_m(m) + \kappa_s c_s(t,x) - a_l m(t,x) R^{N_r-1}(t,x) + d_l c_l(t,x) - (1+\gamma) m(t,x), \tag{65a}$$

$$\frac{\partial c_l(t,x)}{\partial t} = \mathcal{L}_{c,l}(c_l) + a_l m(t,x) R^{N_r-1}(t,x) - d_l c_l(t,x) - a_t c_l(t,x) R(t,x) + (d_t + \kappa_t) c_t(t,x) - (\gamma+1) c_l(t,x), \tag{65b}$$

$$\frac{\partial R(t,x)}{\partial t} = \mathcal{L}_R(R) + \alpha_R(t,x) + (N_r - 1)\big[a_l m(t,x) R^{N_r-1}(t,x) - d_l c_l(t,x)\big] \tag{65c}$$

$$- a_t c_l(t,x) R(t,x) + (d_t + \kappa_t) c_t(t,x) - R(t,x), \tag{65d}$$

$$\frac{\partial c_t(t,x)}{\partial t} = \mathcal{L}_{c,t}(c_t) + a_t c_l(t,x) R - (d_t + \kappa_t) c_t(t,x) - (\gamma+1) c_t(t,x), \tag{65e}$$

$$\tag{65f}$$

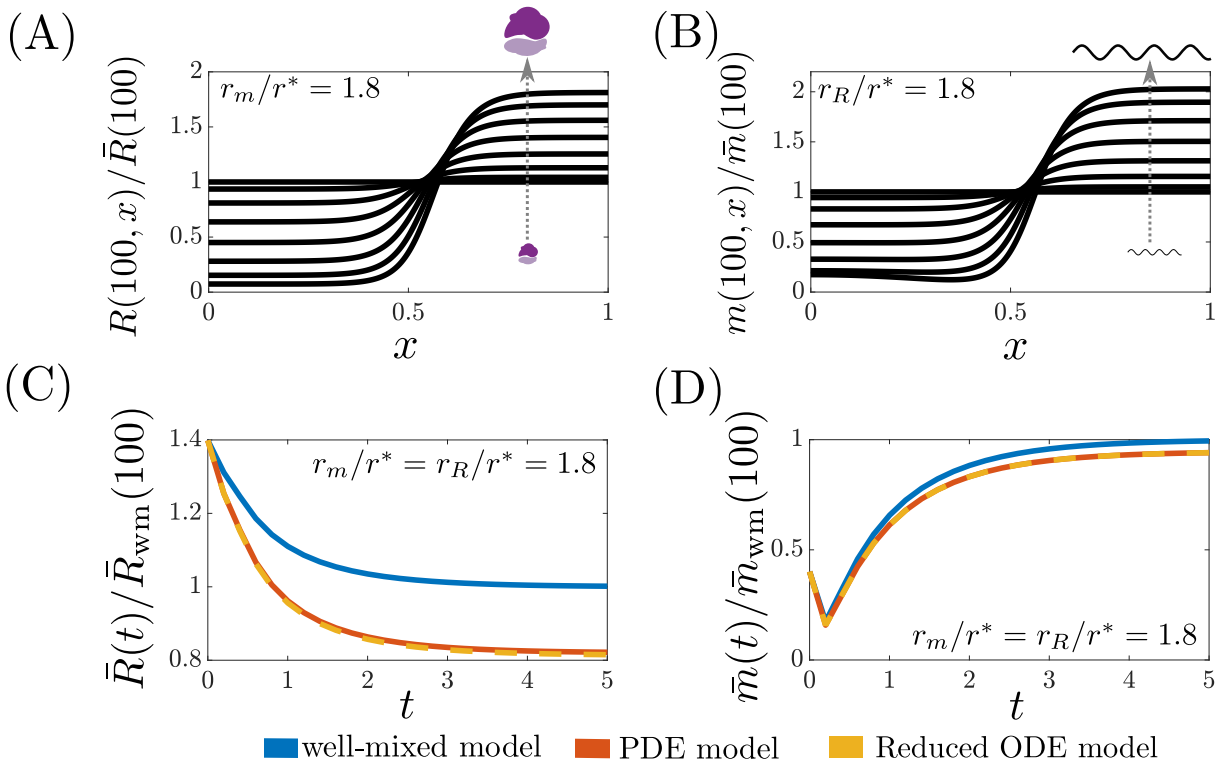

Figure 12: **Ribosome and mRNA steady state spatial profiles and space averaged transients** For the following we refer to the well-mixed model as (15) with (16) given by $\theta_s = 1$ and $\theta_r = 1$. Here time is nondimensionalized with the time scale associated with dilution. (A) The steady state ribosome spatial profile predicted by (62), normalized by spatial averaged value. From the results on the main text this should mirror the normalized available volume profile, which it does. Note as the size of the ribosome increases, it is further excluded from the chromosome. (B) The steady state mRNA spatial profile predicted by (62), normalized by spatial averaged value. From the results on the main text this should mirror the normalized available volume profile, which it does. Note as the size of the mRNA increases, it is further excluded from the chromosome. (C) The temporal space averaged concentration of ribosomes normalized by the steady state of the well-mixed model for the reduced ODE model (15) and the PDE model (62) when $r_m/r^* = r_R/r^* = 1.8$. (D)The temporal space averaged concentration of mRNA normalized by the steady state of the well-mixed model for the reduced ODE model (15) and the PDE model (62) when $r_m/r^* = r_R/r^* = 1.8$. The simulation set up and parameters are identical to those of Figure 5-B.

where $c_s(t,x)$ is given by (62), $\mathcal{L}_m(m)$ and $\mathcal{L}_R(R)$ are given by (63) and

$$\mathcal{L}_{c,l}(c_l) = -\frac{d}{dx}\big[J_{c,l}(x,c_l)\big], \quad J_{c,l}(x,c_l) = -\chi_c v_l(x)^2 \frac{d}{dx}\big[v_l(x)^{-1}c_l\big], \quad J_{c,l}(x,c_l)\big|_{x=0,1} = 0,$$

$$\mathcal{L}_{c,t}(c_t) = -\frac{d}{dx}\big[J_{c,t}(x,c_t)\big], \quad J_{c,t}(x,c_t) = -\chi_c v_t(x)^2 \frac{d}{dx}\big[v_t(x)^{-1}c_t\big], \quad J_{c,t}(x,c_t)\big|_{x=0,1} = 0,$$

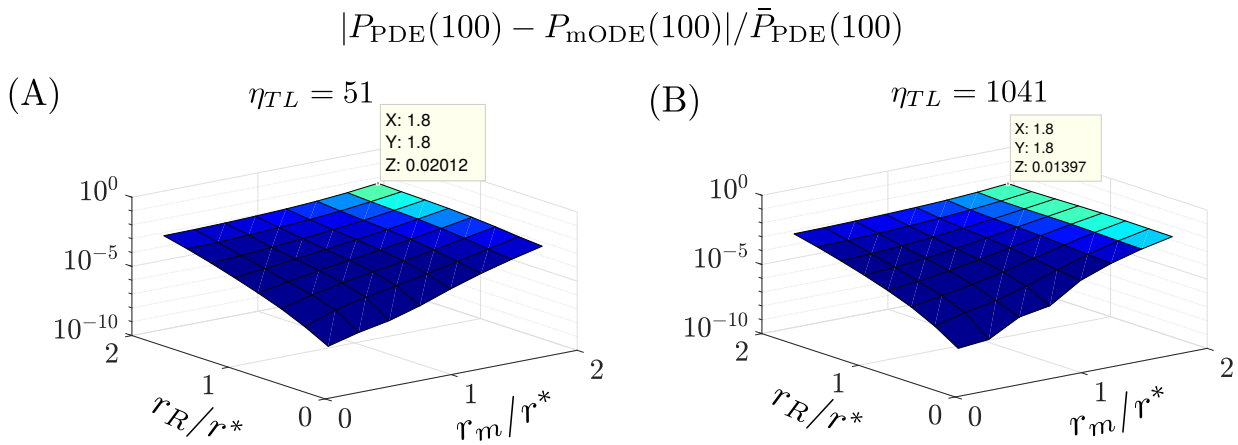

Figure 13: **PDE and reduced ODE model agree well in protein production example** Let $P_{\mathrm{PDE}}(100)$ be the steady state protein space averaged concentration predicted by (62) and $P_{\mathrm{ODE}}(100)$ be the steady state protein space averaged concentration predicted by (15). Let $\eta_{\mathrm{TL}} = 1/(\kappa_m + d_m + 1 + \gamma_m)$. The values of η_{TL} are varied by modifying d_m while maintaining $a_m/d_m = 1$. (A) The relative error for several values of r_m and r_s for $\eta_{\mathrm{TL}} = 51 \implies d_m = 10$. (B) The relative error for several values of r_m and r_s for $\eta_{\mathrm{TX}} = 1041 \implies d_m = 1000$. For both cases the relative error is less than 2.1% The rest of the simulation set up and parameters are identical to those of Figure 5-B.

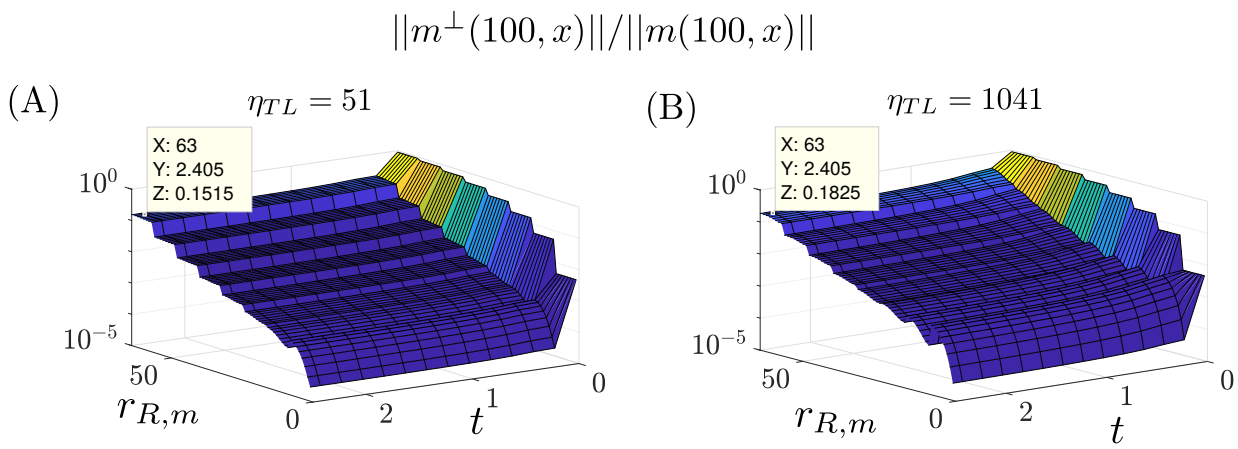

Figure 14: **The error in the mRNA approximation for several binding and unbinding speeds between mRNA and ribosome** Let $m(t,x)$ be as in (62) and $m^{\perp}(t,x) = m(t,x) - \bar{m}(t)\hat{v}_m(x)$ be the a measure of the error in our approximation, where $||y(t,x)|| = (\int_0^1 (y^2(t,x)))^{1/2}$, and $\eta_{\mathrm{TL}} = 1/(\kappa_m + d_m + 1 + \gamma_m)$. The values of η_{TL} are varied by modifying d_m while maintaining $a_m/d_m = 1$. Here r_R, m is a sequence corresponding to the mRNA and ribosome pairs from Figure 5-B. Here time nondimensionalized with the time scale associated with dilution. (A) The relative error in time for several values of r_R, m for $\eta_{\mathrm{TL}} = 51 \implies d_s = 10$. (B) The relative error in time for several values of r_R, m for $\eta_{\mathrm{TL}} = 1041 \implies d_s = 1000$. For both values of η_{TL} the error is high at $t = 0$ since the initial mRNA spatial profile is chosen to be a constant but quickly decays to less than 20%. The rest of the simulation set up and parameters are identical to those of Figure 5-B.

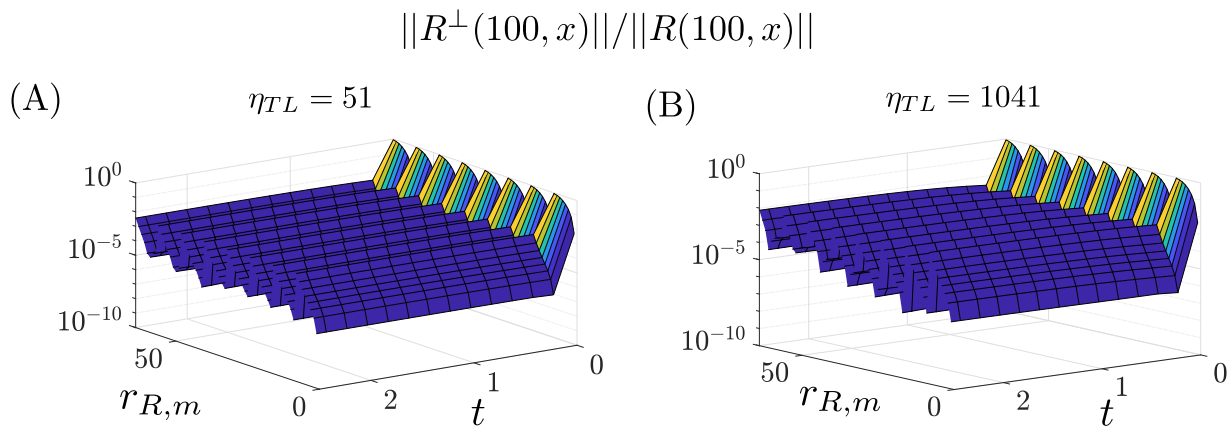

Figure 15: **The error in the ribosome approximation for several binding and unbinding speeds between mRNA and ribosome** Let $m(t,x)$ be as in (62) and $R^{\perp}(t,x) = R(t,x) - \bar{R}(t)\hat{v}_r(x)$ be the a measure of the error in our approximation, where $||y(t,x)|| = (\int_0^1 (y^2(t,x)))^{1/2}$, and $\eta_{\text{TL}} = 1/(\kappa_m + d_m + 1 + \gamma_m)$. The values of η_{TL} are varied by modifying d_m while maintaining $a_m/d_m = 1$. Here r_R, m is a sequence corresponding to the mRNA and ribosome pairs from Figure 5-B. Here time nondimensionalized with the time scale associated with dilution. (A) The relative error in time for several values of r_R, m for $\eta_{\text{TL}} = 51 \implies d_s = 10$. (B) The relative error in time for several values of r_R, m for $\eta_{\text{TL}} = 1041 \implies d_s = 1000$. For both values of η_{TL} the error is high at $t = 0$ since the initial mRNA spatial profile is chosen to be a constant but quickly decays to less than 1%. The rest of the simulation set up and parameters are identical to those of Figure 5-B.

where $v_l(x) = v_m(x)v_R^{N_r-1}(x)$ and $v_t(x) = v_l(x)v_R(x)$. Integrating (65) in space yields:

$$\frac{d\bar{m}(t)}{dt} = \kappa_s \bar{c}_s(t) - a_l\theta_l(t)\bar{m}(t)\bar{R}^{N_r-1}(t) + d_l\bar{c}_l(t) - (1+\gamma)\bar{m}(t), \tag{66a}$$

$$\frac{d\bar{c}_l(t)}{dt} = a_l\theta_l(t)\bar{m}(t)\bar{R}^{N_r-1}(t) - d_l\bar{c}_l(t) - a_t\theta_t(t)\bar{c}_l(t)\bar{R}(t) + (d_t+\kappa_t)\bar{c}_t(t) - (\gamma+1)\bar{c}_l(t), \tag{66b}$$

$$\frac{d\bar{R}(t)}{dt} = \bar{\alpha}_R(t) + (N_r-1)\big[a_l\theta_l(t)\bar{m}(x)\bar{R}^{N_r-1}(t) - d_l\bar{c}_l(t)\big] \tag{66c}$$

$$- a_t\theta_t(t)\bar{c}_l(t)\bar{R}(t,x) + (d_t+\kappa_t)\bar{c}_t(t) - \bar{R}(t), \tag{66d}$$

$$\frac{d\bar{c}_t(t)}{dt} = a_t\theta_t(t)\bar{c}_l(t)\bar{R}(t) - (d_t+\kappa_t)\bar{c}_t(t) - (\gamma+1)\bar{c}_t(t), \tag{66e}$$

$$\frac{d\bar{P}(t)}{dt} = \kappa_t\bar{c}_t(t) - \bar{P}(t) \tag{66f}$$

where

$$\theta_l(t) = \frac{\int_0^1 m(t,x)R^{N_r-1}(t,x)dx}{[\int_0^1 m(t,x)dx][\int_0^1 R(t,x)dx]^{N_r-1}}, \quad \theta_t(t) = \frac{\int_0^1 c_l(t,x)R(t,x)dx}{[\int_0^1 c_l(t,x)dx][\int_0^1 R(t,x)dx]}. \tag{67}$$

The production rate of $\bar{P}$ denoted by $\bar{\alpha}_P$ is given by $\bar{\alpha}_P = \kappa_t\bar{c}_t(t)$. From our analysis in Section 2.2, we expect that $R(t,x) \approx \bar{R}(t)\hat{v}_r(x)$, $m(t,x) \approx \bar{m}(t)\hat{v}_m(x)$, and $c_l(t,x) \approx \bar{c}_l(t)v_l(x)$ (this is verified computationally in Figure 16), and thus we can estimate $\theta_l^*(t)$ and $\theta_t^*(t)$ by the constants

$$\theta_l(t) \approx \theta_l^* = \frac{\int_0^1 v_m(x)v_R^{N_r-1}(x)dx}{[\int_0^1 v_m(x)dx][\int_0^1 v_R(x)dx]^{N_r-1}}, \quad \theta_t(t) \approx \theta_t^* = \frac{\int_0^1 v_l(x)v_R(x)dx}{[\int_0^1 v_l(x)dx][\int_0^1 v_R(x)dx]}, \tag{68}$$

this is verified via simulation in Figure 16)-D.

Let $K_d = (d_l/a_l)^{1/(N_r-1)}$, $K_t = (d_t+\kappa_t)/a_t$, $\beta_l = (\gamma+1)/d_l$, and $\beta_t = (\gamma+1)/(\kappa_t+d_t)$, if $\beta_l, \beta_t, \beta_t R/K_t \ll 1$ (dilution and mRNA degradation is much slower the rate of ribosome unbinding and K_t is sufficiently large),

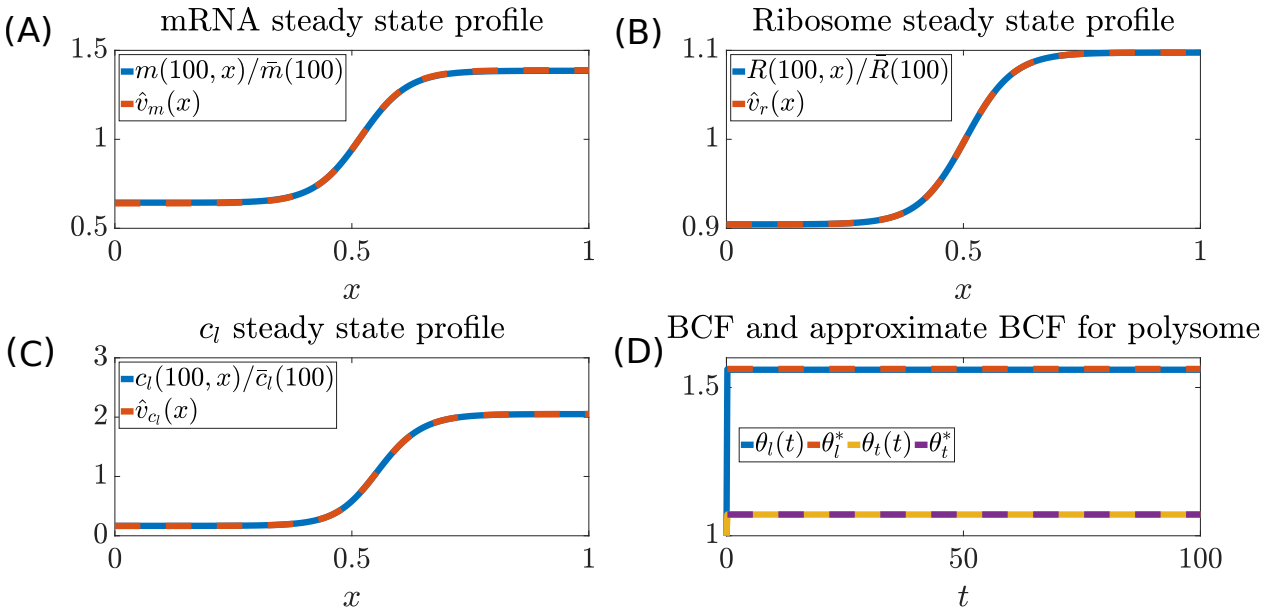

Figure 16: **BCF for Polysome with 10 Ribosomes** (A) The steady state mRNA spatial concentration profile ($m(100,x)$) predicted by (65) normalized by the space averaged concentration along with the normalized mRNA available volume profile ($\hat{v}_m(x) = v_m(x)/\int_0^1 v_m(x)dx$). (B) The steady state ribosome spatial concentration profile ($R(100,x)$) predicted by (65) normalized by the space averaged concentration along with the normalized mRNA available volume profile ($\hat{v}_r(x) = v_r(x)/\int_0^1 v_r(x)dx$). (C) The steady state polysome (loaded with 9 ribosomes) spatial concentration profile ($c_l(100,x)$) predicted by (65) normalized by the space averaged concentration along with the normalized mRNA available volume profile ($\hat{v}_{c_l}(x) = v_{c_l}(x)/\int_0^1 v_{c_l}(x)dx$). (D) The BCF's $\theta_l(t)$ and $\theta_t(t)$ given by (67) and their constant approximation θ_l^* and θ_t^* given by (68). For these simulations, we do not model transcription directly but instead set $\kappa_s c_s(t,x) = 1$, such that at steady state $m_T(x) = m(x) + c_l(x) + c_t(x) = \kappa_s c_s(t,x)/(\gamma+1) = 0.09$ for $\gamma = 10$. The used parameter values are $N_r = 10$, $\chi_m = \chi_c = 224$, $\chi_r = 1280$, $a_t = 10$, $d_t = 10$, $\kappa_t = 40$, $a_l = a_t^{N_r-1}$ $d_l = d_t^{N_r-1}$, $\alpha_r(t,x) = 1$, $r_m/r^* = 0.88$ and $r_R/r^* = 0.44$.

then a simple expression for the steady state protein is given by

$$\bar{P} = \kappa_t \bar{c}_t = \kappa_t \bar{m}_T \underbrace{\theta_t^* \bar{R}/K_t}_{\text{translation}} \underbrace{\frac{\theta_l^* (\bar{R}/K_d)^{N_r-1}}{1+\theta_l^*(\bar{R}/K_d)^{N_r-1}}}_{\text{ribosome loading}},$$

where $\bar{m}_T = \bar{m} + \bar{c}_l + \bar{c}_t = \kappa_s \bar{c}_s/(\gamma+1)$ is the total mRNA.

2.8 Transcription Factor Regulation

Intracellular signaling to control gene expression is often done via transcription factors (TFs). In this section we model a general transcription factor architecture where the repressor $\mathrm{P_r}$ dimerizes to form $\mathrm{c_1}$ (e.g., TetR dimerizes before targeting gene [32]) and then blocks the transcription of gene D that produces protein P. The biochemical reactions corresponding to this process are:

$$\emptyset \xrightarrow{\alpha} \mathrm{P_r}, \quad \underbrace{\mathrm{P_r} + \mathrm{P_r} \underset{\mathrm{d_1}}{\overset{\mathrm{a_1}}{\rightleftharpoons}} \mathrm{c_1}}_{\text{Case I}}, \quad \underbrace{\mathrm{c_1} + \mathrm{D} \underset{\mathrm{d_2}}{\overset{\mathrm{a_2}}{\rightleftharpoons}} \mathrm{c_2}}_{\text{Case II}}, \quad \mathrm{D} \xrightarrow{\kappa} \mathrm{P}, \tag{69}$$

where α is the production rate of $\mathrm{P_r}$, a_1 (d_1) is the association (dissociation) constant to form the $\mathrm{c_1}$ complex, a_2 (d_2) is the association (dissociation) constant to form the the $\mathrm{c_2}$ complex, and κ is the catalytic rate to produce protein P. Since the repressor $\mathrm{P_r}$, freely diffuses, the dimerization reaction belongs to Case I. The gene D is spatially fixed and it is repressed by the freely diffusing $\mathrm{c_1}$, thus this interaction falls under Case II.

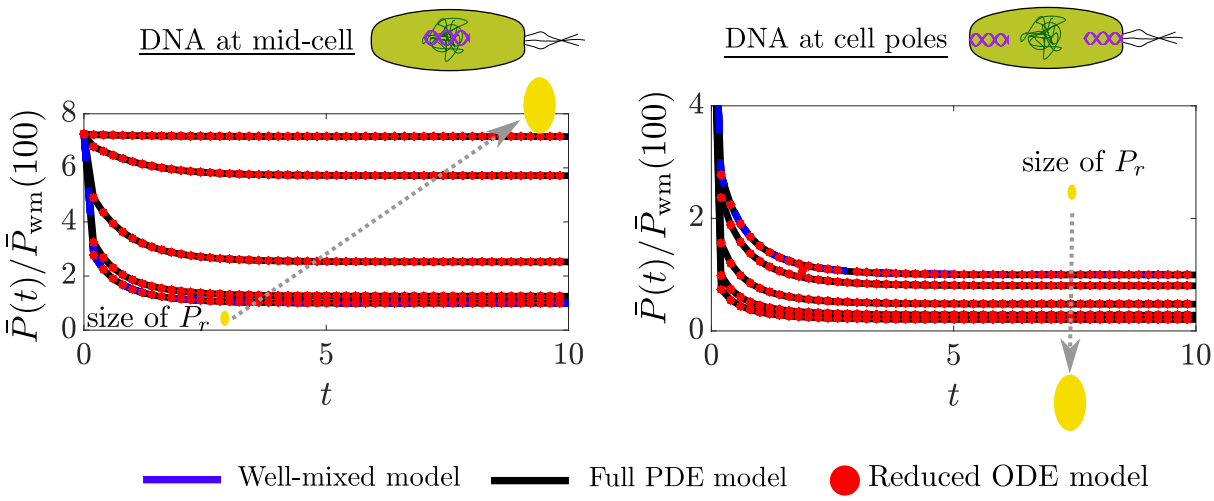

Figure 17: **Transcription factor regulation transient response** The transient response corresponding to Figure 6 in the main text when $\bar{P}_r/K = 2.5$

We assume that the total concentration of D is conserved, so that $D_T(x) = D(t,x) + c_2(t,x)$. The reaction diffusion equations corresponding to (69) are

$$\frac{\partial P_r(t,x)}{\partial t} = \chi_r \frac{d}{dx}\left[v_{P_r}^2(x)\frac{d}{dx}\left[\frac{P_r(t,x)}{v_{P_r}(x)}\right]\right] + \alpha(t,x) - \gamma_r P_r(t,x), \tag{70a}$$

$$\frac{\partial c_1(t,x)}{\partial t} = \chi_c \frac{d}{dx}\left[v_{c_1}^2(x)\frac{d}{dx}\left[\frac{c_1(t,x)}{v_{c_1}(x)}\right]\right] + a_1 P_r^2(t,x) - d_1 c_1(t,x) - a_2 c_1(t,x) D(t,x) + d_2 c_2(t,x), \tag{70b}$$

$$\frac{\partial c_2(t,x)}{\partial t} = a_2 c_1(t,x) D(t,x) - d_2 c_2(t,x), \tag{70c}$$

$$D(t,x) = D_T(x) - c_2(t,x), \tag{70d}$$

where $v_{P_r}(x)$ ($\chi_r = D_r/(L^2\mu)$) and $v_{c_1}(x)$ ($\chi_c = D_{c_1}/(L^2\mu)$) are the available volume profiles (dimensionless diffusion coefficients) of $\mathrm{P_r}$ and $\mathrm{c_1}$, respectively, and from (9), $v_{c_1}(x) = v_{P_r}^2(x)$. The boundary conditions corresponding to (70) are

$$\left[v_{P_r}^2(x)\frac{d}{dx}\left[\frac{P_r(t,x)}{v_{P_r}(x)}\right]\right]_{x=0,1} = 0, \quad \left[v_{c_1}^2(x)\frac{d}{dx}\left[\frac{c_1(t,x)}{v_{c_1}(x)}\right]\right]_{x=0,1} = 0.$$

Values for dimensionless parameters: The growth rate we used to nondimensionalize the time scales was $\mu = 0.5$ 1/hr, consistent with the experiments [52]. The length of the cell is about 3μm and thus $L = 1.5\mu$m [13]. The diffusion coefficient of the transcription factor is taken to be $D_r = D_{c_1} = 0.4\mu m^2/s$ (that of LacI) [54] and thus $\chi_r = \chi_c = 1280$. The transcription factor was assumed to be stale thus $\gamma_r = \mu$. The total concentration of D given by $\bar{D}_T$ was used to nondimensionalize the other concentration variables such that $\bar{D}_T = 1$.

Additional simulation details for Figure 6 in the main text: $D_T(x) \propto e^{-20x}$ when DNA near mid cell and $D_T(x) \propto e^{20(x-1)}$ when DNA at cell poles. The transcription factor production was kept roughly spatially constant $\alpha_s(x) \propto e^{-.001x}$. The binding and unbinding coefficients were chosen to be $a_1 = a_2 = 1000$ and $d_1 = d_2 = 1000$ such that the dissociations constants $K_{d,1} = \frac{d_1}{a_1} = K_{d,2} = \frac{d_2}{a_2} = 1$.

Approxmating BCF from known parameter values:

From (9) and (2) in the main text, we observe that the effective radius of gyration of a dimer complex is $\sqrt{2}r$, where r is the radius of gyration of the individual species. In [55] it was estimated that the radius of gyration for the Tet repressor dimer is 3.1 nm and thus we estimate the radius of gyration of the monomer as $r = 3.1/\sqrt{2}$. From the expression for θ^* given by (24), Figure 4-B, and $r = 3.1/\sqrt{2}$, we have that $\theta^* \approx 0.99$ and $\theta^* \approx 1.01$, when the target DNA is near mid-cell and the cell poles, respectively. Thus, for TetR, the binding strength between the repressor and the DNA varies by about 1% with respect to a well-mixed model in this parameter range. In [56] it was estimated that the radius of gyration for the Lac repressor

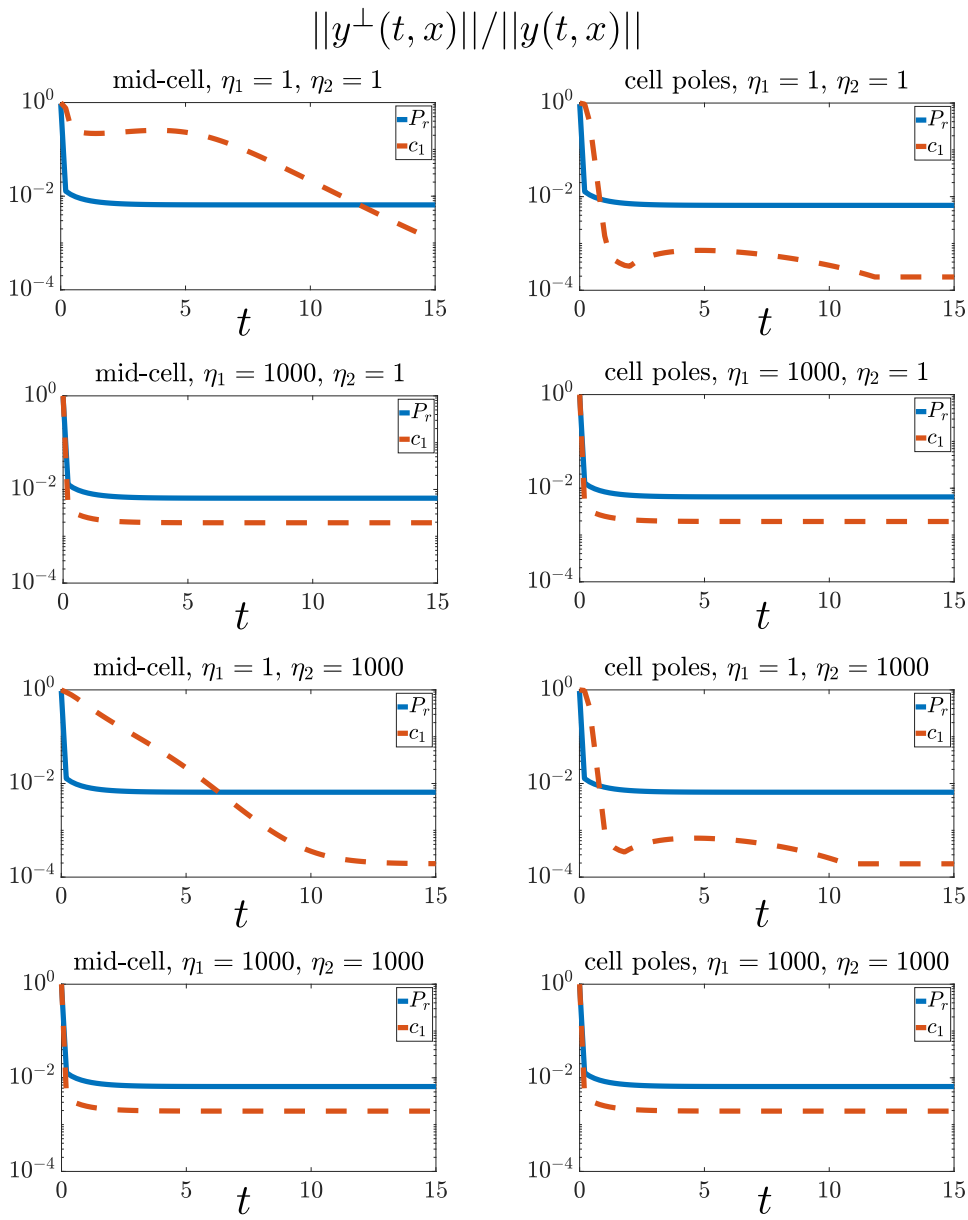

Figure 18: **Infinite dimensional dynamics decay in time independently of binding/unbinding speed** Let $y(t,x)$ be as in (70) (represents $P_r(t,x)$ or $c_1(t,x)$) and let $y^{\perp}(t,x) = y(t,x) - \bar{y}(t)v(x)$ be the a measure of the error in our approximation, where $v(x)$ is the available volume profile of the species. Let $||y(t,x)|| = (\int_0^1 (y^2(t,x)))^{1/2}$, $\eta_1 = d_1/\mu$, and $\eta_2 = d_2/\mu$ and recall that in the simulations we keep $d_1/a_1 = d_2/a_2 = 1$. We show $||y^{\perp}||/||y||$, the relative error for several values of η_1 and η_2 over dimensionless time (with respect to μ) both when the DNA is near mid-cell and the cell poles. The other simulation parameters are identical to those used to generate Figure 6 in the main text. For each time point shown, we took the max relative error with respect to the sizes of $\mathrm{P_r}$ used to generate Figure 6. The error is high at $t = 0$ since the initial spatial profiles were chosen to be a constant but note that they quickly decay.

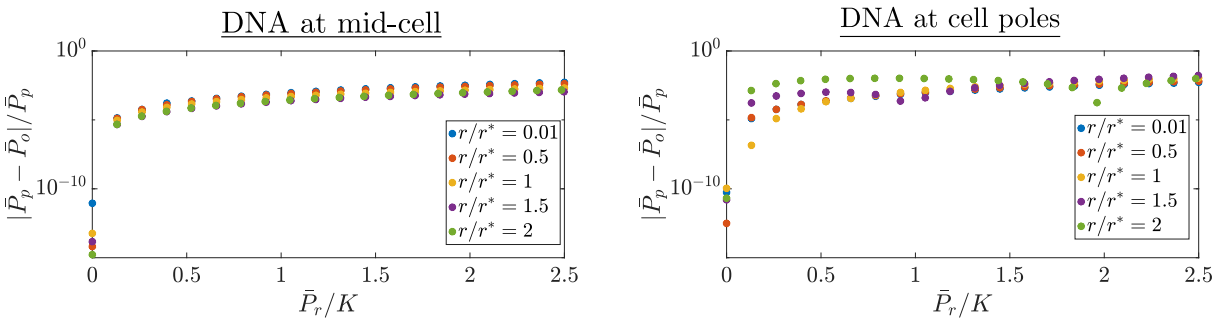

Figure 19: **The relative error between the space averaged PDE model and the reduced ODE model from the data in Figure 6 in the main text** The relative error in the steady state space averaged protein for the full PDE model ($\bar{P}_P$) and the reduced model ($\bar{P}_o$) from the data in Figure 6 in the main text. The errors are less than 1.7% both when the DNA is localized at mid-cell and at the cell poles.

tetramer is $r = 5.3$ nm. Assuming that the tetramer is made up of two dimers, then the radius of gyration of each individual dimer is given by $r = 5.3/\sqrt{2}$. From the expression for θ^* given by (24), Figure 4-B, and $r = 5.3/\sqrt{2}$, we have that $\theta^* \approx 0.97$ and $\theta^* \approx 1.03$, when the target DNA is near mid-cell and the cell poles, respectively. Thus, for the Lac repressor the binding strength between the transcription factor and the DNA varies by about 3% with respect to a well-mixed model in this parameter range.

While we could not find an exact value for the radius of gyration of the dcas9-gRNA complex, in [57] it was shown that the size of the Cas9-gRNA complex is roughly 10 nm. If we assume this value to be the radius of gyration, from Figure 4-B, we have that the BCF for this complex is $\theta^* = 0.9$ and $\theta^* = 1.1$ when the target DNA is near mid-cell and the cell poles, respectively. Thus, the binding strength between the Cas9-gRNA complex and the DNA varies s by about 10% with respect to a well-mixed model in this parameter range.

2.9 Oscillator

Now we consider the repressor activator clock genetic circuit [35]. This circuit produces sustained oscillations if tuned within an appropriate parameter range [36, 1]. The circuit consists of two proteins $\mathrm{P_a}$ and $\mathrm{P_r}$. Protein $\mathrm{P_a}$, is an activator which dimerizes to form $\mathrm{P_{a,2}}$ and then binds to its own gene $\mathrm{D_a}$ to form complex $\mathrm{c_{a,1}}$ to initiate transcription. The dimer $\mathrm{P_{a,2}}$ also finds to the gene $\mathrm{D_r}$, which transcribes $\mathrm{P_r}$ to form complex $\mathrm{c_{a,2}}$ and initiates transcription. Protein $\mathrm{P_r}$, dimerizes to form $\mathrm{P_{r,2}}$ and then represses $\mathrm{P_a}$ by binding to $\mathrm{D_a}$ to form complex $\mathrm{c_r}$. The biochemical equations corresponding to this circuit are:

$$\underbrace{\mathrm{P_a} + \mathrm{P_a} \underset{\mathrm{d_1}}{\overset{\mathrm{a_1}}{\rightleftharpoons}} \mathrm{P_{a,2}},}_{\text{Case I, } \mathrm{P}_a \text{ diffuses}} \quad \underbrace{\mathrm{P_r} + \mathrm{P_r} \underset{\mathrm{d_2}}{\overset{\mathrm{a_2}}{\rightleftharpoons}} \mathrm{P_{r,2}},}_{\text{Case II, } \mathrm{P}_r \text{ diffuses}} \quad \underbrace{\mathrm{P_{a,2}} + \mathrm{D_a} \underset{\mathrm{d_3}}{\overset{\mathrm{a_3}}{\rightleftharpoons}} \mathrm{c_{a,1}}, \quad \mathrm{P_{r,2}} + \mathrm{D_a} \underset{\mathrm{d_5}}{\overset{\mathrm{a_5}}{\rightleftharpoons}} \mathrm{c_r},}_{\text{Case III, } \mathrm{P}_{a,2} \text{ and } \mathrm{P}_{r,2} \text{ diffuse and } \mathrm{D_a} \text{ fixed}} \quad \underbrace{\mathrm{P_{a,2}} + \mathrm{D_r} \underset{\mathrm{d_4}}{\overset{\mathrm{a_4}}{\rightleftharpoons}} \mathrm{c_{a,2}},}_{\text{Case II, } \mathrm{P}_{a,2} \text{ diffuse and } \mathrm{D_r} \text{ fixed}} \tag{71a}$$

$$\mathrm{D_a} \xrightarrow{\kappa_1} \mathrm{P_a}, \quad \mathrm{D_r} \xrightarrow{\kappa_2} \mathrm{P_r}, \quad \mathrm{P_a} \xrightarrow{\gamma_a} \emptyset, \quad \mathrm{P_r} \xrightarrow{\gamma_r} \emptyset, \quad \mathrm{c_{a,1}} \xrightarrow{\kappa_3} \mathrm{P_a}, \quad \mathrm{c_{a,2}} \xrightarrow{\kappa_4} \mathrm{P_r}, \tag{71b}$$

where a_i (d_i) for $i = 1, \ldots, 5$ are association (dissociation) rate constants, γ_a (γ_r) is the degradation rate of $\mathrm{P_a}$ ($\mathrm{P_r}$) κ_1 (κ_2) is the basal rate at which gene $\mathrm{D_a}$ ($\mathrm{D_r}$) is transcribed, and κ_3 (κ_4) is the rate at which the DNA-transcription-factor complexes are transcribed for $\mathrm{D_a}$ ($\mathrm{D_r}$). We assume that the total concentration of $\mathrm{D_a}$ is conserved, so that $D_{a,T}(x) = D_a(t,x) + c_{a,1}(t,x) + c_r(t,x)$. Similarly, we assume that the total concentration of $\mathrm{D_r}$ is conserved, so that $D_{r,T}(x) = D_r(t,x) + c_{a,2}(t,x)$. The spatiotemporal dynamics describing (71) are given by

$$
\begin{aligned}
\frac{\partial P_a(t,x)}{\partial t} &= \chi_a \frac{d}{dx}\left[v_{P_a}^2(x)\frac{d}{dx}\left[\frac{P_a(t,x)}{v_{P_a}(x)}\right]\right] + \kappa_1 D_a(t,x) + \kappa_3 c_{a,1}(t,x) - \gamma_a P_a(t,x),\\
\frac{\partial P_r(t,x)}{\partial t} &= \chi_r \frac{d}{dx}\left[v_{P_r}^2(x)\frac{d}{dx}\left[\frac{P_r(t,x)}{v_{P_r}(x)}\right]\right] + \kappa_2 D_r(t,x) + \kappa_4 c_{a,2}(t,x) - \gamma_r P_r(t,x),\\
\frac{\partial P_{a,2}(t,x)}{\partial t} &= \chi_a \frac{d}{dx}\left[v_{P_{a,2}}^2(x)\frac{d}{dx}\left[\frac{P_{a,2}(t,x)}{v_{P_{a,2}}(x)}\right]\right] + a_1 P_a^2(t,x) - d_1 P_{a,2}(t,x)\\
&\quad - a_3 P_{a,2}(t,x) D_a(t,x) + d_3 c_{a,1}(t,x) - a_4 P_{a,2}(t,x) D_r(t,x) + d_4 c_{a,2}(t,x),\\
\frac{\partial P_{r,2}(t,x)}{\partial t} &= \chi_r \frac{d}{dx}\left[v_{P_{r,2}}^2(x)\frac{d}{dx}\left[\frac{P_{r,2}(t,x)}{v_{P_{r,2}}(x)}\right]\right] + a_2 P_r^2(t,x) - d_2 P_{r,2}(t,x)\\
&\quad - a_5 P_{r,2}(t,x) D_a(t,x) + d_5 c_r(t,x),\\
\frac{\partial c_{a,1}(t,x)}{\partial t} &= a_3 P_{a,2}(t,x) D_a(t,x) - d_3 c_{a,1}(t,x), \quad \frac{\partial c_{a,2}(t,x)}{\partial t} = a_4 P_{a,2}(t,x) D_r(t,x) - d_4 c_{a,2}(t,x),\\
\frac{\partial c_r(t,x)}{\partial t} &= a_5 P_{r,2}(t,x) D_a(t,x) - d_5 c_r(t,x),\\
D_a(t,x) &= D_{a,T}(x) - c_{a,1}(t,x) - c_r(t,x), \quad D_r(t,x) = D_{r,T}(x) - c_{a,2}(t,x)
\end{aligned}
\tag{72}
$$

where $v_{P_a}(x)$, $v_{P_r}(x)$, $v_{P_{a,2}}(x)$, and $v_{P_{r,2}}(x)$ are the available volume profiles of $\mathrm{P_a}$, $\mathrm{P_r}$, $\mathrm{P_{a,2}}$, and $\mathrm{P_{r,2}}$, respectively, $\chi_a = D_a/(L^2\mu)$ is the dimensionless diffusion coefficient of $\mathrm{P_a}$ and $\mathrm{P_{a,2}}$, $\chi_r = D_r/(L^2\mu)$ is the dimensionless diffusion coefficient of $\mathrm{P_r}$ and $\mathrm{P_{r,2}}$. From (9), $v_{P_{a,2}}(x) = v_{P_a}^2(x)$ and $v_{P_{r,2}}(x) = v_{P_r}^2(x)$. The boundary conditions corresponding to (72) are

$$
\left[v_{P_a}^2(x)\frac{d}{dx}\left[\frac{P_a(t,x)}{v_{P_a}(x)}\right]\right]_{x=0,1} = 0, \quad \left[v_{P_r}^2(x)\frac{d}{dx}\left[\frac{P_r(t,x)}{v_{P_r}(x)}\right]\right]_{x=0,1} = 0,
$$

$$
\left[v_{P_{a,2}}^2(x)\frac{d}{dx}\left[\frac{P_{a,2}(t,x)}{v_{P_{a,2}}(x)}\right]\right]_{x=0,1} = 0, \quad \left[v_{P_{r,2}}^2(x)\frac{d}{dx}\left[\frac{P_{a,2}(t,x)}{v_{P_{r,2}}(x)}\right]\right]_{x=0,1} = 0.
$$

Parameters for Figure 7 in the main text: The growth rate we used to nondimensionalize the time scales was $\mu = 0.5$ 1/hr, consistent with the experiments [52]. The length of the cell is about 3μm and thus $L = 1.5\mu$m [13]. The diffusion coefficient of the transcription factor is taken to be $D_a = D_r = 0.4\mu m^2/s$ (that of LacI) [54] and thus $\chi_a = \chi_r = 1280$. The following dimensionless parameters were chosen such that the well-mixed model displayed sustained oscillations: $a_1 = 220, d_1 = 1000, a_2 = 1000, d_2 = 1000, a_3 = 1000, d_3 = 1000, a_4 = 1000, d_4 = 1000, a_5 = 1000, d_5 = 1000, \kappa_3 = 250, \kappa_1 = .04, \kappa_4 = 30, \kappa_2 = .004, \gamma_a = 1, \gamma_r = 0.5$. Furthermore, we choose d_i and a_i for $i = 1, \ldots 5$ large, to demonstrate our results hold even for large binding and unbinding rates. The total concentration of $\mathrm{D_a}$ which is the same as $\mathrm{D_r}$ since we assume they are on the same plasmid, is given by $\bar{D}_T$ and it was used to nondimensionalize the other concentration variables such that $\bar{D}_T = 1$. The total DNA spatial profile was chosen as $D_T(x) \propto e^{50(x-1)}$ to model DNA at cell poles.

2.10 Numerical Method Convergence Rate

For the simulation in Figure 5-A when the DNA is localize at the cell-poles and $r_s/r^* = 1$, we varied the number of spatial nodes used to discretized the spatial domain to demonstrate the convergence rate of our numerical scheme. Let N be the number of points used to discretize the spatial domain and let $\bar{m}_N(t)$ as the space averaged mRNA concentration for that given discretization. We considered when $N = 1024$ to be the true solution $m_{1024}(t)$ and thus define the following relative error

$$
e_\infty = \max_{t\in[0,T]} \left| \frac{\bar{m}_N(t) - \bar{m}_{1024}(t)}{\bar{m}_{1024}(t)} \right|, \tag{73}
$$

where we took its max value over the time interval of the simulation $t \in [0, T]$ where $T = 100$. The results from this numerical experiment are shown in Figure 22. The convergence rate of our numerical scheme is $\mathcal{O}(N^{-2})$ as expected for a second order finite difference numerical scheme.

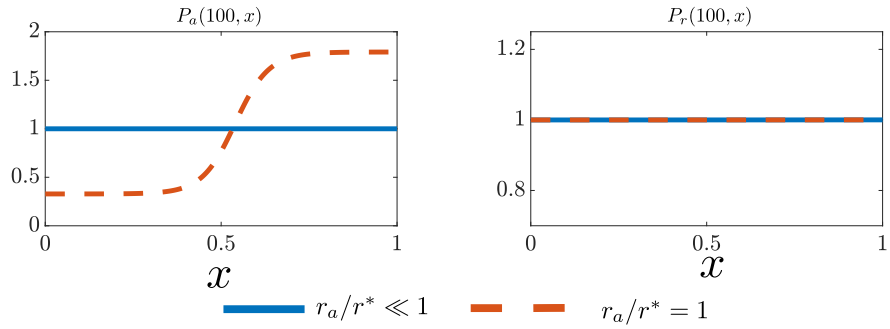

Figure 20: **The activator is excluded from the chromosome as its size increases** The steady state spatial profiles normalized by the average values for $\mathrm{P_a}$ and $\mathrm{P_r}$, that is $P_a(\infty,x)/\bar{P}_a(\infty)$ and $P_r(\infty,x)/\bar{P}_a(\infty)$ for the results of Figure 7 in the main text. As the size of $\mathrm{P_a}$ increases it is excluded from the chromosome. The repressor remains homogeneously distributed throughout the cell. The parameter values and simulation details are identical to those of Figure 7 in the main text.

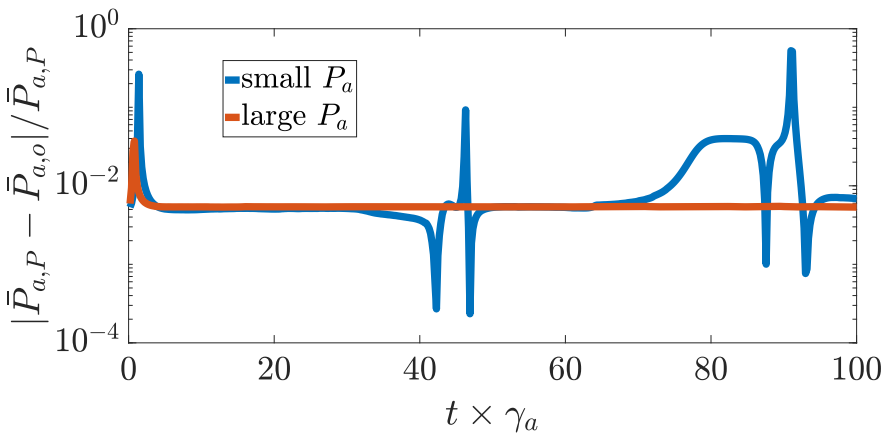

Figure 21: **The relative error between the space averaged PDE model and the reduced ODE model from the data in Figure 7 in the main text** The relative error in the steady state space averaged activator protein concentration for the full PDE model ($\bar{P}_{a,P}$) and the reduced model ($\bar{P}_{a,o}$) from the data in Figure 7 in the main text. Note that for the case when $\mathrm{P_a}$ is small, large relative errors occur near when $\bar{P}_a(t)$ reaches a minimum during each period of oscillation. Otherwise all errors are less than 1%.

2.11 Estimating r^* from Concentration Profiles and Estimating the BFC

Estimate r^*: As discussed in Remark 1 in the main text, we expect the concentration profile of a freely diffusing species to mirror that of the normalized available volume profile. That is, for a freely diffusing species y, with concentration $y(t,x)$, and available volume profile $v(x)$, we expect

$$y(t,x) \approx \bar{y}(t)\hat{v}(x) \quad \text{where} \quad \bar{y}(t) = \int_0^1 y(t,x)dx, \quad \text{and} \quad \hat{v}(x) = \frac{v(x)}{\int_0^1 v(x)dx}. \tag{74}$$

Suppose the radius of gyration of y denoted by r, is known and as discussed in the main text, we have that $v(x) = e^{-(r/r^*)^2\hat{\rho}(x)}$. Approximating $\hat{\rho}(x)$ as a step function as in (59), we have that $v(1) \approx 1$ and $v(0) = e^{-\frac{(r/r^*)^2}{2(1-\Delta x)}}$, where Δx is the distance between the end of the chromosome and the cell poles (see Figure 1 in the main text). Let let y^{in} and y^{out} denote the the average concentration inside and outside the nucleotide, respectively, which are given by

$$y^{\text{in}} = \frac{1}{1-\Delta x}\int_0^{1-\Delta x} y(x)dx, \quad y^{\text{out}} = \frac{1}{\Delta x}\int_{1-\Delta x}^1 y(x)dx.$$

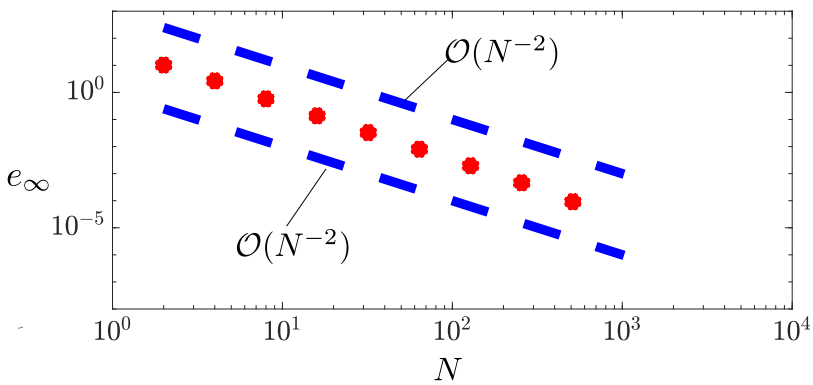

Figure 22: **Convergence rate of numerical scheme used to simulate PDEs in this work** For the simulation in Figure 5-A when the DNA is localize at the cell-poles and $r_s/r^* = 1$, we varied the number of spatial nodes used to discretize the spatial domain to demonstrate the convergence rate of our numerical scheme. Let N be the number of points used to discretize the spatial domain and let $\bar{m}_N(t)$ as the space average mRNA concentration for that given discretization. We considered when $N = 1024$ to be the true solution $m_{1024}(t)$ and the relative error e_∞ is given by (73). The relative error is given by the red markers and the blue dashed lines serve as references for $\mathcal{O}(N^{-2})$ convergence rates.

Let $\psi_y = y^{\text{out}}/y^{\text{in}}$ and from (74), we have that

$$\psi_y = y^{\text{out}}/y^{\text{in}} = v(0)/v(1) = v(0) = e^{-\frac{(r/r^*)^2}{2(1-\Delta x)}}, \tag{75}$$

then r^* can be estimated assuming one knows Δx, that is, how far the dense nucleoid region extends beyond mid-cell. A similar calculation was done in [13], using the fact that the free ribosome concentration is 10% higher at the cell poles than mid-cell. To estimate ψ, it is sufficient to know the average concentration of a species inside and outside nucleoid region.

Estimate the BCF: The BCF provides a measure to determine the extent to which spatial effects modulate the biomolecular dynamics. Therefore, an experimental method to estimate the BCF is desirable. We propose a method that only requires knowing Δx and the concentration of freely diffusing species inside and outside the nucleoid .

Suppose that for Case I and Case III, the concentration of $\mathrm{E_i}$ is measured inside and outside the nucleoid and denoted by E_i^{in} and E_i^{out}, respectively. Similarly, for Case I and Case II, we assume that S^{in} and S^{out} is measured. If a fluorescence imaging method is used to measure these quantities (as in [14]), then we emphasize that the free $\mathrm{E_i}$ and S must be measured, not when they are in complex form ($\mathrm{c_i}$). Let $\psi_i = E_i^{\text{out}}/E_i^{\text{in}}$ and $\psi_s = S^{\text{out}}/S^{\text{in}}$. By (75), $\psi_i = v_{0,E_i}$ and $\psi_s = v_{0,S}$, where v_{0,E_i} and $v_{0,S}$ are as in (60). Thus, using (61) we can estimate the BCF for Cases I-III by

- Case I:

$$\theta_i^* = \frac{\psi_i\psi_s(1-\Delta x) + \Delta x}{\left[\psi_i(1-\Delta x) + \Delta x\right]\left[\psi_s(1-\Delta x) + \Delta x\right]},$$

- Case II and Case III:

$$a_i = \begin{cases} \psi_s, & \text{Case II} \\ \psi_i, & \text{Case III} \end{cases},$$

$$\theta_i^* = \begin{cases} 0 \le \dfrac{a_i}{a_i(1-\Delta x) + \Delta x} \le 1, & x_i^* \le 1-\Delta x \text{ for Case II and } x_s^* \le 1-\Delta x \text{ for Case III} \\ 1 \le \dfrac{1}{a_i(1-\Delta x) + \Delta x} \le \dfrac{1}{\Delta x} & x_i^* > 1-\Delta x \text{ for Case II and } x_s^* > 1-\Delta x \text{ for Case III.} \end{cases}$$

As $r_{e,i}/r^* \to \infty$ ($r_s/r^* \to \infty$) we have that $\psi_i \to 0$ ($\psi_s \to 0$), thus ψ_i and ψ_s are a measure of the excluded volume effects on $\mathrm{E_i}$ and S, respectively. Physically, this is expected because when $\mathrm{E_i}$ is severely expelled from the nucleoid by available volume effects, we have that $E_i^{\text{out}} \ll E_i^{\text{in}}$ and similarly for S.

2.12 Experimental Setups to Verify the Role of Spatial Effects Predicted by Model

A potential experiment to test our hypothesis that genes near the poles our transcribed more effectively than gene near mid-cell, is to measure the rate of transcription (via Quantitative PCR) of a gene under the control of the T7 promoter. This promoter is solely transcribed by the T7 RNAP which specifically targets the promoter, thus this system can be considered orthogonal to the endogenous transcription machinery [58]. By appending random base pairs (BPs) to the sequence of T7 RNAP that do not effect its functionally, we can control its size and thus how much excluded volume effects it experiences. We can then measure the transcription rate of the gene when it is localized in the cell-poles and mid-cell. The results of this experiment should look similar to Figure 5-A in the main text, as the size of the T7 RNAP increases the mid-cell (pole) gene has lower (higher) transcription rate. For the mid-cell localized gene, this can be repeated in parts of the chromosome which are known to be dense to amplify these effects.

To experientially validate our analytical prediction that protein steady state levels will increase with mRNA size, we propose expressing a florescence protein from a plasmid with an appended sequence of base pairs added downstream of the stop codon. The appended sequence should have a low affinity to recruit ribosome such that the amount of ribosomes sequestered by the mRNA are the same as without the appended sequence. Assuming this appended sequence does not affect the lifetime of the mRNA, then it should yield the same functional protein which can be used to quantify the mRNA excluded volume effects. This appended sequence of base pairs will allow us to control the size of the mRNA without increasing its ribosome usage. From our theory, for longer appended sequences, more protein expression is expected.

To validate the hypothesis that a transcriptional repressor regulates genes near the poles more effectively than gene near mid-cell, we propose a genetic circuit on a plasmid expressing a repressor that targets a gene expressing a florescence protein. The transcription factor chosen should be large enough or dimerize to have considerate excluded volume effects. The target DNA expressing protein should be placed on several axial locations in the cell (under the same promoter) achieved by using backbones with different localization profiles and/or different chromosomal integration sites. We should observe that the effective disassociation constant of the repression curve increases as the target genes location is closer to the mid-cell. The disassociation constant is proportional to the amount of repressor necessary to cause the genes expression to decrease by half.

2.13 Cell Division: Time Varying Cell Length and Chromosome Profile

As the cell divides it partitions molecular species amongst daughter cells, this along with changes in the cell length cause dilution effects on intracellular concentrations. Furthermore, early in the cell division cycle, the chromosome density is highest mid-cell, but as the cell divides the peak chromosome density tends towards the cell-poles [14, 13] (to distribute genes evenly among daughter cells). From the results in the main text, we expect this temporal changes in the chromosome density will effect the BCF since species are repelled away from regions with high chromosome density via excluded volume effects. In this section, we provide the modeling framework to account for dilution effects and temporal fluctuations in the chromosome density.

Dilution effects on spaced average concentrations: Here we demonstrate how cell division and a time varying cell length effects space average concentrations. Let $\bar{N}_p(t)$ be the total molecular count in a cell population of a molecule of interest (i.e., ribosomes) as the cell expands and divides. To model dilution from cell division, assume that $\bar{N}_p(t)$ is identically distribute among $N_{\text{cells}}(t)$ number of cells such that $N_{\text{cells}}(t) = N_{\text{cells}}(0)e^{\mu t}$, where μ is the cell growth rate and each cell has a volume given by $V_c(t) = 2\pi R^2 L(t)$, where R is the cell radius and $2L(t)$ is the cell length. The total population volume is then given by $V(t) = N_c(t)V_c(t)$ and letting $\bar{c}(t)$ be the number of molecules per total volume (concentration), this quantity is given by $\bar{c}(t) = \frac{\bar{N}_p(t)}{V(t)}$, note that this is identical to the concentration per cell volume (since we assume all cells in the population have identical averaged concentrations). This implies that

$$\dot{\bar{c}}(t) = \frac{\dot{\bar{N}}_p(t)}{V(t)} - \underbrace{\frac{\dot{V}(t)}{V(t)}\bar{c}(t)}_{\text{dilution effects}} = \frac{\dot{\bar{N}}_p(t)}{V(t)} - (\underbrace{\mu}_{\text{cell division}} + \underbrace{\frac{\dot{L}}{L}}_{\text{varying length}})\bar{c}(t).$$

Dilution effects on local concentrations: Let $N(t,x)$ be the number of molecules per unit length of a cell such that that $\int_0^{L(t)} N(t,x)dx = \frac{\bar{N}_p(t)}{N_{\text{cells}}(t)}$. The temporal evolution of $N(t,x)$ in the presence of dilution

and a moving boundary, which introduces an advective term [59] (to account for the extra diffusion as the cell length varies), is given by

$$\frac{\partial N(t,x)}{\partial t} = \underbrace{D\frac{d}{dx}\big[v^2(x)\frac{d}{dx}[\frac{N(t,x)}{v(x)}]\big]}_{\text{diffusion}} \underbrace{-\frac{d}{dx}(u(t,x)N(t,x))}_{\text{advection}} + \underbrace{f(t,x,N)}_{\text{reaction}} - \underbrace{\mu N(t,x)}_{\text{dilution}}, \tag{77}$$

with boundary conditions

$$D\left[v^2(x)\frac{d}{dx}[\frac{N(t,x)}{v(x)}]\right]_{x=0,x=L(t)} = 0,$$

where $u(t,x) = \frac{x}{L(t)}\dot{L}(t)$ is the velocity of a material point induced by the increase in cell length. Notice that our current finite difference method with a stationary mesh cannot be applied directly to (77), thus we propose the following spatial coordinate transformation $y(t,x) = \frac{x}{L(t)}$ (and to be consistent with the nondimensionalization from the main text), which renders a stationary domain. Let $c(t,y) := N(t, yL(t))$ and thus $\frac{dN}{dt} = \frac{dc}{dt} = \frac{\partial c}{\partial t} + \frac{\partial c}{\partial y}\frac{\partial y}{\partial t} = \frac{\partial c}{\partial t} - \frac{\partial c}{\partial y}y\frac{\dot{L}}{L}$, finally

$$\begin{aligned}\frac{\partial c}{\partial t} =& \frac{\partial c}{\partial y}y\frac{\dot{L}}{L} + \frac{D}{L^2(t)}\frac{d}{dy}\big[v^2(y)\frac{d}{dy}[\frac{c}{v(y)}]\big] - \frac{1}{L(t)}\frac{d}{dy}(uc) + f(t,c) - \mu c,\\ =& \frac{D}{L^2(t)}\frac{d}{dy}\big[v^2(y)\frac{d}{dy}[\frac{c}{v(y)}]\big] + f(t,c) - (\mu + \frac{\dot{L}}{L})c.\end{aligned}$$

Notice that the effective dilution coefficient is now given by $\frac{D}{L^2(t)}$, which as expected increases as cell length increases and $2\int_0^1 c(t,y)dy = 2\int_0^{L(t)} \frac{N(t,x)}{L(t)}dx = \dot{\bar{c}}(t)$, thus the space averaged under this coordinate system provides us the concentration per cell volume. The boundary conditions are

$$D\left[v^2(y)\frac{d}{dy}[\frac{c(t,y)}{v(y)}]\right]_{y=0,y=1} = 0.$$

Time varying chromosome density: We now model the chromosome density varying in time $\hat{\rho} := \hat{\rho}(t,x)$ as the cell divides. This implies that the available volume profiles will also depend on time since $v(x,t) = e^{-\frac{r}{r^*}\hat{\rho}(x,t)}$, and thus

$$\frac{\partial c}{\partial t} = \frac{D}{L^2(t)}\frac{d}{dy}\big[v^2(t,y)\frac{d}{dy}[\frac{c}{v(t,y)}]\big] + f(t,c) - \tilde{\mu}(t)c,$$

where $\tilde{\mu}(t)$ is the effective dilution rate given by

$$\tilde{\mu}(t) = \mu + \frac{\dot{L}(t)}{L(t)} \tag{78}$$

The quantities $L(t)$ and $v(t,x)$ will vary with a time scale related to cell growth, for example, let $T_{1/2} = \frac{\ln(2)}{\mu}$ be the cell doubling time, then one possibility is

$$L(t) = L_0(1 - \Delta_L \cos(2\pi t/T_{1/2})), \tag{79}$$

for this choice of $L(t)$, the effective dilution rate (78) is graphically shown in Figure 23. In [13] it was shown the cell length late in the cell division cycle was $4.4\mu m$ (compare to its nominal length $3\mu m$), thus for our simulations we take $\Delta_L = 0.2$.

In [14] it was experimentally shown how the chromosome density varies with time and a model for the density in early ($\hat{\rho}_1(y)$) and late ($\hat{\rho}_2(y)$) in the cell division process were provided in [13]

$$\hat{\rho}_1(y) = c_1\frac{1}{1+e^{20(y-1/2)}} \quad \hat{\rho}_2(y) = c_2\frac{e^{-6(1/2-y)^2} + e^{-6(1/2+y)^2}}{1+e^{20(y-2/3)}}$$

where c_1 and c_2 are chosen such that $\int_0^1 \hat{\rho}_1 dy = \int_0^1 \hat{\rho}_2 dy = 1/2$. To capture the transition between $\hat{\rho}_1$ and $\hat{\rho}_2$ as the cell divides we propose the following model

$$\hat{\rho}(t,y) = 1/2\Big(\hat{\rho}_1(y)\cos^2(\pi t/T_{1/2}) + \hat{\rho}_2(y)\sin^2(\pi t/T_{1/2})\Big), \tag{80}$$

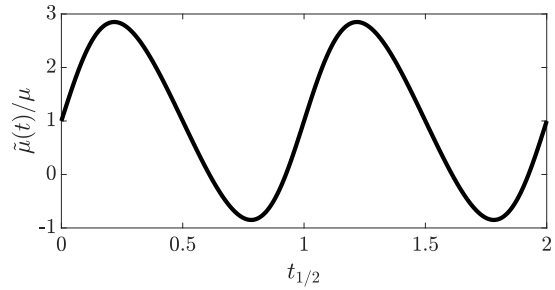

Figure 23: **Varying cell length modulates dilution rate** The effective dilution rate (78) is given for $L(t)$ given by (79) and $\Delta_L = 0.2$, where $t_{1/2}$ is time normalized by the cell doubling time ($t_{1/2} = t/T_{1/2}$).

notice that $\int_0^1 \rho(t,y)dy = 1/2, \forall t \geq 0$. The model for the cell length and the chromosome density is shown in Figure 24. The model for the chromosome density is consistent with experimental observations where late in the division phase the chromosome is in the form of two lobes, where each lobe of DNA will correspond to a daughter cell.

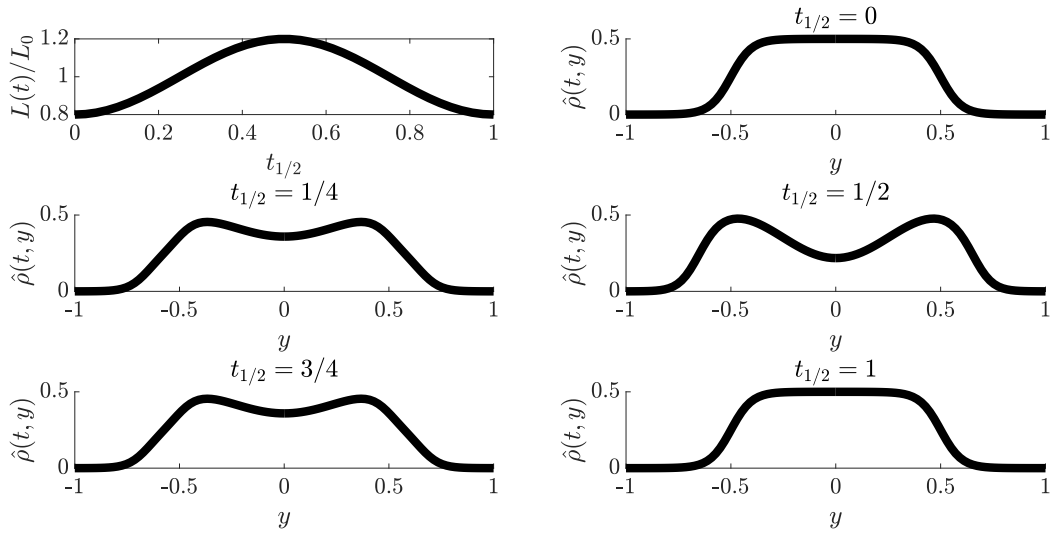

Figure 24: **The cell length and chromosome density varies over time** The normalized cell length $L(t)/L_0$ (79) with $\Delta_L = 0.2$ and the chromosome density $\hat{\rho}(t,y)$ (80) shown over one cell division cycle, where $t_{1/2}$ is time normalized by the cell doubling time. The model for the chromosome density is consistent with experimental observations [14, 13] where late in the division phase the chromosome is in the form of two lobes, where each lobe of DNA will correspond to a daughter cell.

Time scale separation: When the scale associated with diffusion is much fast than dilution $D/L_0 \gg \mu$ (and any other time scale associated with the reaction dynamics), we can treat $L(t)$ and $v(t,y)$ as constant in time when performing model reduction as in Section 1.3 in the main text, thus we expect (similar to the results of the main text)

$$c(t,y) \approx \bar{c}(t)\hat{v}(t,y), \tag{81}$$

where $\bar{c}(t) = \int_0^1 c(t,y)dy$ and $\hat{v}(t,y) = v(t,y)/\int_0^1 v(t,y)dy$. So all of our previous analysis still holds except that the BCF will vary slowly (slow with respect to the time scale of diffusion) as the cell divides.

Example: We verify via simulations the prediction that (81) holds and that the BCF can be treated as a slowly (with respect to diffusion) varying parameter. Consider the simple bimolecular reaction:

$$\mathrm{E} + \mathrm{S} \underset{\mathrm{d}}{\overset{\mathrm{a}}{\rightleftharpoons}} \mathrm{c}, \quad \emptyset \xrightarrow{\alpha_{\mathrm{e}}} \mathrm{E}, \qquad \emptyset \xrightarrow{\alpha_{\mathrm{s}}} \mathrm{S}, \tag{82}$$

with dynamics given by

$$\begin{aligned}
\frac{\partial E(t,y)}{\partial t} &= \frac{D_e}{L^2(t)}\frac{d}{dy}\big[v_e^2(t,y)\frac{d}{dy}[\frac{E(t,y)}{v_e(t,y)}]\big] + \alpha_e(y) - aE(t,y)S(t,y) + dc(t,y) - \tilde{\mu}(t)E(t,y),\\
\frac{\partial S(t,y)}{\partial t} &= \frac{D_s}{L^2(t)}\frac{d}{dy}\big[v_s^2(t,y)\frac{d}{dy}[\frac{S(t,y)}{v_s(t,y)}]\big] + \alpha_s(y) - aE(t,y)S(t,y) + dc(t,y) - \tilde{\mu}(t)S(t,y),\\
\frac{\partial c(t,y)}{\partial t} &= \frac{D_c}{L^2(t)}\frac{d}{dy}\big[v_c^2(t,y)\frac{d}{dy}[\frac{c(t,y)}{v_c(t,y)}]\big] + aE(t,y)S(t,y) - \tilde{\mu}(t)c(t,y),
\end{aligned} \tag{83}$$

where $\alpha_e(y)$ and $\alpha_s(y)$ are the production rates of E and S, respectively. The space averaged dynamics ($\bar{E}(t) = \int_0^1 E(t,y)dy$, $\bar{S}(t) = \int_0^1 S(t,y)dy$, and $\bar{c}(t) = \int_0^1 c(t,y)dy$) are given by

$$\begin{aligned}
\frac{d\bar{E}(t)}{dt} &= \bar{\alpha}_e - a\theta(t)\bar{E}(t)\bar{S}(t) + d\bar{c}(t) - \tilde{\mu}(t)\bar{E}(t),\\
\frac{d\bar{S}(t)}{dt} &= \bar{\alpha}_s - a\theta(t)\bar{E}(t)\bar{S}(t) + d\bar{c}(t) - \tilde{\mu}(t)\bar{S}(t),\\
\frac{d\bar{c}(t)}{dt} &= a\theta(t)\bar{E}(t)\bar{S}(t) - \tilde{\mu}(t)\bar{c}(t),
\end{aligned} \tag{84}$$

where the BCF is given by

$$\theta(t) = \frac{\int_0^1 E(t,y)S(t,y)dy}{\big[\int_0^1 E(t,y)dz\big]\big[\int_0^1 S(t,y)dy\big]}. \tag{85}$$

We first focus on the $E(t,y)$ dynamics when $a = 0$ and $d = 0$

$$\frac{\partial E(t,y)}{\partial t} = \frac{D_e}{L^2(t)}\frac{d}{dy}\big[v_e^2(t,y)\frac{d}{dy}[\frac{E(t,y)}{v_e(t,y)}]\big] + \alpha_e(y) - \tilde{\mu}(t)E(t,y) \tag{86}$$

to show the effects of having time varying dilution $\tilde{\mu}(t)$ and available volume profiles on the expression level. Figure 25 shows how the space averaged concentration $\bar{E}(t)$ is modulated by the time varying dilution $\tilde{\mu}(t)$. We observe that the concentration reaches a periodic steady state centered at unity where the oscillations have a period that coincides with the doubling time. Furthermore, in Figure 26, we verify that

$$E(t,x) \approx \bar{E}(t)\hat{v}_e(t,y)$$

where $\hat{v}_e(t,y) = v_e(t,y)/\int_0^1 v_e(t,y)dy$ as expected (since diffusion much faster than dilution $D_e/(L_0\mu) \gg 1$). Thus, even with a time varying $v_e(t,y)$, the enzyme will be expelled from the chromosome to areas of higher available volume.

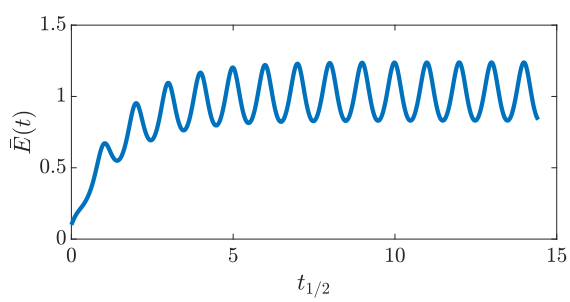

Figure 25: **Enzyme expression as cell length varies** The space averaged enzyme expression (86) there is no binding/unbinding with S ($a = 0$ and $d = 0$). The oscillations arise due to changes in the cell length during cell division. The simulation parameters are: $r_e/r^* = 2$ $\mu = 1$ $D_e/(L_0\mu) = 13 \times 10^3$ $\alpha_e(y) = 1$, $\Delta_l = 0.2$.

Next, we demonstrate how the binding dynamics are effected by having a time varying available volume profile, therefore $a \neq 0$ in (83). Similar to "Case 1" in the main text, we consider the case when $D_e, D_s, D_c \neq 0$ (all species freely diffuse), where we expect the BCF to be approximated by

$$\theta^*(t) = \frac{\int_0^1 v_e(t,y)v_s(t,y)dy}{\big[\int_0^1 v_e(t,y)dy\big]\big[\int_0^1 v_s(t,y)dy\big]}. \tag{87}$$

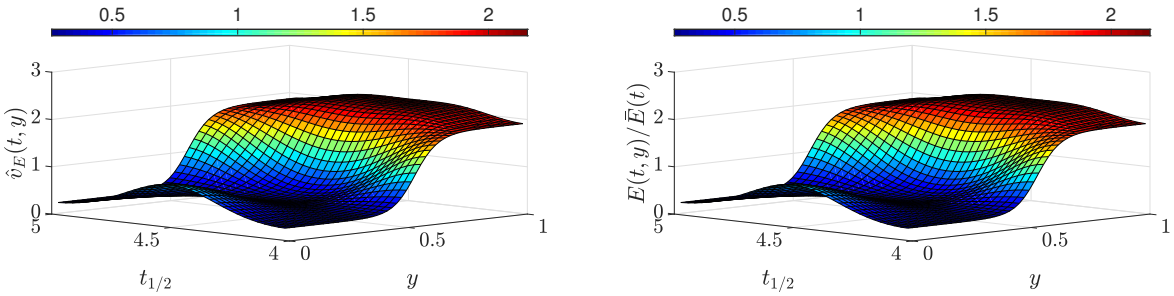

(a) Normalized available volume profile

(b) Normalized enzyme concentration

Figure 26: **The normalized enzyme spatial profile matches that of its normalized available volume profile.** The enzyme concentration spatial profile normalized by its space average shown over one cell division cycle after four cell division cycles ("steady state") matches its available volume as expected (86). The simulation parameters are: $r_e/r^* = 2$ $\mu = 1$ $D_e/(L_0\mu) = 13 \times 10^3$ $\alpha_e(y) = 1$, $\Delta_l = 0.2$.

This is verified in Figure 27, where $\theta(t)$ given by (85) and $\theta^*(t)$ given by (87) are shown after three doubling times and are shown to be in good agreement. The BCF varies periodically in time (with the period consistent with the doubling time) and oscillates near a nominal value of 1.5 with amplitude 0.04.

Next we look at the the case when S and c are spatially fixed ($D_s = D_c = 0$) and localized near y^*, which is similar to "Case 2" in the main text. For this scenario we expect the BCF to be approximated by

$$\theta^*(t) = \hat{v}_s(t, y^*). \tag{88}$$

The results are shown in Figure 28 when $y^* = 0$ and $y^* = 1$ after three doubling times, there is good agreement between the BCF and its approximation. When $y^* = 0$ (S localized near mid-cell), the BCF is less than unity and oscillates near a nominal value of 0.55 with amplitude 0.3. When $y^* = 1$ (S localized near the cell poles), the BCF is greater than unity and oscillates near a nominal value of 2 with amplitude 0.1.

These results suggest that the BCF for a species localized near mid-cell will vary significantly as the cell density varies during cell division. This is expected because as shown in Figure **??**, the chromosome density is initially high near mid-cell but decreases by half as the cell divides, thus no longer excluding from that region.

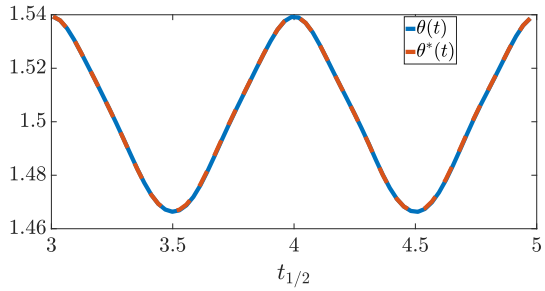

Figure 27: **The BCF for the case when all species freely diffuse** The binding correction factor $\theta(t)$ (85) and its approximation θ^* (87) over two cell division cycles. The BCF oscillates around a nominal value of 1.5 with amplitude 0.04 and period consistent with the doubling time. The simulation parameters are $r_e/r^* = r_s/r^* = 2$, $r_c/r^* = 2\sqrt{2}$, $\mu = 1$, $D_e/L_0 = D_s/L_0 = D_c/L_0 = 13 \times 10^3$ $\alpha_e(y) = \alpha_s(y) = 1$, $\Delta_l = 0.2$, $d = 100$, $a = 100$.

2.14 Exclusion Effects from Plasmid DNA Density

The genome of *E. coli* MG1655 has 4.6 Mbp [60]. Comparatively, a single plasmid can have .01 Mbp a copy number as high as 500-700 (e.g. pUC19). Therefore, the total plasmid and chromosome basepair count may be comparable in applications with high copy number plasmids. In these applications, it may be necessary to

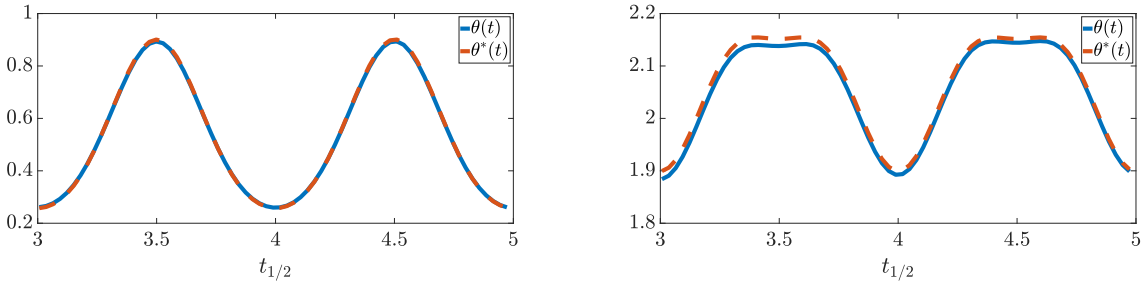

(a) $y^* = 0$ (b) $y^* = 1$

Figure 28: **The BCF for the case when** S **is spatially fixed at** y^* The binding correction factor $\theta(t)$ (85) and its approximation θ^* (88) over two cell division cycles. The BCF oscillates with a period consistent with the doubling time. When $y^* = 0$ (S localized near mid-cell), the BCF is less than unity and oscillates near a nominal value of 0.55 with amplitude 0.3. When $y^* = 1$ (S localized near the cell poles), the BCF is greater than unity and oscillates near a nominal value of 2 with amplitude 0.1. This is shown for a molecule localized near mid-cell $y^* = 0$ and near the cell poles $y^* = 1$. The simulation parameters are $r_e/r^* = r_s/r^* = 2$, $r_c/r^* = 2\sqrt{2}$, $\mu = 1$, $D_e/L_0 = D_s/L_0 = D_c/L_0 = 13 \times 10^3$ $\alpha_e(y) = \alpha_s(y) = 1$, $\Delta_l = 0.2$, $d = 100$, $a = 100$.

account how plasmid DNA repels freely diffusing species and "excludes" them. To do so we modify our model of the DNA density $\hat{\rho}(x)$ as shown in Figure 29 to account for plasmid DNA. For the DNA density profiles from Figure 29, we calculate the approximate BCF θ^* (13), these are shown in Figure 30. For Case 1 where the reactants freely diffuse. We observe that the BCF decreases as the plasmid DNA density increases (as shown in Figure 29). This occurs because as the plasmid DNA increases the overall density profile becomes more uniform. Note that when the plasmid DNA is sufficiently high to render an almost uniform DNA density profile, the BCF is unity as expected. For Case 2, where one reactant freely diffuses and the other is fixed at x^*. As the plasmid density increases (as shown in Figure 29) we observe that the BCF decreases at the cell poles (as expected since species are excluded from dense plasmid DNA mesh) and increases at region near $x^* \approx 0.65$ (where there is minimal overlap between chromosome and plasmid DNA). When the plasmid DNA density is similar to that of the chromosome rending a uniform DNA distribution, we observe that the BCF is unity everywhere (as expected since there are no exclusion effects).

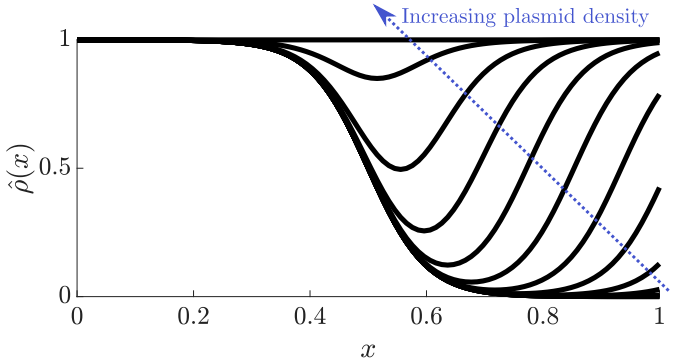

Figure 29: **DNA density with plasmid contributions**. The DNA density now includes contributions from plasmid DNA. We show several profiles with increasing plasmid density. For this results we had $\hat{\rho}(x) = \frac{1}{1+e^{20(x-1/2)}} + \frac{1}{1+e^{20(-x+x_s)}}$ where $x_s \in [1/2, 3/2]$ is the parameter we varied to get difference plasmid densities ($x_s = 3/2$ lowest plasmid density and $x_s = 1/2$ highest plasmid density).

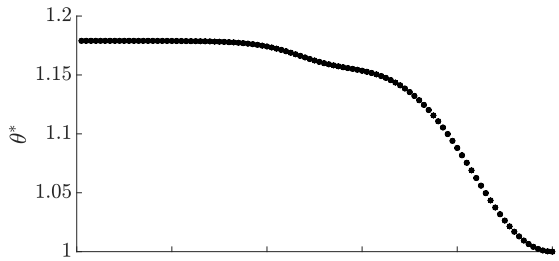

(a) Case 1: Reactants freely diffuse

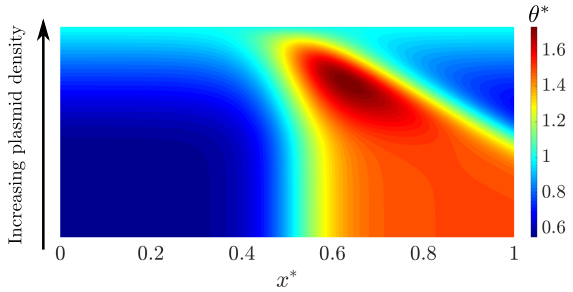

(b) Case 2: One reactant diffuses and the other fixed at x^*

Figure 30: **The approximate BCF θ^* when plasmid DNA is accounted for** (a) Case 1 where the reactants freely diffuse. We observe that the BCF decreases as the plasmid DNA density increases (as shown in Figure 29). This occurs because as the plasmid DNA increases the overall density profile becomes more uniform. Note that when the plasmid DNA is sufficiently high to render an almost uniform DNA density profile, the BCF is unity as expected. (b) Case 2 where one reactant freely diffuses and the other is fixed at x^*. As the plasmid density increases (as shown in Figure 29) we observe that the BCF decreases at the cell poles (as expected since species are excluded from dense plasmid DNA mesh) and increases at region near $x^* \approx 0.65$ (where there is minimal overlap between chromosome and plasmid DNA). When the plasmid DNA density is similar to that of the chromosome rending a uniform DNA distribution, we observe that the BCF is unity everywhere (as expected since there are no exclusion effects). The simulation parameters are $r/r^* = 1$ and $\hat{\rho}(x)$ as in Figure 29.